School of Aerospace, Mechanical and Mechatronic Engineering

Analysis on the relationship between wind veer and the wind turbine wake in the context of wake steering

By

ELLA KERR

Supervisor:

Associate Professor Michael Kirkpatrick

This thesis was submitted to the Faculty of Engineering of the University of Sydney in fulfilment of the requirements for the degree of Master of Philosophy (Engineering)

2023

Abstract

Wake steering is the intentional yaw misalignment of upstream wind turbines in a wind farm to deflect the low energy wakes away from the turbines downstream. This improves the inflow conditions for downstream turbines and has been shown to improve overall power production in computational, experimental and field tests of the technique. Wake steering is most applicable in the stable atmospheric boundary layer (SBL), which is characterised by a low level of turbulence and so wakes persist for longer distances through wind farms, resulting in higher wake losses than in neutral or convective atmospheric conditions. A common feature of the SBL is wind veer, which is the change in wind direction with height due to a balance between the pressure gradient, atmospheric friction and the Coriolis forcing. Wind veer has been previously shown to affect the skew of the wake and its downstream trajectory at different heights across the rotor. To further investigate the influence of wind veer on wake behaviour, in the context of how it would affect the application or effectiveness of wake steering, numerical simulations of wakes in varying veered flow conditions were performed. The Simulator fOr Wind Farm Applications (SOWFA), a Large Eddy Simulation (LES) solver, was used to model the turbine and SBL flow. The turbine yaw angle and Coriolis forcing, via the latitude location of the turbine, were also varied to represent wake steering and generate different inflow wind veer profiles.

The wake cross-section was observed to skew according to the inflow wind veer profile, with the veer exhibited by the wake shown to match the inflow veer close to the turbine rotor before fading with downstream distance. The inflow wind veer profile and skew of the wake shape was found to have a directional impact on the deflection of wakes generated in veered flow, with the direction of skew observed in the wake region below hub height appearing to dominate where the wake centre was located. The recovery of the skewed wake was also determined to occur faster than wakes produced in non-veered flow. A two turbine simulation performed in non-veered and veered flow revealed a disparity in the upstream turbine yaw angle that improved the net power between the two inflow conditions. This indicated that wake steering controllers must account for the effect of wind veer on the wake behaviour to maintain its efficacy between veered and non-veered flows. Wake models currently used in wake steering controllers were compared with the simulation results and found to insufficiently capture the wake dynamics that occur when turbines operate in veered wind. The outcomes of this thesis highlight the potential implications for wake steering when wind farms operate in veered wind conditions and provide a basis for future development of wake steering controllers, wake models and the applicability of both in realistic, atmospheric flow conditions.

Statement of Originality and Declaration

The content in this thesis is, to the best of my knowledge, entirely my own and has not been submitted for any other degree or purpose.

I certify that the intellectual content of this thesis was produced by myself and any assistance or external sources have been acknowledged. This includes, but is not limited to, the following:

- I worked under the supervision of Associate Professor Michael Kirkpatrick to develop the topic, aims and objectives of this thesis.
- I researched the relevant literature to understand the work that has previously been done and determine the current level of knowledge regarding the effect of wind veer on wakes and potential implications for wake steering.
- I used the open-source Simulator fOr Wind Farm Applications (SOWFA), developed by the National Renewable Energy Lab and based on the OpenFOAM framework as the solver for my simulations.
- The simulations were run on the University of Sydney supercomputer, Artemis, and the National Computational Infrastructure (NCI) supercomputer, Gadi. Access to Gadi was supported by the Sydney Informatics Hub (SIH) High Performance Computing Allocation Scheme.
- I worked with Michael Kirkpatrick, NCI and SIH to install and compile SOWFA on both Artemis and Gadi.
- I implemented the velocity deficit and wake deflection models in MATLAB for comparison with my simulation results. More details on these models and the derivations are provided in Section 3.5 and Appendix A.3.
- I used the open-source application, Paraview to visualise the raw data from the simulations.
- I wrote the MATLAB scripts to process, analyse and produce figures of my results.

Ella KERR

Authorship Attribution Statement

This thesis contains material that was included in the conference paper,

> Analysis of the relationship between wind veer and wake deflection of yawed wind turbine wakes in stable atmospheric boundary layer flow. In *Proceedings of the 23rd Australasian Fluid Mechanics Conference*, University of Sydney, Sydney Australia, 4 - 8 December 2022.

This includes the method for running the simulations and calculating the wake centre, as well as some of the results presented in Section 4.5. As first author, I developed the research objectives, method and simulations, as well as the data processing, interpretation and preparation of figures. This was performed with guidance and advice from my supervisor. I also personally presented the work at the conference.

Ella KERR

As the supervisor for the research upon which this thesis is based, I certify that the authorship attribution statements above are correct.

Assoc. Prof. Michael KIRKPATRICK

Acknowledgements

First and foremost I would like to thank my supervisor Michael. It's been a 3 year long journey that has included an undergraduate Honours thesis, tutoring Thermo 2 twice, tutoring Renewable Energy, many chats about tennis, some exchange of baked goods and now concludes with this MPhil thesis. It has been absolute pleasure to work with you and I hope you enjoy your new teaching focused role and not having to deal with Artemis/Gadi just being super annoying for no reason every now and then. I'd also like to thank Snowy for being a wonderful addition to my weekly Zoom meetings with Michael. Here's a message just for you: woof woof woof bark bark.

Thanks to all the HDR friends I have made in the last two years! Shout out to those in the Futsal team (let's go Legs of Steel!) to Friday lunches followed by Friday pubbing (usually without much time between lunch and the pub). Also big thanks for the support during my run in the 3 Minute Thesis competition, sorry that you had to hear the exact same speech 3 times. To those involved in the very memorable late night/early morning Singstar renditions of Kiss From A Rose and Love Shack, we sure crushed it. I've also managed to do more karaoke this year than in all the years before it because of y'all.

A special thanks to my fellow members of the AMME HDR Crew, Anne, Tara and Athiya. Our group started with the aim to make the HDR experience a more enjoyable one for those in AMME and I can definitely say that this goal was achieved for me. The many events we have run have been a real highlight of my year and I hope the spirit of the group continues into the future.

Thank you to Ruby, Mum and Dad for making me take a break every now and then and ensuring I was always well fed. I know finishing this thesis isn't quite on par with Ruby's wedding, but I expect the level of celebration for it will be matched. Now that this is done though, I have more time to memorise the location and names of oceans to improve our Good Weekend Quiz scores.

Thanks/apologies to whomever may have heard my late night attempts (and successes) to hit the high notes in the titular number from The Phantom of the Opera that I would often practice in S223. It was only after several renditions that I learned that, that room is *not* soundproof.

Finally, thanks to me. I am the Master of the thesis.

Contents

List of Figures

List of Tables

1. Introduction

Anthropogenic carbon dioxide emissions contribute significantly to the global heating and associated changes in climate that have been observed since the industrial revolution [1]. Temperatures across the globe continue to increase, and so the likelihood of catastrophic climate events has also increased. Such events include ocean acidification, flooding, heatwaves, droughts and tropical cyclones, many of which are already affecting the various inhabited regions across the globe [1]. The emissions contributing to global warming are overwhelmingly the result of burning fossil fuels to produce energy [2]. Thus, a key aspect of mitigating catastrophic climate disaster is the shift to renewable energy sources.

In 2015, 192 parties, including the European Union, joined the Paris Agreement, which aims to limit the global temperature increase this century to 2 °C above the pre-Industrial Age level [3]. However, atmospheric concentrations of greenhouse gases has continued to increase year on year [4]. By 2021, the carbon budgets consistent with achieving the Paris goals have been significantly depleted and global warming has already increased to 1.1 °C [5][6]. The focus of the United Nations Climate Change Conference in Glasgow (COP26), was thus on the urgent need for action, including a provision for the phase-down of coal power [2]. This call for action was echoed in the Intergovermental Panel on Climate Change (IPCC) report on 'Impacts, Adaptation and Vulnerability', stating that "further delay in... global action on adaptation and mitigation will miss a brief and rapidly closing window of opportunity to secure a liveable and sustainable future for all" [4].

While this sentiment seems discouraging and the commitments of the Paris Agreement appear unlikely to be met, any reduction in anthropogenic carbon emissions, and thus global warming, is paramount to mitigate a worsened climate catastrophe. In other words, any action that can reduce the impact of climate change is still critical.

The role of electricity generation in powering the world is also becoming more significant with the electrification of services and technology that previously relied on direct sources of fuel. A common example of this is the growing electric vehicle (EV) industry, with EVs outselling diesel vehicles in some parts of the world [7].

Electricity currently contributes to 20% of the world's final energy consumption and is predicted to reach 30% by 2050 [5] and as in 2022, fossil fuels are the dominant source of electricity across the globe, though the uptake of renewable technologies continues to grow each year. From 2018 to 2019, there was a increase of 361 TWh, or 5.5% increase, in global renewable electricity generation [8].

This reflects the continued growth in the renewable energy industry, which has seen a 1447 TWh increase in renewable electricity generation across the globe since 2015 [8]. Solar and wind energy generation have thus far dominated this surge, suggesting that these are the most suitable methods for the needed rapid replacement of fossil fuel electricity sources [8].

Wind is the second largest source of renewable energy behind solar and the third largest when including hydroelectricity. Wind energy is captured using wind farms with the horizontal axis wind turbine (HAWT) the most common turbine design implemented commercially. The International Energy Agency (IEA) predict the onshore wind farm capacity to increase by an average of 75 GW per year from 2021 to 2026 [9]. The potential of wind energy, particularly from offshore, is also vast with a geospatial assessment of offshore wind sites indicating that almost 36,000 TWh per year of electricity could be generated by offshore wind farms, which is close to the projected global electricity demand for 2040 [9].

1.1 Wind Farms in Operation

Wind turbines work on the principle of capturing the kinetic energy in the wind and converting it to electricity [10]. The wind exerts both lift and drag forces on the turbine rotor, causing the blades to rotate, in turn rotating the shaft of a generator enclosed within the hub. In 2019, global electricity from wind turbines accounted for 1412 TWh, which includes a 12% increase in generation from 2018 [8].

In this process of electricity generation, the wind passing through the turbine rotor becomes highly turbulent, low in energy and reduced in velocity in the region directly behind the turbine, known as the 'wake' [11]. The presence of wakes within large wind farms has been observed to cause varying load conditions and a reduction in power production, often referred to as 'wake losses' [12][13]. In large offshore wind farms, the average power loss due to wakes is 10 to 20% of total power output [14]. Given sufficient distance, the wake speed and overall behaviour will recover toward that of the freestream conditions, so turbines in wind farms will be spaced apart in the attempt to reduce wake losses [12]. However, it is generally more economically viable for wind farm operators to group turbines together across a wind farm site with consideration of the electricity transmission infrastructure and land costs [13]. Thus, there must be compromise between turbine spacing and wake losses and the operational and capital costs of the wind farm.

Various strategies have been implemented across wind farms to maximise the power and minimise the performance issues associated with wake losses [11]. Conventional and widely used approaches include optimising the layout of the wind farm to reduce wakes

overlapping with downstream turbines for the given conditions at the wind farm site or finessing the design of the turbine blade for peak performance [15].

In the past few years, the concept of 'active wake control' has been a topic of particular interest to the wind energy research community [16][17][18]. Active wake control (AWC) methods aim to respond actively to the real-time conditions in a wind farm and adjust turbine parameters to optimise the overall farm performance. Examples of AWC include blade pitch control, turbine induction control and wake steering [19]. Thus far, wake steering has shown great promise as a technique to mitigate losses due to inter-farm wakes [11][19][20][21]. Wake steering involves the intentional misalignment, or 'yawing', of the turbine rotor with the inflow wind such that upstream turbine wakes are directed away from the rotors of downstream turbines [11][13]. While the yawed, upstream turbines will experience a reduction in power production relative to if it were not yawed, the aim of wake steering is for the power improvement of the downstream turbine to counter-act this loss, resulting in an overall improvement in wind farm energy yield [13][19][22][23].

Most modern HAWTs are already fitted with yawing actuators and control systems so the rotor tracks perpendicularly to the inflow wind direction, as this yields the greatest proportion of power from the freestream wind [22]. Thus, the implementation of wake steering in commercial wind farms would be relatively simple, requiring only a modification to the wind direction tracking controller [24]. AWC also has the benefit of reacting to changes in the inflow wind conditions such as wind direction and velocity [24], whereas the traditional performance optimisation methods were applied in initial stages of the wind turbine or farm design and cannot be modified later.

The conditions a turbine experiences in real, atmospheric flow varies from those often tested in experiments. In the lowest part of the atmosphere, wind flows as a boundary layer, known as the atmospheric boundary layer (ABL). The ABL is directly affected by the presence of the earth's surface in terms of friction and heat transfer, with its behaviour varying diurnally and over different terrains [25]. It is often characterised as convective or unstable (CBL), stable (SBL), or neutral (NBL) depending on its thermal properties. These different categories also differ in regard to turbulence intensity, buoyancy effects and depth of the boundary layer [25]. The nature of the ABL directly affects the behaviour of the wakes that form in those conditions as it constitutes the inflow and surrounding freestream conditions [26][27][28].

While various wind tunnel and computational tests have indicated that wake steering can lead to an increase in overall farm production, there is still uncertainty regarding the effectiveness of the technique in realistic wind farm site conditions [18]. Some field tests have been performed and demonstrated encouraging results, though these have been limited to include only a small number of turbines and have not investigated the technique

on a full farm scale [20][21]. Similarly, only select ranges of inflow wind directions and atmospheric conditions are generally considered in the analyses. Thus, the observed performance of wake steering in the field so far has not been indicative of the range of conditions that occur at a wind farm [29].

In terms of wind turbine wakes and wake steering, the SBL is particularly of interest due to its impact on wake behaviour. The SBL develops when there is a cooling effect from the surface to the wind, which commonly occurs at night over land and over bodies of water [25]. The SBL exhibits a low level of turbulence and thus wakes tend to propagate for longer distances than in the CBL or NBL as wake recovery depends on the entrainment of momentum from the surrounding freestream flow [27]. This leads to higher wake losses observed in wind farms when the conditions are stable [26]. Similarly, the low turbulence intensity in the inflow results in relatively structured wakes with a clear relationship between wake centre and turbine yaw angle, indicating the potential effectiveness of wake steering in redirecting wakes formed in the SBL [28]. The presence of the SBL over offshore wind farm sites and the corresponding potential capacity offshore wind farms can provide, further indicate the key role the SBL can play in wind energy generation.

The SBL often involves the presence of wind veer, which is the change in wind direction with height. Wind veer occurs due to the Coriolis forcing and atmospheric friction [30]. In the Northern Hemisphere, this results in the wind direction shifting clockwise with increasing height, while in the Southern Hemisphere it shifts counter-clockwise [25]. Observations of wake flow in veered atmospheric conditions suggest that wind veer has an influence on the behaviour of wind turbine wakes [31][32][33][34].

1.2 Wakes and Wind Veer

When veer is present in the inflow wind through a turbine, the wake then demonstrates a degree of veer itself [33][34][35][36][37]. The magnitude and shape of this wake veer depends on that of the inflow wind, though an empirical relationship has not yet been derived. This translates to the location of the maximum velocity deficit being deflected in different directions at different heights generally following the same direction as the inflow veer profile [32][33][35]. For wake steering to be most beneficial, the technique must be deflecting the wake regions of maximum deficit to ensure the conditions for downstream turbines are more favourable than if the technique were not imposed. Therefore, accurate prediction of the wake centre is required so the controller is not producing sub-optimal or detrimental flow conditions at downstream turbines.

Wake models simplify the complex wake characteristics into several key parameters, often the wake expansion rate and the velocity deficit for given distances downstream from

the turbine [11][38][39][40]. The relationships between the wake parameters have been determined either experimentally or through analytical studies to provide an indicative representation of the wake behaviour.

Wake steering controllers typically utilise analytical or empirical wake models, coupled with optimisation algorithms, to determine the optimal yaw set-points for given conditions [16]. High fidelity methods such as computational fluid dynamics (CFD) are not used in these wake steering controllers as they require significant computational resources and time for simulations, which is not conducive to a controller that responds actively to instantaneous conditions. Thus, parametric wakes models, albeit lower in fidelity, are used as they can quickly provide results [12][40].

It then becomes important for the wake model to be effectively and accurately capturing the wake behaviour, including the dynamic relationship between wake characteristics and the inflow wind features such as wind veer. There is a consensus among those who have studied the relationship between turbine inflow and wake veer that low-order wake models should include this effect to improve wind farm optimisation and thus performance [28][33][34][37].

The uncertainty regarding the effectiveness of wake steering under realistic conditions is a hindrance to the technique being implemented commercially and so potential improvements to wind farm performance are being missed. The wake models currently used in wake steering controllers do not account for the effect of wind veer on wake behaviour and have not been tested for their efficacy in veered flows. Testing the models against data from a range of yawing and veer conditions would identify the shortfalls of the current models and could lead to modifications to wake steering controllers. This would improve the validity of the wake steering in realistic atmospheric flows and further the progression of wake steering from theoretical concept to widely utilised wind farm optimisation technique.

1.3 Research Objectives

This research aims to understand and analyse the relationship between wind veer and the wake behaviour from yawed wind turbines. In particular, this thesis investigates how wake models could be modified to better represent realistic wakes when conditions involve wind veer and the potential implications for wake steering as the inflow wind veer varies. This will be achieved by simulating the wakes produced under varying wind veer profiles and for different yaw angles. It will also consider the implications of wind veer on the effectiveness and accuracy of wake steering controllers by investigating how well currently used wake models capture the dynamics of wakes produced in veered flow. Several analytical wake models will be implemented and compared with the results obtained from

the simulations to observe how well wake features such as the shape, velocity deficit and deflection are represented by the models when the inflow wind involves wind veer.

The outcomes of this thesis will contribute to understanding how wake dynamics vary based on the wind farm inflow conditions. This will help to improve the effectiveness of wake steering when operating in realistic flow conditions and bring the technique closer to implementation in commercially operating wind farms. As the world shifts its reliance on traditional, fossil fuel sources of energy to renewable technologies, wind energy is likely to be a major source of electricity across the globe. Thus improving the efficiency of wind farms is necessary to ensure the power demands of the future can be met.

1.4 Thesis Outline

The structure of this thesis is as follows, Chapter 2 provides background information and reviews the literature currently available on wind turbines wakes, the atmospheric boundary layer and how wakes are influenced by wind veer. Chapter 3 outlines the methodology used to simulate the stable atmospheric conditions using a CFD solver, varying the wind veer profiles and locate the wake centre. The analytical models currently used in wake steering controllers that are being compared with the simulation results are also presented. Chapter 4 presents the results from the simulations and wake models with an analysis on features such as wake shape, wake deflection and turbine power production. These results are discussed further in Chapter 5 with a particular focus on the implications of wind veer for the current approach to wake steering. Finally, Chapter 6 summarises the findings of this thesis and suggests avenues for future research into the topic of wake steering in veered conditions.

2. Literature Review

2.1 Wind Turbine Wakes

As energy is extracted from the wind passing through the turbine, the velocity of the wind decreases and a slower region of flow forms behind the turbine known as the 'wake'. The wake is characterised by increased turbulence and a lower velocity relative to the freestream wind [10]. While all wakes share the same overall features, aspects of the wake behaviour will vary between different turbines and different wind farms, with factors such as turbine type, yaw angle, terrain and atmospheric wind conditions affecting the wake flow. The presence of turbine wakes within wind farms can affect various farm performance metrics and thus control strategies are often implemented to mitigate any issues. The use of computational fluid dynamics (CFD) and simplified wake models have been employed across the wind energy research community to analyse wake effects. Such methods are often more accessible and carry a lower cost than field or experimental methods and thus have become a popular choice for investigating wind turbine flow. Parametric, experimental, and analytical wake models also play a key role in the development and implementation of wake control strategies.

2.1.1 Formation and Features

Wind turbines generate power by converting the kinetic energy in the wind to mechanical energy and then electrical energy via the rotor and generator, respectively [10]. Some common features of the wake include a 'near' and 'far' wake region, velocity deficit, wake rotation, wake centre and wake recovery.

The near wake occurs within approximately one to four rotor diameters from the turbine, with the far wake being the region further downstream [31][41]. The near wake is affected by the physical characteristics of the turbine such as the blade profiles and geometry of the nacelle and hub [41]. The maximum velocity deficit of the wake is found in the near wake region, occurring within one to two diameters downstream from the turbine [42]. The near wake is highly complex and thus difficult to model.

The far wake region is less dependent on the physical specifications of the turbine rotor, but rather more affected by the wind inflow conditions [10]. When analysing the impact of turbine-wake interactions in wind farms, it is the far wake region and its features that are considered, given turbines are generally spaced at distances greater than the near wake

region length [12][41].

The direction of rotation of the near wake is opposite to that of the turbine blades due to the conservation of angular momentum [42], with the magnitude of rotation decreasing as the wake travels downstream [43]. The wake rotation also induces a slight deflection in the wake when the inflow wind velocity is sheared [42]. As most modern horizontal axis wind turbines (HAWTs) have clockwise rotating blades, the wake rotates counter-clockwise and when viewed from upstream, appears to drift towards the right as it travels downstream. This occurs as the slower wind near the ground is transported up to the right side of the wake, while the faster wind near the top of the rotor is transported down to the left side. As the momentum on the right side of the wake is lower, the wake deflects to the right [11][19]. Henceforth in this thesis, the terms 'right' and 'left' refer to directions relative to the turbine when viewed from upstream. The rotating wake also acts as a vortex, which interacts with the ground and contributes to this wake deflection occurring in un-yawed turbines [19].

In cases of boundary layer flow that involve shear and the presence of ground, the vertical profile of velocity in the wake still resembles a Gaussian distribution, as has been observed in uniform flow conditions [44]. However, variations from the Gaussian distribution were observed near the edges of the wake, due to the stratified inflow velocity. The self-similarity aspect of a Gaussian distribution has allowed for simple analytical models to effectively represent the mean flow distribution in the far wake, as will be discussed further in Section 2.1.5.

2.1.2 Behaviour

The wake can be deflected by changing the relative angle between the turbine rotor plane and inflow wind direction [13][45]. This can be achieved through yawing the turbine, which is rotating the turbine about the vertical axis, and through pitching the turbine rotor up or down [19]. Changing the rotor angle introduces an additional force, in the example of yawing this acts laterally to the flow and for pitching the force induces vertical deflection [13]. The direction of this deflection is shown in Figure 2.1 for yawing. The cross-sectional area of the wake from yawed turbines appears to be curled, or 'kidney-shaped', rather than the more circular, symmetric wake shape produced by turbines not in yaw. LES studies by Vollmer *et al.* [28] noted this change in wake shape, as did Howland *et al.* [46] in an analysis of wake flow using LES with the actuator disk model (ADM) and the actuator line model (ALM), and experimentally using a porous actuator disk in a wind tunnel. Lidar scans performed by Fleming *et al.* [47] on a full scale wind turbine also revealed wake deflection due to yawing and a curled wake shape.

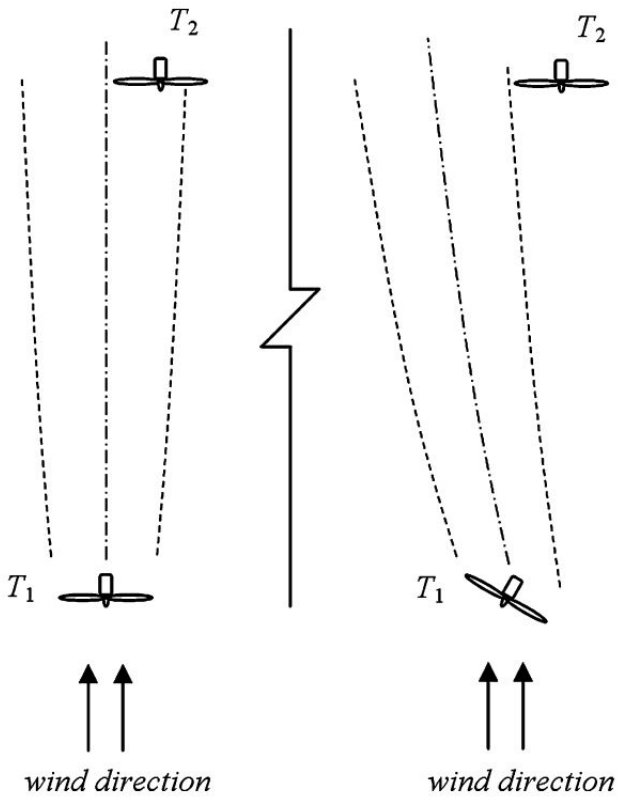

Figure 2.1: Schematic of wake deflection due to turbine yawing from [13].

The cause of this wake curling has been linked to the shedding of a counter-rotating vortex (CRV) pair from the top and bottom tips of the yawed rotor [39]. Bastankhah and Porté-Agel propose this CRV pair occurs to maintain continuity in a flow with strong variation in the cross-stream velocity [39].The presence of the CRVs has also been linked to the phenomenon of 'secondary steering', wherein the wakes from un-yawed turbines exposed to the deflected wakes from yawed turbines upstream will exhibit their own degree of wake deflection [48]. In arrays with multiple, yawed turbines, the cross-stream velocity components appear to merge and compound with each yawed turbine [48]. This suggests that wake deflection is occurring in part due to the yaw of the turbine and due to the presence of the CRV pair.

As outlined above, modifying the turbine parameters, such as the yaw angle, causes such variations in wake behaviour. Similarly, as the inflow conditions change, so too does the wake. Wake meandering refers to random, unsteady fluctuations of the whole wake relative to the time-averaged wake centre-line [12]. These fluctuations are caused by turbulent structures in the atmospheric inflow, that are larger than the turbine diameter and present as oscillations of the whole wake [49]. The relationships between wake behaviour and the consistently changing atmospheric boundary layer (ABL) are explored further in Section 2.2.

2.1.3 Wake Losses

The power produced by a wind turbine is given by,

$$P = \frac{1}{2} C_P \rho A U^3 \tag{2.1}$$

where C_P is the coefficient of power, ρ is the air density, A is the swept area of the turbine rotor and U is a representative inflow wind speed. From this equation, the relationship between power production and wind speed of the turbine inflow is clear, with higher velocities corresponding to higher power. A 'cut-off' wind speed will exist for each turbine model and represents the limitations of the turbine generator at increasing wind speeds [42]. So higher wind speed does not necessarily indicate higher delivered power, however wind speed magnitude provides an indication of the available power in the wind resource. It should also be noted that there is a 'cut-in' wind speed, below which the turbine will not operate [42].

While the turbines located near the outer edges of the wind farm are likely to experience the freestream wind conditions, this is generally not the case for the turbines near the centre of the farm. Instead, these turbines are often exposed to the low velocity, highly turbulent wakes from upstream turbines and, per Equation 2.1, produce less power than those exposed to the freestream conditions as there is less energy available in the inflow. This is known as 'wake losses' and refers to the reduction in power produced by a wind farm due to the presence of upstream turbine wakes propagating through downstream turbines relative to the situation in which all turbines were exposed to the freestream wind flow.

Ideally, turbines would be spaced to allow sufficient recovery of the wake between rows, however, to minimise costs associated with land use and transmission, turbines are grouped together, resulting in interference effects and wake losses [13]. In large wind farms, this can have a significant impact on overall farm power production. Barthelmie *et al.* [14] observed the power losses due to the presence of wakes in large offshore wind farms to be on the order of 10 to 20% of the total power. In an LES study of various wind farm layouts and turbine spacing combinations, Ghaisas *et al.* [50] noted a variation in the effect of wake losses on the power production. Testing different wind farm layouts, improvements in power production were observed to vary by 13 to 33% depending on the chosen layout [51].

To combat wake losses, control strategies can be implemented at different points throughout the wind farm development, design and operation stages. These methods have ranged from turbine layout optimisation to blade design to the more recently suggested active control strategies [15]. For the former approaches of layout or blade optimisation,

this is implemented during the construction of the wind farm or turbines and are then effectively locked in, regardless of how the wind resource changes at the farm site over time. Whereas active control strategies respond to the changing inflow wind conditions and aim to adapt the turbine parameters such that the wind farm is consistently operating at peak performance. A current promising and viable proposal for active wake control (AWC) is wake steering.

2.1.4 Wake Steering

Wake steering is a relatively recent technique that aims to improve the overall wind farm power production. The method involves intentionally misaligning the turbine rotor with the inflow wind direction to deflect the wake away from downstream turbines [13][19].

A common feature of modern HAWTs is the ability of the turbine to track the inflow wind direction and aim to maintain orthogonality between the rotor and inflow wind vector [42]. The power production of an individual turbine is maximised when the turbine rotor is perpendicular to the inflow wind and so direction tracking is implemented on the basis of maximising individual turbine power [45]. Wake steering, on the other hand, aims to increase the overall power production of the farm by improving the flow conditions between turbines via collaborative turbine control [13][45]. The implementation of wake steering is also seemingly straightforward for currently operating wind farms as turbines are already fitted with yaw controllers [16], suggesting that this method can be applied to farms already in operation.

Wake steering has been investigated via numerical [11][19], experimental [52][53] and field methods [20][21][54]. The technique has demonstrated potential to deflect turbine wakes and improve power production of turbine arrays and wind farms, though has yet to be implemented in a commercially operating wind farm.

Fleming *et al.* [19] observed the horizontal wake offset to increase in magnitude with increasing yaw angle magnitude. Similarly, the reduction in power produced by the yawed turbine also increased for larger yaw angles. For wake steering to yield an improvement in farm efficiency, this loss in power produced by the upstream, yawed turbine must be overcompensated by the increase in downstream turbine power.

In a CFD study, optimising the yaw angles of turbines in a small wind farm based on static wind conditions yielded a 15% increase in power production [11]. Archer and Vasel-Be-Hagh concluded from their LES analysis of a 28-turbine wind farm that power production gains from wake steering were statistically significant when at least two turbines were downstream of the yawed turbine [55]. They also note that for negative yaw angles, the wake steering implementation was not effective and relate this finding to the influence

of the Coriolis force on the wake deflection. This trend has similarly been observed in a number of studies and is discussed further in Section 2.3 [32][53][56].

Schottler *et al.* [52] performed wind tunnel tests to analyse the wake behaviour of a yawed turbine and noted the generation of a curled, 'kidney-shaped' wake cross-section downstream of both the turbine models tested. While the lateral displacement direction of the wake centre was similar for the two models tested, the direction of vertical displacement differed, with the authors relating this variation to the opposing blade rotation directions implemented. In wind tunnel tests of a two-turbine array under boundary layer flow, Campagnolo *et al.* [57] observed increases in power produced by the downstream turbine. The greatest increase of 21% was achieved when wake steering was combined with offsetting the downstream turbine laterally.

Field tests of wake steering controllers have resulted in improved total power production for a range of the wind directions observed at the site [54]. Howland *et al.* [45] implemented pre-determined, optimised yaw angles based on prior operational wind data for the site of a 6-turbine array and calculated the increase in annual average power production to be between 7 and 13% for selected wind directions at night. Fleming *et al.* [21] also tested a controller that accounted for the dynamic behaviour of the turbine yaw actuator and instantaneous changes in the wind direction. This approach resulted in a reduction in the recorded wake losses by 6.6% when implemented for specific inflow wind directions.

While wake steering appears to be a promising solution to wake losses, it is not yet clear how effective the method is for varying wind conditions, with a survey of wind farm experts across academia and industry outlining the need for analyses of wake steering in more realistic wind conditions [18]. Wake steering controllers generally involve a look-up table or database of the optimal yaw angle to improve farm power for a given wind direction. These optimal angles are pre-determined by applying an optimisation algorithm to the results from simple wake models of the farm layout or turbine array operating in various wind directions. By improving the wake models used in wake steering controllers, the technique applicability to real wind conditions would similarly be improved.

2.1.5 Wake Modelling

To study wake features, wake behaviours and how turbines interact with the wind flow, the effect of the turbine blades on the fluid flow is often modelled. This can be achieved using computational fluid dynamics (CFD) or parametric wake models.

Computational Fluid Dynamics

CFD methods solve the discretised Navier-Stokes equations to simulate the behaviour of fluid flow using numerical methods. The Navier-Stokes equations describe the conservation of mass and momentum of fluid motion, with an equation for each direction of motion. The general equations for mass and momentum conservation are given below and the terms are discussed in more detail in the Methodology Section 3.1.

$$\partial_\alpha u_\alpha = 0 \tag{2.2}$$

$$\partial_t u_\alpha + \partial_\beta u_\alpha u_\beta = -\frac{1}{\rho}\partial_\alpha P + \nu \partial_\beta \partial_\beta u_\alpha \tag{2.3}$$

Here u is the velocity vector, ρ is the density of the air, P is the air pressure, ν is the air viscosity. The terms on the left hand side of the equation are the convective terms, with the first term being the transient changes in velocity and the second term representing convection. The right hand side of the equation includes the diffusion terms, with the first term on the right representing the pressure gradient and the last term in the equation describing diffusion.

Some approaches to solving the Navier-Stokes equations via numerical methods include Reynolds Averaged Navier-Stokes (RANS), Large Eddy Simulations (LES) and Direct Numerical Simulations (DNS). RANS considers the statistically steady behaviour of turbulent flow via solving the time-averaged Navier-Stokes equations,

$$\partial_t \overline{u}_\alpha + \partial_\beta \overline{u}_\alpha \overline{u}_\beta = -\frac{1}{\rho}\partial_\alpha \overline{P} + \nu \partial_\beta \partial_\beta \overline{u}_\alpha - \partial_\beta \overline{u'_\alpha u'_\beta}. \tag{2.4}$$

The above equation is in Cartesian form, with summation over repeated indices implied and the overbar to represent time averaging. The last term in this equation is specific to RANS simulations and is the Reynolds stress term, which is approximated via a turbulence model. Compared to LES and DNS, RANS is the least computationally intensive approach, however it is lower in fidelity and instantaneous results cannot be obtained.

LES resolves only the larger scale turbulent eddies in the flow and, similarly to RANS, approximates the smaller, diffusive eddies via a turbulence model. It is the larger eddies that contain more energy and are involved in the transport of the flow characteristics [58]. LES can provide results on the transient behaviour of the flow and capture the vortex structures within the wake. LES requires more computational resources than RANS, but less than DNS and so is a popular choice for obtaining detailed results of wind turbine wake behaviour [59].

DNS solves the Navier-Stokes equations directly, without the use of turbulence mod-

els, and thus produces results of greater accuracy than LES and RANS. However, this requires a much finer grid resolution to capture the larger turbulent eddies and the much smaller, Kolmogorov scales in the flow at which viscosity is dominant and so DNS is very computationally intensive and thus expensive [60]. The range of scales involved in wind turbine simulations, from the blade boundary layer to the distance between turbines due to the high Reynolds number for the fluid flow, is too large for DNS to be used practically [13][61].

Current common methods for modelling a wind turbine rotor in CFD flows include the actuator disk method (ADM), actuator surface method (ASM) and the actuator line method (ALM). These three methods share the core concept of representing the turbine interaction with the freestream wind via forces projected onto the discretised flow field, but vary in the specific method implementation, fidelity and the flow features resolved. The ALM is discussed in more detail in Method Section 3.3.2.

Parametric Wake Models

Wake models provide an even faster, albeit lower fidelity, means to approximate the turbine wake and its behaviour than CFD. The concept of a wake model is to simplify the complex wake characteristics into several key parameters, most notably wake expansion and velocity deficit, with either empirically or analytically determined relationships to link them. This allows for wake features to be computed or visualised relatively quickly compared with the more computationally and time intensive CFD approaches.

The Jensen wake model [38] is the most well-known and simple wake model, derived from the conservation of momentum in the far wake and field results on the wake recovery rate. A 'top-hat' approximation is implemented for the wake velocity deficit and a linear wake expansion pattern is assumed for the wake shear boundary [38]. While the simplicity of the Jensen model allows for easy calculation of wake behaviour, it has been found to overestimate the velocity deficit for the outer regions of the wake cross-section and does not account for the effect of inflow turbulence on velocity deficit [23][62].

The Gaussian wake model (Gaussian model) by Bastankhah and Porté-Agel provides a more realistic representation of a wake compared with the Jensen model via the Gaussian wake deficit profile and incorporation of inflow turbulence in the wake recovery calculation [39]. This model was determined from a budget analysis of the Reynolds Averaged Navier Stokes (RANS) and observations of turbine wakes as developed via wind tunnel experiments. The Gaussian model has been implemented in several wake steering controller tests as the current wake model of the FLOw Redirection In Steady-state (FLORIS) simulator [17][20][29]. FLORIS previously utilised a parametric model proposed by Gebraad *et al.* [11], which considered the wake to comprise of three distinct regions including a near

wake, far wake and mixing zone to better represent the scenario of downstream turbines experiencing partially waked inflow conditions. The difference between these wake zones is reflected in the calculation of the velocity deficit and cross-sectional area of the zone.

To capture the wake deflection associated with turbine yawing, wake models may include an additional relationship between the yaw angle and wake centre offset. An early example of this is from Jiménez *et al.* [13] (Jiménez model), which uses a top-hat velocity deficit distribution assumption as per the Jensen and Katic models alongside a wake skew angle model based on the conservation of momentum. Although their results demonstrated satisfactory agreement with experimental results, the authors noted that further validation of the model is required. Qian and Ishihara later suggested that the Jiménez model overestimates the wake centre offset due to the inaccuracies associated with the top-hat velocity deficit distribution assumption [63]. Blondel *et al.* [64], similarly note the discrepancy between the Jiménez model results from measurements and high-fidelity simulations. They suggest the deviations to arise from a combination of insufficient model calibration and the constraints of the underlying model assumptions.

Similar wake deflection models proposed by Gebraad *et al.* [11] and Howland *et al.* [46] are based on the integration of the skew angle relationship presented by Jiménez *et al.* [13]. Thus, these models would also be influenced by the errors in the underlying Jiménez model. Bastankhah & Porté-Agel derived an alternative deflection model as part of the Gaussian model, which showed good agreement with experimental data and considers the influence of inflow turbulence on wake development [39]. Though this deflection model, like ones previous, also assumes the deflection to increase linearly with downstream distances which is not observed in the field [64].

Newer wake models tend to adapt already established and implemented models to include additional phenomena that can influence the wake deflection. King *et al.* [40] introduced a modification proposed by Martinez-Tossas *et al.* [65] to incorporate the effect of secondary steering and yaw induced recovery in the Gaussian model. While the underlying wake deflection component of the Gaussian model is still based on a linear relationship, the incorporation of these additional wake behaviour features better reflected the realism of wake flow. This resulted in a model that compared better with LES results than the unmodified Gaussian model, with King *et al.* [40] suggesting its potential to improve the performance of wake steering controllers and thus farm power production.

2.2 Wakes and the Atmospheric Boundary Layer

Wind turbines operate in the atmospheric boundary layer and the nature of the wind flow through the rotor is thus susceptible to atmospheric conditions. The ABL is often

characterised as neutral, stable or unstable depending on features such as the vertical potential temperature profile and degree of turbulence present in the atmosphere at a given time. The stable boundary layer is of particular interest in the study of wind farm performance given the observed higher wake losses and longer rate of wake recovery compared with neutral and unstable conditions [27]. The SBL also often features wind veer, which is the change in the wind direction with height and is a core concept explored in this research [66].

2.2.1 Atmospheric Boundary Layer

The Atmospheric Boundary Layer (ABL) occurs in the lowest region of the atmosphere. The structure and behaviour of the ABL varies diurnally and seasonally, and is affected by local topographies, terrain and heat transfer from the Earth's surface [67]. Figure 2.2 depicts several key features of the ABL and how it changes through the course of the day.

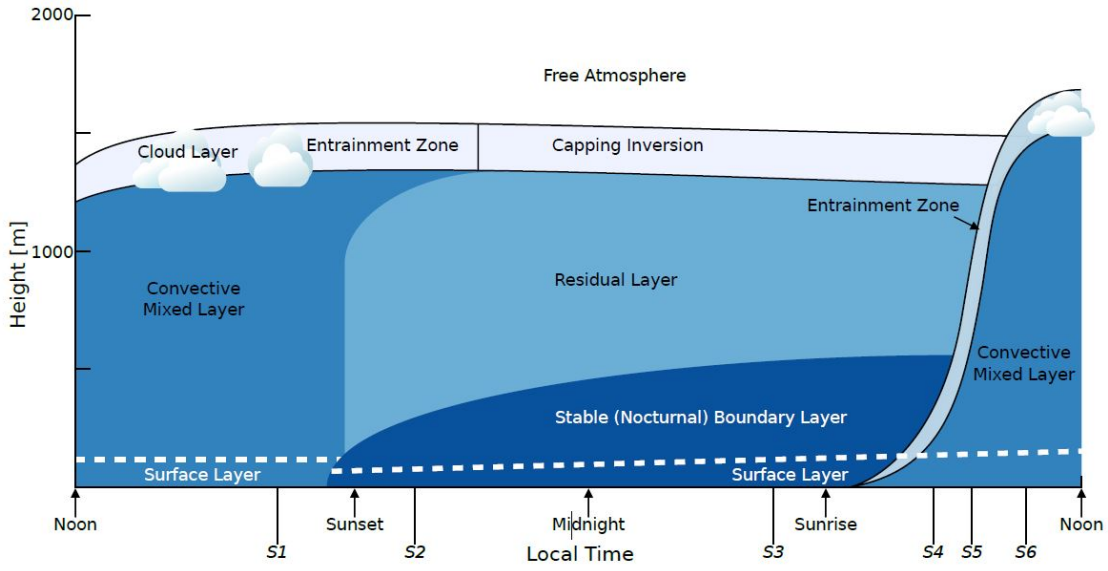

Figure 2.2: Schematic of the diurnal changes in the ABL from [68].

The ABL is often categorised as either neutral (NBL), stable (SBL) or convective (CBL) according to the flow potential temperature profile, as shown in Figure 2.3 [26].

Potential temperature, θ, is a measure of temperature that removes the effect of pressure changes due to altitude. It is given by the following equation,

$$\theta = T\left(\frac{P_0}{P}\right)^{R/C_P} \tag{2.5}$$

where T is temperature, P_0 is a reference pressure, P is pressure, R is the gas constant and C_P is the specific heat capacity of air. As an air parcel flows over large obstacles

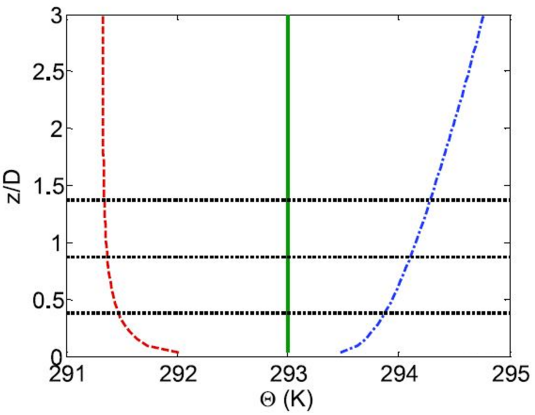

Figure 2.3: Vertical profiles of potential temperature for convective (red), neutral (green) and stable (blue) atmospheric conditions from [27].

such as hills or mountains, it will experience a change in temperature due to the change in altitude and pressure, though the potential temperature will remain constant [69]. Air parcels of the same potential temperature can be exchanged without work or heat input and so lines of constant potential temperature are considered to be natural flow pathways [25]. The motion of air parcels in the atmosphere varies between the NBL, SBL and CBL and thus is used as a method to categorise the boundary layer flow.

The convective mixed layer, or unstable boundary layer, forms when there is heat transfer from the surface to the air above [69]. This generally occurs during the day as radiation from the sun heats the surface of the Earth, which then transfers heat to the air via convection [25]. It can also develop when cool air flows over warm ocean water. This transfer of heat results in a negative gradient potential temperature profile, with potential temperature decreasing with height, as shown in Figure 2.3. This negative profile gives rise to positive buoyancy, wherein warm air parcels rise as they are less dense than their surroundings [25]. At the top of the ABL is the 'entrainment zone', across which the air parcels are entrained from the free atmosphere into the BL [25]. As the warm air parcels in the CBL rise, they mix with the sinking cooler air from the free atmosphere above, leading to a well-mixed boundary layer. This mixing gives rise to a BL with enhanced turbulent kinetic energy and vertical transport of momentum, heat and moisture [25][27]. It is also the mechanism by which the BL grows in depth, leading to a much thicker BL than the SBL or NBL.

The boundary layer most often replicated in lab or experimental settings is the NBL. The NBL is characterised by zero-gradient thermal stratification, with the potential temperature staying constant with increasing height [69]. This profile is easier to replicate than the SBL or CBL thermal profiles and so experimental investigations on atmospheric flows, particularly ones that also consider the presence of a wind turbine, will involve boundary conditions similar to the NBL. In reality, the NBL only arises under certain conditions and may not persist for long periods of time. It is often observed in the transition from the CBL to the SBL after sunset and as such the level of turbulence in the NBL falls between that of the CBL and SBL, with turbulence generation due to shearing as the dominant mode for turbulence production [27].

The SBL generally develops at night or when warm air passes over cool bodies of

water due to surface cooling [26]. It is characterised by negative buoyancy, whereby the vertical motions of the turbulent eddies generated due to shear are suppressed and thus the conditions are low in turbulence [70][71]. The SBL and its influence on wind turbine wakes are discussed in more detail in Section 2.2.2 as it is the interaction between wind turbines and the SBL in the context of wake steering that is of particular interest for this research.

The lowest part of the ABL is the surface layer, also known as the Prandtl layer, which occurs in all categorisations of the ABL and is where turbines operate. In the surface layer, turbulent generation by shear effects dominates and there is little variation in the magnitude of the turbulent fluxes and stresses [67]. The residual layer that forms above the SBL at night is essentially the residual of the CBL, containing moisture and trace particles from the CBL of the previous day [67]. It is less turbulent than the CBL, though more turbulent than the SBL and exhibits a neutrally stratified thermal profile. It is also unaffected by turbulent transport of properties near the surface as it does not have direct contact with the ground.

In 2019, the average wind turbine had a 120 m rotor diameter and a hub height of 90 m [30]. By 2021, the largest wind turbine in production was the General Electric Haliade-X which was 220 m in rotor diameter with a 260 m hub height [72]. As turbines grow in size, the breadth of the ABL the rotor covers also increases and so too does the exposure to more complex regions of atmospheric flow [30].

The ratio of occurrences of the CBL, NBL and SBL was observed to be 40%, 20% and 40% at an offshore wind farm in the Baltic Sea [73]. Wind turbines thus experience a range of atmospheric conditions throughout operation and the performance of a wind farm is dependent on the wind conditions of the site. In particular, the effects of wind shear in direction and velocity across the rotor and level of turbulence in the freestream flow have a great impact on power production, blade loads and wake behaviour [27][69][74].

Notably, the rate of wake recovery varies between the atmospheric stabilities. Wakes recover faster in highly turbulent flows compared with more laminar flows as the entrainment of momentum from the freestream conditions surrounding the wake region is enhanced [28]. Correspondingly, the expansion of the wake is turbulence dependent with convective conditions leading to wake growth rates up to 2.4 times larger than wakes produced in stable conditions [27]. The persistence of wakes downstream directly relates to the wake losses experienced in a wind farm. In conditions where wakes recover faster, such as convective conditions, the wind farm is more efficient than when operating in stable conditions [28]. Hansen *et al.* [75] observed a dependency on stability for the power production of an offshore wind farm, with the turbulence intensity and wake width varying with stability.

Vollmer *et al.* [28] investigated how wake deflection due to yaw misalignment is influenced by the stability of the atmospheric flow. The authors note that the magnitude of the wake deflection and the shape of the wake vary between the three stability categories, effecting the power production of all turbines within a wind farm. This has been similarly observed in various other studies and reveals potential implications for the effectiveness of wake steering across the diurnal cycle [20][28][31][53].

2.2.2 Stable Boundary Layer

The stable boundary layer (SBL) is specifically important in the study of wind turbines and wake behaviour. The SBL typically develops after sunset, when in the absence of radiative heating of the Earth's surface, cooling occurs between the surface and the air above [69]. The potential temperature profile then shifts to be of positive gradient, increasing with height and so, opposite to the CBL, stable stratification occurs. Unlike the enhanced mixing observed with the unstable stratification in the CBL, this stable stratification suppresses the vertical motion of air parcels, ultimately dampening turbulent structures [25]. So, the SBL is characteristically low in turbulence with predominantly shear generation between the wind and the planetary surface acting as a source of turbulence [25][69]. The SBL tends to be lower in depth than the CBL, with the 'top' of the BL being undefined and instead blending into the residual layer [67].

Given the entrainment of momentum from the surrounding freestream conditions into the wake drives wake recovery, wakes produced in the SBL propagate for longer distances downstream than those observed in the CBL or NBL [27]. At the offshore Nysted wind farm, a reduction of up to 9% in wind-farm efficiency was observed by Barthelmie and Jensen in stable conditions relative to convective conditions [73]. Churchfield *et al.* [26] found that the ratio of power produced by upstream and downstream waked turbines is 15-20% higher when conditions are convective relative to when they are neutral.

The deflection of the wake due to yawing is more prominent in the SBL compared with both the NBL and CBL. The wake deflection has been found to increase with increasing thermal stability [26][28] and decreased inflow turbulence [39]. Vollmer *et al.* [28] noted a correlation between turbine yaw angle and wake deflection when exposed to stable conditions. Whereas, in convective conditions, the wake deflection appeared to be independent of any applied yaw angle, suggesting the technique of wake steering to be most viable for offshore wind farms or when stable conditions are present [12].

Low level jets (LLJ) are observed in the SBL. These are, as the name suggests, regions of flow close to the ground with wind speeds higher than the geostrophic wind. The height of the LLJ can vary from 90m to 300m, depending on the stratification of the

boundary layer [76]. High stratification corresponds to a lower LLJ, while low stratified flow corresponds to a higher LLJ. Wind turbine hub heights are on the order of 90m and so an LLJ may occur above or across the top section of a wind turbine rotor.

The LLJ location also influences wake behaviour in terms of recovery rate and cross-sectional asymmetry. When the LLJ is above the turbine rotor, there is greater potential for vertical transfer of momentum from the higher speed jet into the low velocity wake [76]. Whereas, when the jet is near hub height the wake shape becomes asymmetric due to the highly variable inflow velocities across the rotor. The wake recovery is slower compared with the higher placed LLJ as there is less available momentum in the flow above the wake region. LLJs also present issues in terms of turbine blade loads and exposure to such high wind speeds can damage the turbine rotor.

2.2.3 Wind Veer

A prominent feature of the SBL is the change in wind direction with height, known as wind veer or directional shear. Wind veer is present in atmospheric flows as the balance of forces change. Above the ABL, wind flows with a balance between the pressure gradient and Coriolis forcing, resulting in geostrophic winds, which flow along lines of constant pressure [30]. Closer to the Earth's surface, however, the wind experiences friction with the surface, disrupting the force balance and so it flows at an angle to the geostrophic wind direction and at a different magnitude. The stronger the frictional force, the higher the angle between the surface wind speed vector and the geostrophic wind vector increases, and the magnitude of the surface wind speed decreases [77].

According to Svensson and Holtslag [77], the magnitude of this angle, ψ, is,

$$\cos\psi = \frac{fh\overline{v}}{u_*^2} \tag{2.6}$$

where f is the Coriolis parameter, u_* is the frictional velocity, h is the ABL height and $\overline{v}$ is the averaged cross-stream velocity component in the ABL flow. As altitude increases, the effect of friction diminishes and winds accelerate. This ultimately appears as the wind direction rotating with increasing height. In the Northern Hemisphere, winds rotate clockwise when viewed from above, whereas counter-clockwise rotation is seen in the Southern Hemisphere, and this is called 'veering' flow. 'Backing' flow is when winds rotate counter-clockwise (clockwise) in the Northern (Southern) Hemisphere and occurs due to cold air advection [30].

2.3 Wakes and Wind Veer

The relationship between wind veer and the behaviour of turbine wakes is yet to be extensively investigated, though some recent studies indicate that the presence of wind veer in the inflow wind will affect the behaviour of the turbine wake.

The change in direction of the freestream wind velocity vector with height corresponds to an asymmetry in the development of the turbine wake [35]. Bromm *et al.* [35] demonstrate a wake shape that expands in the same direction as the inflow wind veer, though the extent of this stretching is less than the direction change in the inflow wind. The proportional relationship between the inflow wind veer and the wake veer was beyond the scope of their study and has not yet been quantified. A key outcome of the LES investigation by Bromm *et al.* [35], is that the wake of a turbine in veered wind flow will exhibit deflection in different directions and magnitudes at various heights across the rotor, as depicted in Figure 2.4.

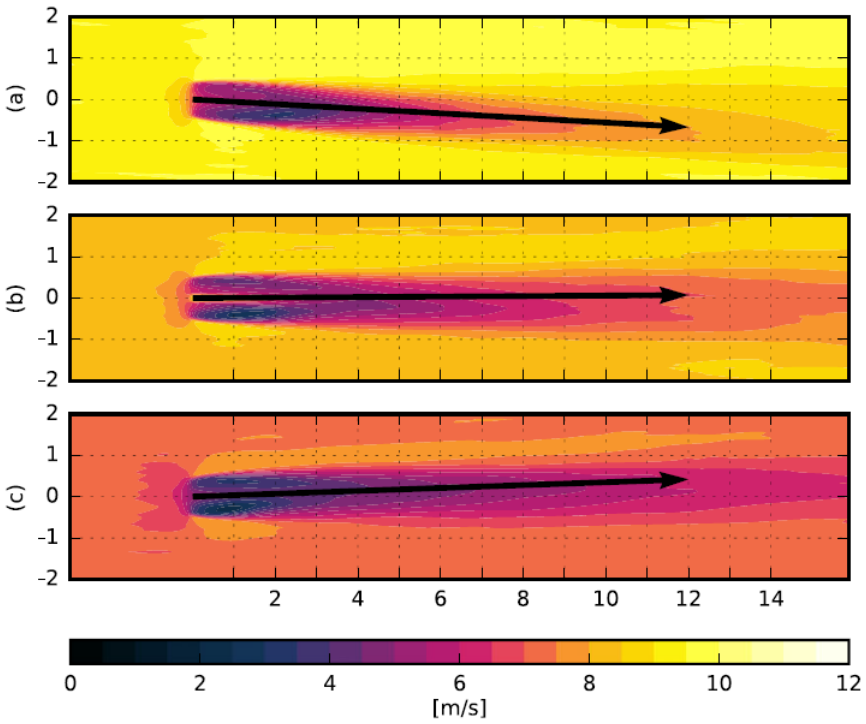

Figure 2.4: Velocity contours of turbine operating in veered wind flow at a) one quarter diameter above hub height b) at hub height and c) one quarter diameter below hub height from [35].

A similar trend was observed in field experiments by Bodini *et al.* [33], who note the angular change in wake centre-line with height occurs at a magnitude of half or less than the angular change in wind direction in the inflow, though the ratio of wake veer to inflow veer decreases as the wake propagates downstream [34]. The authors suggest that the difference in inflow veer and wake veer may be due to the interaction of the inflow veer and

the turbine blade rotation. They also observed the magnitude of wake veer from turbines on the outside of the wind farm to be greater than in wakes from inner turbines of the farm [33].

Englberger *et al.* [78] noted that wakes from veered inflow exhibit a degree of veer themselves and tested the wake behaviour for various shapes and vertical gradients of inflow veer profiles. Veer was applied over the top, bottom or entire rotor and the authors observed the wake veer to occur in response to the location of the inflow veer. For example, wind veer across the bottom of the rotor resulted in wake veer in the region nearer the ground. The extent of the wake veer for different inflow veer profiles was also seen to vary. Veer only in the lower rotor half corresponded to wake veer at a lower magnitude than the inflow, whereas veer across the upper rotor led to a ratio between the inflow veer and wake veer close to 1 [78].

Comparing the clockwise (CW) and counter-clockwise (CCW) rotation of the blades for turbines in veered flow demonstrated that the proportion of inflow veer to wake veer is affected by rotation direction [36]. In CBL flow without veer, the blade rotation only has a minor effect on the wake behaviour, which seems to be concentrated in the near wake region [41][79]. Whereas in SBL veered flow, rotational direction impacts the wake recovery rate, span-wise expansion, near wake velocity deficit and the wake deflection [79].

The cross-section of a wake is generally approximated to be circular, so the reality of a non-symmetric or skewed wake shape produces different results in terms of energy yield or loading conditions on downstream turbines compared with the predicted behaviour. The diagonal skewing associated with wakes produced from veered wind flow may result in the regions of high and low velocity gradients occurring at different lateral locations relative to the turbine tower [35]. If a downstream turbine is laterally offset in the same direction as the higher velocity gradient partial wake region, it will likely experience higher load conditions and increased fatigue loading [35].

The power produced by a downstream turbine also differs when exposed to a skewed wake compared with a non-skewed wake [34]. Nouri *et al.* [32] tested the effect of the Coriolis force on steered turbines and observed the difference in power production associated with positive and negative yaw misalignment to decrease from 17% to 7% when the Coriolis force was relaxed. As mentioned earlier, a difference in power production when wake steering in implemented with positive and negative yaw angles has been noted in various studies. Similar to Nouri *et al.* [32], Archer and Van-Be-Hagh [55] and Bromm *et al.* [35] suggest the asymmetry in power production is influenced by wind veer and its effect on wake deflection. The rotation direction of the turbine blades is also theorised to contribute to power difference between yaw angles of opposite polarity [56], while Bartl *et al.* [53] highlight that the power asymmetry is higher when the flows have a lower

turbulence intensity.

Abkar *et al.* [80] derived an analytical wake model (Abkar model) that encapsulates the effect of wind veer on the downstream velocity profile. Their approach considers the conservation of mass and momentum in the flow, a skewed Gaussian velocity deficit distribution and builds on the Gaussian model proposed by Bastankhah and Porté-Agel [39][80]. The model agreed well with the maximum velocity deficit and normalised velocity deficit profiles obtained via LES of a turbine operating in SBL conditions and unlike previous parametric models, only the wake growth rate is required as an input, which can be approximated using values from previous studies.

However, the model assumes equal expansion of the wake in the vertical and spanwise direction, though Abkar and Porté-Agel note that under each of the different atmospheric stability regimes the vertical wake growth is smaller than the lateral [27]. The level of turbulence in the inflow wind is also not included in the calculation of velocity deficit in this model. Wake recovery rate is associated with the degree of turbulence in the freestream flow, with higher turbulence corresponding to faster wake recovery [23][39], and so the model would not accurately capture how velocity deficit changes for different inflow conditions.

Notably, the proposed model also does not consider the effect of yawing in the wake deficit model. Rotor yawing can counteract or compound with the inflow veer when it comes to wake deflection, and this must be accounted for when determining the location of the wake centre downstream of yawed turbines. Yawing also contributes to curling the wake shape, leading to a cross-sectional area that differs from that of a skew Gaussian and so the Abkar model would likely not accurately capture the effect of wind veer on yawed turbine wakes, with the authors suggesting further research is needed to account for yawing with this model.

The influence of wind veer on wake behaviour is expected to have a significant impact on the application of wake steering, as the technique requires an accurate estimation of the wake centre location to effectively redirect wakes away from turbines downstream and ensure that overall farm power is improved. As wind turbines increase in the size, they cover greater regions of the ABL and with veer, the change in wind direction across the rotor will similarly become larger. Thus for wake steering to be effective in real, wind farm operating conditions, it must be capable of incorporating the variations in wake behaviour due to wind veer.

Englberger *et al.* [78] and Englberger and Lundquist [36] revealed how the inflow wind veer interacts with the superimposed vortex due to rotor rotation, with the spanwise velocity component, and thus wake deflection, being amplified or weakened depending

on the rotation direction. A similar incidence would thus be expected as veered inflow encounters a yawed turbine and the introduced lateral force the yawed rotor imparts on the flow, causing deflection. The direction of this lateral force would either combine with the inflow veer, enhancing the wake veer, or counteract it, minimising or reverting the direction of the wake veer. Accounting for this interaction between inflow veer and yawed turbine rotor is necessary for wake models to accurately predict wake deflection.

Similarly, the change in wake recovery rate for veered wakes may negate the need for extensive wake deflection should the velocity deficit recover in sufficient distance between turbine rows. This would affect the optimal yaw angle needed for effective wake steering as over yawing the upstream turbine would result in unnecessary power loss. This has been a common thread throughout many studies on the effect of wind veer on wind turbine wakes is the recommendation for low order wake models to capture the variation in flow dynamics [37][33]. Improving the accuracy of wake models would, in turn, improve the accuracy of wake steering methods given the controllers generally utilise empirical or analytical models when optimising the yaw set-points [16][20][21][54].

2.4 Summary

Wake steering has the potential to increase the power production of large wind farms by improving flow conditions between turbines. Wake losses are greatest when the atmospheric conditions are stable and the energy wakes persist for longer distances, generally passing through turbines downstream. A common feature of stable atmospheric conditions is the presence of wind veer, which has been shown to influence the shape of turbine wakes and how wakes deflect. Wake steering controllers utilise simplified wake models to determine the optimal yawing conditions to improve farm power production. However, if these models do not accurately capture the effect of wind veer on the wake behaviour and its deflection, then wake steering is unlikely to be an effective technique to improve wind farm efficiency in veered flow. Therefore, analysing how wake behaviour varies under different veering conditions and determining how accurately wake models currently used in wake steering controller development perform for veered inflow conditions is necessary to ensure wake steering can be beneficial in realistic, stable atmospheric wind flow.

3. Methodology

3.1 Simulator for Wind Farm Applications

The Simulator fOr Wind Farm Applications (SOWFA) is a computational fluid dynamics (CFD) solver based on the OpenFOAM framework that was designed by the National Renewable Energy Laboratory (NREL) specifically for simulating wind farms in atmospheric flow. It is a large eddy simulation (LES) solver, thus SOWFA resolves the turbulent structures larger than the discretised grid spacing and parameterises the effect of the dissipative turbulence at the sub-grid scale (SGS) using a closure model [81].

The Navier-Stokes (NS) equations describe the mechanics of fluid flow in terms of mass and momentum conservation. These equations are complex and analytical solutions are only available for simple cases. CFD solvers discretise the Navier-Stokes equations and treat the fluid volume as a mesh of cells, calculating the fluid parameters at each discrete point throughout the flow domain. SOWFA solves the incompressible, spatially filtered NS mass conservation and momentum equations as given below,

$$\frac{\partial \overline{u}_j}{\partial x_j} = 0 \tag{3.1}$$

$$\frac{\partial \overline{u}_i}{\partial t} + \frac{\partial}{\partial x_j}\overline{u}_j\overline{u}_i = -2\epsilon_{i3k}\Omega_3\overline{u}_k - \frac{\partial \tilde{p}}{\partial x_i} - \frac{1}{\rho_0}\frac{\partial}{\partial x_i}\overline{p}_0(x,y) - \frac{\partial}{\partial x_j}\tau_{ij}^D - g\left(\frac{\overline{\theta}-\theta_0}{\theta_0}\right)\delta_{i3} + \frac{1}{\rho_0}f_i^T \tag{3.2}$$

Each of the terms in Equations 3.1 and 3.2 represent a different aspect of flow behaviour and the overbar indicates terms that are spatially filtered. For example, $\overline{u}_j = u_j - u_j'$ is the velocity vector resolved by the grid and consists of the velocity fluctuation vector, u_j', subtracted from the instantaneous velocity vector, u_j.

Term I is the rate of change of the velocity components, describing how the velocity changes with time. Term II is the convection term, describing the transport of fluid throughout in space due to its velocity. Term III is the Coriolis force acting on the fluid due to the planetary rotation of the Earth.

The gradient of the modified pressure, $\hat{p}$, is given by Term IV. The modified pressure is given by, $\hat{p} = \tilde{p}'/\rho_0 + \tau_{kk}/3$, where $\tilde{p}'(x,y,z,t) = \tilde{p}(x,y,z,t) - p_0(x,y) + \rho_0 gz$. $\tilde{p}$ is the static pressure resolved by the mesh, p_0 is the averaged static pressure at the surface and $\rho_0 gz$ is the hydrostatic variation in pressure due to height. p_0 demonstrates linear variation in the horizontal directions due to the background driving pressure gradient. ρ_0 is the

constant density for the incompressible flow, the gravitational constant, g, is taken as 9.81 m/s^2 and z is the height above the ground surface. Thus, $\tilde{p}'$, is the deviation in the mesh resolved static pressure from the time-averaged static pressure. The modified pressure, $\hat{p}$, as outlined above, is normalised by density, and lumped with the trace component of the stress tensor, τ_{kk}.

Term V gives the gradient of the horizontally averaged, background driving pressure. The divergence of the deviatoric component of the stress tensor is given by Term VI, where $\tau_{ij}^D = \tau_{ij} - \tau_{kk}{}^{\delta_{ij}}/_3$. The stress contains both viscous and SGS parts, and δ_{ij} is the Kronecker delta. Term VII represents the effect of buoyancy using the Boussinesq approximation. Term VIII models any additional forces, normalised by constant density, acting on the flow. For the simulations involving a turbine, the force of the blades on the wind is incorporated in the momentum equation via Term VIII.

Generally, there is also a viscous term included in the momentum equations however it is not considered in the SOWFA solver as atmospheric flows occur at a high Reynolds number and viscous effects are only significant near solid surfaces. The effect of the turbine on the flow is modelled as a body force and the blade geometry is not resolved as a solid object, so the bottom boundary, which represents the ground, is the only surface in the domain. At the mesh cell centres, vertically closest to the ground boundary, the stress and temperature flux are modelled using Schumann's wall model to account for both the SGS and viscosity effects [82].

The above terms and models are discussed in more detail below.

3.1.1 Turbulence Closure Model

A turbulence closure model is required to model the SGS turbulence effects as SOWFA is an LES solver. The Smagorinsky model is an eddy-viscosity model which approximates the SGS stress via the linear relationship,

$$\tau_{ij}^D = -2\nu^{SFS}\overline{S}_{ij}, \tag{3.3}$$

where ν_{SGS} is the SGS viscosity and the strain rate tensor is given by,

$$\overline{S}_{ij} = \frac{1}{2}\left(\frac{\partial \overline{u}_i}{\partial x_j} + \frac{\partial \overline{u}_j}{\partial x_i}\right). \tag{3.4}$$

In SOWFA, Moeng's model is implemented for the SGS effects, which is a modified version of the Smagorinsky model [83]. In this model, the turbulent viscosity and turbulent

kinetic energy are calculated using,

$$\begin{aligned} \nu_{SGS} &= C_k \sqrt{k} \Delta \\ k &= 2 \frac{C_k}{C_e} \Delta^2 \| S_{ij} \|^2 \\ \Delta &= (\Delta x \Delta y \Delta z)^{(1/3)} \end{aligned} \tag{3.5}$$

where Δ represents the sub-grid length scale, k is the SGS turbulent kinetic energy, and C_k and C_e are model constants which relate to the Smagorinsky coefficient, C_s, via $C_s^2 = C_k \sqrt{\frac{C_k}{C_e}}$.

A Smagorinsky coefficient of 0.134, as given by $C_k = 0.0673$ and $C_e = 0.93$, is used in this implementation of SOWFA.

In this approach, the length scale is calculated as either based on the grid spacing or the stability dependent mixing length, whichever is smaller,

$$\begin{aligned} l &= min(\Delta, l_s) \\ l_s &= \begin{cases} 0.76\sqrt{k} \sqrt{\dfrac{\theta_0}{\left| g \dfrac{\partial \bar{\theta}}{\partial z} \right|}} & for \ \dfrac{\partial \bar{\theta}}{\partial z} > 0 \\ \Delta \quad for \ \dfrac{\partial \bar{\theta}}{\partial z} < 0 \end{cases} \end{aligned} \tag{3.6}$$

where θ_0 is a constant reference potential temperature and $\frac{\partial \bar{\theta}}{\partial z}$ is a measure of stability, which is positive for the SBL due to its positive temperature gradient.

This length scale modification was suggested by Deardorff to address the small mixing lengths observed in SBL flow due to the relatively smaller turbulence intensity in stable conditions compared with other BL flows [83]. The turbulent Prandtl number is also sensitised to the local stability, calculated using both the grid- and stability-dependent length scales,

$$Pr_t = \frac{1}{1 + \frac{2l}{\Delta}}. \tag{3.7}$$

Thus in regions where the vertical gradient of the potential temperature is positive, such as in the capping inversion, the turbulent Prandtl number would be closer to 1 and SGS temperature diffusivity is reduced as SGS thermal conductivity depends on the SGS viscosity and turbulent Prandtl number via $\kappa = \frac{\nu_{SGS}}{Pr_t}$.

Variations in features of the simulated boundary layer, such as its depth, have been associated with the selected SGS model and model constants. For the Smagorinsky

coefficient, a value of 0.23 was observed to result in a reduction in resolved turbulence compared with smaller coefficient values [84]. Bhaganagar and Debnath [76] tested the simulation sensitivity for a range of Smagorinsky coefficient values and determined that $C_s = 0.1$ to 0.132 compared well with results from the GABLs study [84], as well as Kosovic and Curry [85] and Nieuwstadt [86].

The flow field is initially uniform and velocity perturbations at the ground surface are superimposed to generate turbulence within the flow. These fluctuations occur with the spanwise and streamwise velocity components. The SGS quantities are initially set to zero and gradually establish within the flow over time.

3.1.2 Coriolis Forcing

The effect of the Coriolis forcing, and thus wind veer, is included in SOWFA via a body force term in the NS momentum equations. The magnitude of the force is proportional to the latitude location of the wind farm and varies with height, as per,

$$f_c = -2\epsilon_{i3k}\Omega_3\overline{u}_k \tag{3.8}$$

with

$$\Omega_j = \omega \begin{bmatrix} 0 \\ \cos\phi \\ \sin\phi \end{bmatrix} \tag{3.9}$$

where Ω_j is the vector for the rate of planetary rotation at a location on the Earth's surface, ω is the planetary rotation rate and ϕ is the angle of latitude of the wind turbine site. The rate of rotation was set to 7.27×10^{-5} rad/s (1 revolution per 24 hr) and different values for the latitude were implemented to modify and isolate the effect of wind veer on the wake behaviour.

3.1.3 Boussinesq Approximation

SOWFA uses an incompressible form of the NS equations with density treated as a constant value, however in real atmospheric flows the density will vary due to heating and cooling fluxes from the Earth's surface and changes in altitude. Rather than solving the compressible NS equations, which requires significantly more computational resources, the buoyancy effects are included via the Boussinesq approximation.

The Boussinesq approximation assumes variations in density to be most significant in the buoyancy term of the NS equations and negligible in the other terms. Thus, constant density, ρ_0, is included in the other filtered NS equation terms and only the buoyancy

force is re-written as,

$$F_B = \rho g = (\rho_g + \Delta\rho)g \tag{3.10}$$

where $\Delta\rho$ is the variation in the density relative to the constant density value. This can be re-written further in terms of the thermal expansion of air,

$$\Delta\rho g = (\rho - \rho_0)g = -\rho_0\beta(T - T_0)g \tag{3.11}$$

where β is the thermal expansion coefficient and, under the ideal gas assumption, $\beta = \frac{1}{T_0}$. Putting this in terms of potential temperature, the force due to buoyancy is represented as,

$$F_B = g\left(\frac{\overline{\theta} - \theta_0}{\theta_0}\right)\delta_{i3} \tag{3.12}$$

An equation for transport of potential temperature within the flow is thus required to update the potential temperature for the Boussinesq equation. This is given by,

$$\frac{\partial\overline{\theta}}{\partial t} + \frac{\partial(\overline{u}_j\theta)}{\partial t} = -\frac{\partial q_j}{\partial x_j}. \tag{3.13}$$

$\bar{\theta}$ is the resolved potential temperature and q_j is the temperature flux due to viscous and SGS effects.

3.1.4 Wall Model

LES methods resolve the larger turbulent eddy structures, but near the wall, these energy-containing scales become smaller and smaller and would require a much higher resolution grid to capture the turbulent effects [87].

The stress and temperature flux near the ground boundary are modelled as SGS effects throughout the domain, except within the region near the lower boundary. In this region, the Schumann wall model is applied to account for both the SGS and viscous effects [82]. At the ground boundary, the stress tensor components are equal to zero except for the vertical shear stresses, τ_{13} and τ_{23}, which are specified as,

$$\begin{aligned}
\tau_{13}^{tot} &= -u_*^2\frac{\overline{u}_{z_1} - \langle\overline{u}_{z_1}\rangle}{(\langle\overline{u}_{z_1}\rangle^2 + \langle\overline{v}_{z_1}\rangle^2)^{\frac{1}{2}}} \\
\tau_{23}^{tot} &= -u_*^2\frac{\overline{v}_{z_1} - \langle\overline{v}_{z_1}\rangle}{(\langle\overline{u}_{z_1}\rangle^2 + \langle\overline{v}_{z_1}\rangle^2)^{\frac{1}{2}}}.
\end{aligned} \tag{3.14}$$

Here u_* is the friction velocity, z_1 refers to the cell centre closest to the ground boundary and angle brackets indicate horizontal averaging. The Monin-Obukhov similarity theory (MOST) is applied along the bottom, ground boundary to relate the velocity at the first

cell centre in the vertical direction to the instantaneous wall stress and calculate the friction velocity as needed by the wall model [88]. MOST can only be applied when the friction velocity is non-zero and the wind is not calm [25].

The aerodynamic roughness height, z_0, and the horizontally averaged surface temperature flux are specified by the user as constants in the SOWFA code. The friction velocity is a function of the vertical shear stresses,

$$u_*^2 = (\langle \tau_{13}^{tot} \rangle^2 + \langle \tau_{23}^{tot} \rangle^2)^{\frac{1}{2}} \tag{3.15}$$

and thus, must be calculated iteratively. This is achieved by driving the following equation to zero,

$$f(u_*) = u_* - \frac{\kappa(\langle \overline{u}_{z1} \rangle^2 + \langle \overline{v}_{z1} \rangle^2)^{\frac{1}{2}}}{\ln\left(\frac{z_1}{z_0}\right) - \varphi_M} \tag{3.16}$$

where $\varphi_M = -\gamma_M \frac{z_1}{L}$, with L, the Obukhov length calculated as,

$$L = -\frac{u_*^3}{\kappa q_w \left(\frac{g}{\theta_0}\right)}. \tag{3.17}$$

The surface heat flux is calculated as follows,

$$q_w = \frac{\kappa u_* \Delta T}{\ln\left(\frac{z_1}{z_0}\right) - \varphi_H} \tag{3.18}$$

where κ is the von-Karman constant, ΔT is the temperature difference between the ground surface and cell centre, $\varphi_H = \gamma_H \frac{z_1}{L}$, and γ_M and γ_H are stability parameters. The values used for γ_M and γ_H are 4.9 and 7.8 respectively as per Beare *et al.* [84]. This surface heat flux accounts for the variation between the temperature at the surface boundary and at the temperature at the cell centre adjacent to the lower boundary.

3.1.5 Discretisation and Momentum Equation Solver

The terms of the NS equations are discretised using a finite volume, collocated approach that is equivalent to second order accuracy in space. Quantities at the cell centres are linearly interpolated to the cell faces to obtain the derivative values at the cell centres. However, SGS quantities are calculated at the cell faces as the SOWFA developers found calculating SGS values at the centre and then interpolating to the faces resulted in excessive friction near the surface. Directly calculating SGS terms at the faces has been shown to address this issue [89].

The spatially filtered momentum equations are solved using the predictor-corrector Pressure-Implicit Splitting Operation (PISO) method [90]. The predictor step solves for momentum using the previous time-step pressure field. This is followed by three corrector steps to iteratively update the pressure and velocity fields per the filtered continuity equation. After the correction steps, the temperature, SGS effects and turbine body forces are calculated sequentially, based on the values from the previous time step.

The linearised momentum predictor and potential temperature equations are calculated iteratively via the diagonal incomplete-LU preconditioned bi-conjugate gradient method. The pressure term is solved using a geometric-algebraic multigrid (GAMG) iterative solver. Quantities at the cell centres are linearly interpolated to the cell faces to obtain the derivative at the centre of the cells. Rhie-Chow interpolation for the velocity fluxes is implemented to prevent the decoupling of the velocity and pressure terms and avoid checker-board oscillations [91].

Time discretisation is achieved using a second order accurate, backward in time method. The effect of the turbine on the wind flow is modelled as a body force using the Actuator Line Method (ALM), discussed in more detail in Section 3.3.2.

The SOWFA implementation involves first running a precursor ABL simulation without any turbines to generate the atmospheric flow and turbulent structures [89]. Once the flow has developed and reached a quasi-equilibrium state, it is run for some time longer with sampling at each time step at the upstream boundary plane. These planes of turbulent flow data are then used as the inflow conditions to initialise the turbine simulation. Figure 3.1 presents a schematic of this process. These three steps will henceforth be referred to as the 'spin-up', 'precursor' and 'turbine' simulations.

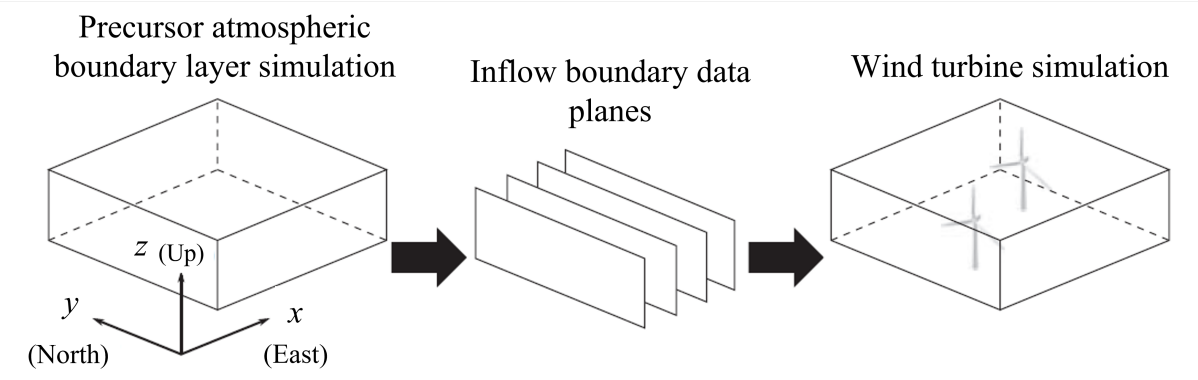

Figure 3.1: SOWFA process obtained from [26].

SOWFA has been used extensively in the study of wind farms in atmospheric flow conditions and has been validated as an effective CFD tool in numerous studies. For neutral and unstable conditions, SOWFA has demonstrated its proficiency to represent

these flows and their structures. The solver was able to replicate the logarithmic law of the wall scaling for neutral flow profiles. While the development of updrafts, significant vertical velocity fluctuations distinct to unstable atmospheric flows due to pockets of warmer air rising, were observed in SOWFA simulations of unstable flow conditions [89]. Churchfield et al. compared simulations and field data for the 48-turbine Lillgrund wind plant and found good agreement between the power production data for the first five rows of the farm [89]. SOWFA can reproduce the turbulent structures in a NBL over water, as demonstrated by a comparative analysis on the wind spectra and coherence between the simulated results and empirical spectral models by Kaimal and Busch-Panofsky [92].

However, the structure of the SBL varies from the NBL and CBL and so simulating stable conditions has different requirements. As the SBL is characterised by low turbulence intensity, the characteristic eddies are generally quite small. This is a point of difficulty when using LES to capture the SBL as a higher resolution grid or greater dependence on the SGS model is needed for a reliable simulation and maintaining the resolved turbulence. Without proper grid resolution or with an overly dissipative turbulence model, the SGS fluxes dominate and the resolved turbulence can vanish [84]. This has been found to result in the flow falsely appearing to be laminar and runaway cooling at the ground surface [70].

Although the initial implementation of SOWFA was not suitable for SBL flow, Churchfield et al. introduced an updated version with improved SGS model capabilities and demonstrated its validity [87]. This was achieved by comparing SOWFA results with the Global Energy and Water Cycle Experiment Atmospheric Boundary Layer Study (GABLS) LES model inter-comparison results for SBL flows obtained by Beare et al. [84]. The ability of the solver to produce similar mean profiles for wind speed, potential temperature and various flux profiles when the Smagorinsky model with coefficients ranging from 0.135 to 0.17 were used was presented [87]. The Lagrangrian-averaged scale-independent (LASI) dynamic model was similarly tested and performed more poorly relative to the Smagorinsky model when both were compared with the GABLS cases, over-predicting the height of the LLJ and wind direction angle [87].

This comparison was repeated by Ghaisas et al. [50], along with simulations of a turbine operating in the SBL corresponding to the study by Lu and Porté-Agel [93]. The Smagorinsky model with a coefficient of 0.13 and the LASI dynamic model were both implemented again. The authors noted good agreement with the GABLS and Lu and Porté-Agel results in terms of mean temperature, TKE, momentum fluxes and buoyancy fluxes of the SBL, with both SGS models showing similar results. The mean streamwise and spanwise velocity profiles showed great agreement with the profiles from Lu and Porté-Agel and were within the spread of results obtained in the GABLS study. For simulations including a turbine, good agreement with Lu and Porté-Agel was again observed for the

time-averaged profiles of the mean velocities, temperature, momentum fluxes and buoyancy fluxes. Reasonable agreement for the TKE profiles at various downstream distances from the turbine was also obtained, with the Smagorinsky model giving results closer to the reference LES [50]. This repeated study by Ghaisas *et al.* [50] demonstrated the capacity of SOWFA to replicate the results of stable atmospheric flows and turbines operating in the SBL.

Bhanagar and Depnath also achieved similar results to the GABLS study for turbulence intensity profile, mean temperature profile and mean streamwise velocity profile when using SOWFA to simulate the SBL with a grid size of 3.125 m and C_s of 0.1 to 0.132, as well as a grid of 6.25 m and $C_s = 0.1$ [76]. The authors have since used SOWFA in several studies on wind turbines operating in the SBL [76][94].

3.2 Stable Boundary Layer Flow

The spin-up simulation is first run to establish the stable atmospheric flow features. This required setting the parameters for the SBL, establishing the most suitable discretised grid and run time.

3.2.1 SBL Parameters

As outlined in the literature review, the SBL is characterised by low turbulence, negative buoyancy and a positive potential temperature vertical profile. A cooling rate of -0.25 K/h was imposed along the ground boundary, which corresponds to a 'low stable regime' [94]. The more stable the flow, the smaller the turbulent eddy structures and thus the higher resolution grid required to appropriately capture the flow behaviour. Therefore, a lower stability case is simulated rather than a highly stable boundary layer as it is more feasible and less computationally intensive [70]. Implementing a surface cooling rate, rather than a surface heat flux, as a boundary condition is recommended for simulating the SBL [95].

A surface roughness value of 0.001 m is employed to replicate the conditions of an offshore wind farm [19]. This was chosen as SBL conditions often develop offshore due to the heat transfer between the cool water surface and the warmer air above. Similarly, wake losses for offshore farms tend to be significant and wake steering would thus be highly effective in offshore farms. The temperature is initialised to 300 K and a temperature inversion is implemented starting at a height of 500 m with a width of 100 m, above which the potential temperature increases at a rate of 0.003 K/m. The pressure throughout the domain is fixed at a constant value and during the first solver step, it is adjusted to maintain continuity in the flow.

The horizontal directions are in the x- (east-west) and y-coordinate (north-south) directions with the z-axis following the vertical direction. The horizontally averaged wind velocity is set to 8 m/s at a height of 100 m and wind flows from west to east through the domain. SOWFA adjusts the driving pressure gradient based on the difference between the actual and input wind speed at hub height. After some time, the driving pressure gradient oscillates about a mean value, maintaining the desired hub height wind velocity.

3.2.2 Domain and Boundary Conditions

The domain for all simulation steps was 3000 m $\times$ 2000 m $\times$ 800 m. For the spin-up and precursor simulations, the horizontal boundaries are all periodic. The lower, ground boundary is an impenetrable surface with zero normal velocity. The upper boundary is above the boundary layer wind flow and acts as a rigid lid on the flow, with stress and temperature flux set to zero. Thus, there is no need to specify temperature and velocity boundary conditions at the upper or lower boundary given the stress and temperature flux conditions have been input.

For the turbine simulation, only the side boundaries are periodic, with the sampled precursor velocities and temperatures specified at the upstream boundary for each time-step. The downstream boundary has Neumann conditions with the velocity and temperature gradients set to zero. Similar to the preceding simulation steps, the top boundary in all simulations is treated as a stress-free lid on the flow.

3.2.3 Wind Veer Variation

To vary the wind veer profile, different latitude values were implemented as this varies the Coriolis force acting on the flow. These latitudes are outlined in Table 3.1.

Table 3.1: Wind veer cases

Case	Latitude (°)
Lat0	0
Lat10	10
Lat40	40
Lat70	70
Latneg10	-10
Latneg40	-40
Latneg70	-70

As the Coriolis force acts in different directions in the Northern and Southern Hemi-

spheres, both positive and negative latitudes are tested to observe how the wake responds to wind direction profiles acting in opposite directions. The 0° latitude case is to provide a reference for the effect of the varying Coriolis forces due to the different latitudes as the wind veer profile is near constant at 0° across the turbine rotor.

3.2.4 Grid Resolution

For the grid sizing, three different approaches were tested and compared to determine which is most suitable in resolving the flow structures and can be calculated within a reasonable time. Given the large domain, even on coarse grids, the time to compute several hours of simulated flow is significant and require the use of super-computing facilities. The simulations run in this research were performed using Artemis, the University of Sydney's high performance computing (HPC) facility, and Gadi, the National Computational Infrastructure (NCI) Australia's supercomputer.

The three grid sizes tested are outlined in Table 3.2 and will be referred to as the '12.5m', '6.25m' and 'graded' grids. The simulation parameters for these tests differed slightly from the specifications above the SBL. A latitude of 41.3° and a surface roughness of 0.15m was used. The 6.25m and graded grids address the additional resolution needed in the vertical direction for atmospheric flows given the variation in properties with height due to the stratified wind velocity profile and associated vertical wind shear.

Table 3.2: Details of the grids tested for the SBL simulation

Case	Cell dimensions	Total number of cells	Maximum cell length (m)	Minimum cell length (m)
12.5 m	240 × 160 × 64	2,457,600	12.5 m	12.5 m
6.25 m	240 × 160 × 128	4,915,200	12.5 m (horizontal)	6.25 m (vertical)
Graded	240 × 160 × 64	2,457,600	33.63 m (vertical)	2.80 m (vertical)

Comparing the vertical profile of the span-wise velocity component for each of the grids revealed the 12.5m to differ significantly from the other two grids in the heights covered by the turbine rotor, at various run times. Similarly, the momentum and buoyancy fluxes were expected to take a much longer run time to converge when using the 12.5m relative to the 6.25m and graded grids. While the computational time was much faster for the 12.5m grid, it was considered to be sub-optimal given it requires a longer run time, which may negate any benefit of computation speed, and the variations in the vertical velocity profiles.

The graded grid computed faster than the 6.25m as it involves fewer mesh cells. However, a caveat of the graded grid is that the additional refinement around the turbine

and wake region will also be graded and so the aspect ratio of the cells in this region would vary across the height of the turbine, as the horizontal grid lengths are uniformly refined. As discussed further in Section 3.3.2, the parameter used to project the blade body force onto the flow, ϵ, is dependent on the local grid size.

The 6.25m grid was thus chosen for the simulations given its uniformity when refined, as the graded grid may experience skewness in the flow values due to the varying, high magnitude mesh cell aspect ratios in the turbine region. Although this grid did involve the longest computational time, it is manageable, especially when using HPC facilities. The GABLs inter-comparison study also concluded that a grid spacing of 6.25 m produces reasonable accuracy relative to the higher resolution simulations [84]. Previous implementations of the SOWFA solver have only used uniform, rather than graded, grids and so this is continued here. Section 3.2.4.1 presents a summary of the results of the grid resolution tests.

3.2.4.1 Atmospheric Flow

Figure 3.2 presents the spanwise velocity profile with height for the three grids tested for implementation. The spanwise velocity profile was considered as varying the wind veer profile affects the spanwise velocities present across the rotor. As shown in the figure, the 6.25m and graded grids produced profiles that are very similar in the region across the turbine rotor, whereas the 12.5m grid was unable to resolve the same profile. Thus, the 12.5m grid was deemed insufficient for representing the SBL flow. As outlined in Section 3.2.4, the 6.25m grid was selected as graded grids have not been applied to SOWFA before and the skew of the grid introduces difficulties when defining the distribution function involved in the actuator line method.

The transient momentum and buoyancy fluctuations were also compared between the three different grid sizings and, as shown in Figure 3.4 and discussed above, the projected time for the 12.5m grid to converge is longer than that for the 6.25m and graded grid. This further influenced the selection from the latter grids and it would significantly increase the computational requirements of the atmospheric wind simulations.

3.2.5 Run Time

A variable time-step is used to maintain a maximum Courant number of 0.75 and is capped at a maximum of 25s. The Courant number reflects the ratio of the distance travelled by the wind flow in one time-step and the mesh cell length and should not exceed 1 for the numerical schemes used in SOWFA [96].

The spin-up simulations were run until a quasi-equilibrium state is achieved. This

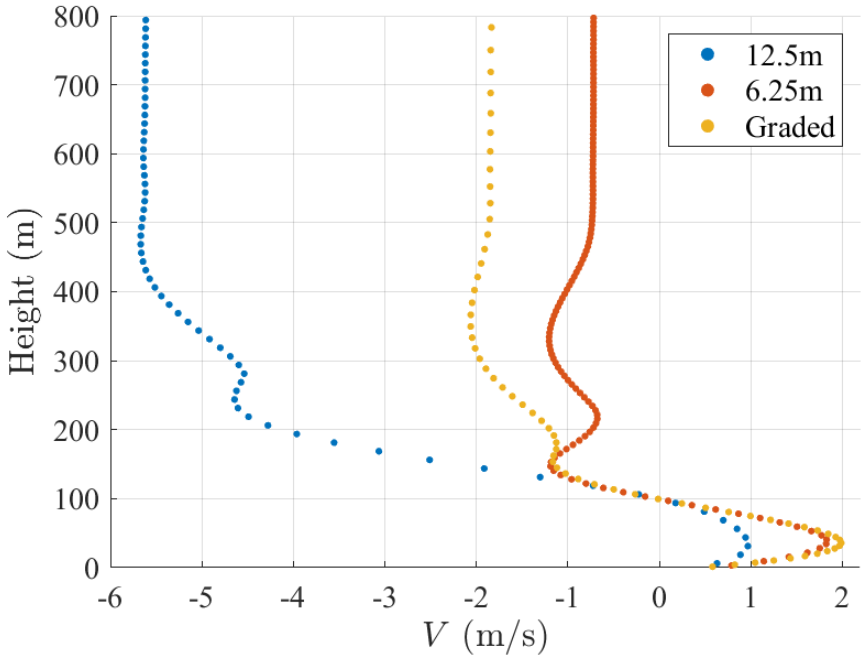

Figure 3.2: Horizontally averaged spanwise velocity with height for the 12.5m, 6.25m and graded grids

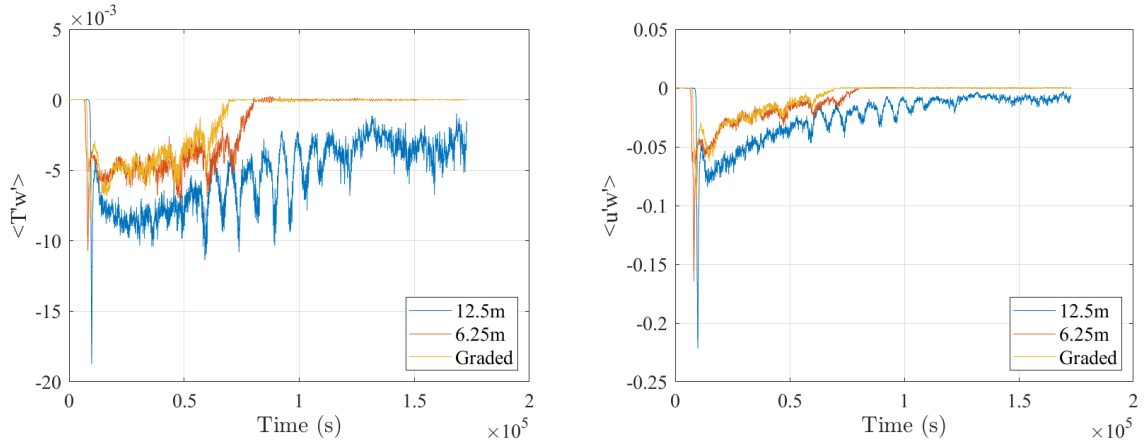

(a) $< T'w' >$ **(b)** $< u'w' >$

Figure 3.3: Horizontally averaged buoyancy and momentum for the tested grid sizes

is defined as the time taken for the vertical momentum and vertical buoyancy fluxes at heights across the wind turbine rotor to converge to constant values, similar to the approach by Bhaganagar and Depnath [76]. The run times differed across the different veering cases and are presented in Table 3.3, with figures depicting the flux convergences included in Appendix A.2. The Artemis queue for running these simulations involved 24 cores per node, while the Gadi queue involved 28 cores per node, and so the CPUs utilised for the simulations differs between the two supercomputers.

Table 3.3: Run times and computational resource per veer case

Case	Run time (s)	Run time (h)	Cores (CPUs)	Total resource (kSUs)
Lat0	248,400	69	96	6.624
Lat10	118,800	33	112	3.696
Lat40	223,200	62	112	6.944
Lat70	86,400	24	96	2.304
Latneg10	129,600	36	96	3.456
Latneg40	237,600	66	96	6.336
Latneg70	86,400	24	96	2.304

The different veering cases each vary in the magnitude of Coriolis force and thus the balance of forces also differs between the cases and therefore, the run times vary between the cases.

The SBL is characterised by negative buoyancy and this dampens the turbulent eddies, leading to low turbulence and highly stratified flow, thus the fluxes associated with buoyancy were also measured in determining the time allowed for the flow to develop. Wake recovery is driven by the entrainment of momentum from the surrounding freestream flow into the wake region and so the transient nature of the vertical momentum was similarly considered in determining the wind-up run time.

Once the quasi-equilibrium state has been reached, the velocity and temperature values are sampled every time step at the west, inflow boundary plane in the precursor simulation step. This data is collected for 3600s for use as the turbine simulation inflow conditions.

3.3 Turbine Modelling

3.3.1 Turbine Parameters

The turbine modelled in these simulations is the NREL 5MW turbine, the details of which are outlined in Table 3.4. This is the default turbine available in SOWFA and was chosen for these simulations as there is easily available data on the turbine parameters, as needed for modelling the turbine. The turbine yawing cases are for 0°, 20° and −20°. Wake steering controllers tend not to exceed yaws of ±20° to manage the increase in structural loading experienced by the yawing turbine [97].

Table 3.4: Parameters of the NREL 5MW Turbine [98]

Parameter	Value
Hub height	90 m
Rotor diameter	126 m
Number of blades	3
Rotation speed	9.1552 rpm
Rotation direction	Clockwise
Cut-in speed	3 m/s
Rated speed	11.4 m/s
Cut-out speed	25 m/s

3.3.2 Actuator Line Method

The ALM discretises wind turbine blades into actuator points along lines, with each line representing one blade, and returns the forces of the blades acting on the flow field [99]. This force is included in the NS equations as Term VIII in Equation 3.2. Each actuator point is described by its radius from the turbine hub and is assigned the actual blade properties from the turbine type being modelled at that radius. These properties include the type of airfoil, the chord length and twist angle, which are provided by a table of the values for each radial distance. The velocity vector, consisting of the components from both the wind flow and rotational velocity due to the blade motion, is sampled at the centre of each actuator point. This is used to determine the flow angle and magnitude of resultant velocity at each point. The angle of attack is then found by subtracting the blade twist and pitch from the flow angle. Given the angle of attack and magnitude of velocity, the force per spanwise unit length is calculated at each actuator point, as below,

$$f_{2D} = \frac{1}{2}\rho U_{rel}^2 c \left(C_L \mathbf{e}_L + C_D \mathbf{e}_D\right), \tag{3.19}$$

where U_{rel} is the local velocity relative to the blade, c is the chord length at the actuator point, $C_L(\alpha, Re)$ and $C_D(\alpha, Re)$ are the lift and drag coefficients, respectively, and $\mathbf{e}_L$ and $\mathbf{e}_D$ are the unit vectors in the direction of the lift and drag forces, respectively. The outcome of this process is a number of point forces acting along each actuator line but are not linked to the cells of the discretised grid. These point forces must be converted to volume forces within the grid cells to be solved numerically in the momentum equations. This is achieved by projecting the point force onto the nearby cell volumes per the following approach developed by Sørensen and Shen [99]. The force vector at the actuator point j, located at (x_j, y_j, z_j) for time t is $f_i^A(x_j, y_j, z_j, t)$ and the resulting body force vector at

the cell (x, y, z) and time t due to actuator point forces is,

$$F_i^A(x, y, z, t) = \sum_{j=1}^{N} f_i^A(x_j, y_j, z_j, t) \frac{1}{\epsilon^3 \pi^{3/2}} \exp\left[- \left(\frac{|\overrightarrow{d_j}|}{\epsilon} \right) \right]^2 . \tag{3.20}$$

Where ϵ is the projection width, d_j is the distance vector between the cell centre location (x, y, z) and the actuator point j at (x_j, y_j, z_j).

Troldborg indicate epsilon should be at least twice the grid spacing to reduce "spurious flow field oscillations to acceptable levels by adequately resolving the projection function" [100]. For the grid resolution used in the simulations, this corresponds to 6.25 m and 3.125 m in the horizontal and vertical directions, respectively. Churchfield *et al.* suggest for the correct power prediction of large utility-scale rotors with large aspect ratios, epsilon should be approximately $0.035D$, which equals 4.41 m for the turbine diameter of 126 m [101]. Churchfield *et al.* put forth that the projection width should relate to the blade chord length given the lift and drag forces are calculated using the chord length. The maximum blade chord length of the NREL 5-MW turbine is about 4.7 m [98]. A constant value of 5 was thus chosen as it is more than double the vertical grid spacing and is close to the maximum cord length. 40 actuator points are implemented along each actuator line and so the spacing between points is less than the grid spacing, as suggested by Troldborg *et al.* [96][100].

As the solid blade structures are not resolved, neither is the boundary layer flow over the blade surfaces. However, larger structures such as the vortices shed from the turbine hub and blade tips, the flow induction region upstream of the turbine and the wake, with its rotation, deflection and recovery, are captured. The Actuator Disk Method (ADM) uses a similar approach, but rather represents the turbine rotor as a porous disk, with the blade forces calculated over discretised disk sections instead of along the blade lines [13][102]. The ALM, however, is used to represent the turbine here rather than the ADM as it resolves more details of the wake, in particular, it can depict the vortex structures within the flow. The wake of a yawed turbine distinctly involves a pair of counter-rotating vortices (CVP) shed from the top and bottom of the rotor and these contribute to skewed cross section. This behaviour is not captured by the ADM and so the higher fidelity ALM is chosen.

3.3.3 Additional Mesh Refinement and Boundary Conditions

The mesh is refined in the region of the turbine and wake to increase the resolution of the wake flow structures. The domain refinement works by halving the mesh cell in each direction, and so one three-dimensional cell becomes 8 cells when refined. As a result,

the grid resolution is refined to 3.125 m in the horizontal directions and 1.5626 m in the vertical direction. The regions in the domain with additional refinement are depicted in Figure 3.4. One level of refinement resulted in discontinuities in the flow, with SGS errors

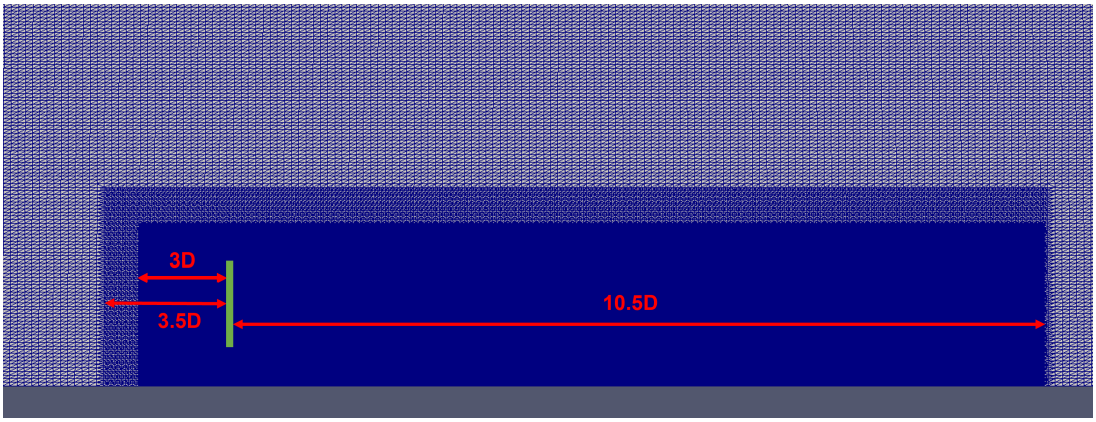

(a) View from upstream (yz plane)

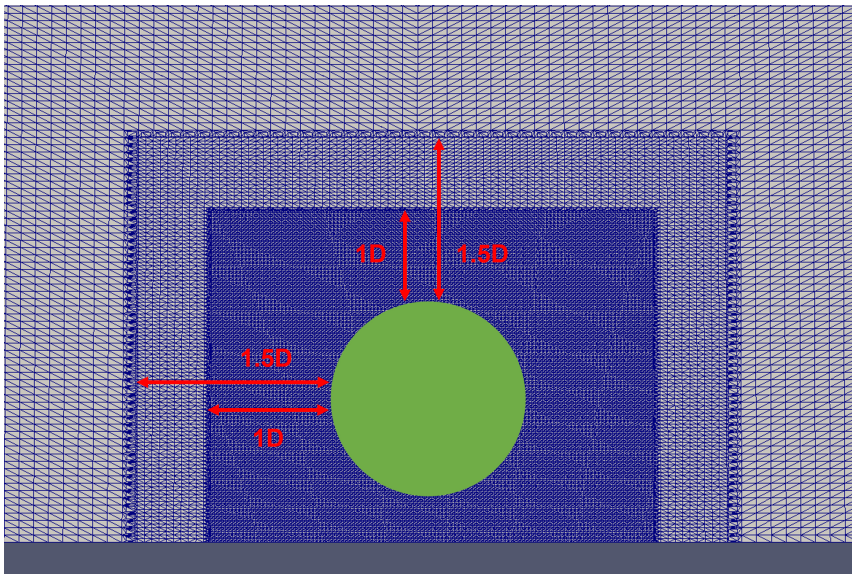

(b) View from the side (xy plane)

Figure 3.4: Mesh refinement region around the turbine, shown in green.

appearing to propagate upstream from the turbine. This was observed by viewing the eddy viscosity and corresponding SGS turbulent kinetic energy throughout the domain, as depicted and discussed further in Appendix A.1.2. Whereas two levels of refinement did not demonstrate these 'wiggles'. Three refinement levels would provide even higher resolution, but would also require significantly more computational resources and the run times would not be feasible.

The location and size of the two refined regions were implemented on a balance of run time and ensuring sufficient spacing around the turbine so the wake behaviour is not sensitive to the changes in refinement. Velocity deficits at more than $10D$ downstream of the turbine have been observed to be insignificant, with the wake flow generally having

recovered back to the inflow conditions again and so the refined region for the wake only extends to $10.5D$ from the turbine [41].

The turbine simulation was run for 3600s, with time averaging occurring over the last 1800s and results written out at 300s intervals. A fixed time-step of 0.025s was implemented to limit the turbine blade tip from advancing more than one grid cell within one time-step. With a rotor speed of 9.1552 rpm, this corresponds to approximately 260 time-steps per revolution of each blade.

3.4 Wake Centre Location

Understanding the location of the wake centre is necessary for effective wake steering controllers. The location of the wake centre is determined using the available power method [28][103]. This involves calculating the power available in the waked flow for a theoretical turbine located at increasing downstream distances. The downstream power is then compared with the available power in the freestream conditions for the same lateral offset, but upstream of the turbine in uninterrupted flow. The equation for the wake centre is thus,

$$\begin{aligned} f_{AP}(x_D, y_D) &= \iint_G \frac{U(x_D, y, z)^3}{U_{free}(-1.5D, y, z)^3} dydz, \\ G &: (y - y_T)^2 + (z - z_h)^2 \leq R^2, \end{aligned} \tag{3.21}$$

where the subscript D denotes the coordinate at the downstream distance, U_{in} is the streamwise wind velocity at $-1.5D$ upstream of the simulated turbine, y_T is the lateral position of the theoretical turbine, z_h is hub height of the theoretical turbine and R is the radius of the turbine. This was integrated discretely over the available data and 200 offset positions were tested. The lateral offset that produces the minimum value for power is considered the wake centre. Equation 3.21 is derived from the turbine power, given in Equation 2.1, with the air density, rotor area and turbine power coefficient assumed to be the same for the upstream and downstream theoretical turbines.

The integration was performed discretely, over the available data with the lateral bounds of the offset positions limited by the mesh refinement areas of the turbine simulation. The inner most refined grid area spans from -190m ($-1.5D$) to 190m ($+1.5D$) relative to the turbine at 0 m. The boundaries for the wake centre location integration were thus ± 107 m relative to the turbine to ensure the theoretical downstream turbine rotor was entirely within the inner most refined region. The number of lateral offset positions tested was chosen based on the wake centre location and minimum power available in the flow had converged by 200 points.

While this method does not necessarily track the location of the maximum velocity

deficit in the wake, it does indicate how a downstream turbine is affected by the combination of wind veer and yawing. This information is much more relevant to wake steering controllers, which aim change turbine yaw angles to improve overall wind farm production [28]. It also captures how the veered and deflected wake interacts with the surrounding freestream conditions, particularly, the stratified velocity profile. Similarly, it does not assume a specific wake shape, unlike similar Gaussian fit approaches, [28][104] and so the skew of the wake cross-section and how that propagates downstream contributes to the overall wake centre location.

3.5 Wake Models

The results obtained from the SOWFA simulations were compared with various established wake models, currently used in the development of wake steering controllers to observe how accurately these models represent the wake behaviour in veered inflow conditions. Models for the velocity deficit and the wake deflection were tested separately. The models are briefly described below with the full outlines of the parametric relationships involved presented in Appendix A.3.

3.5.1 Velocity Deficit

The velocity deficit models compared with SOWFA in this study are the Abkar model [80] and the Gaussian Curl Hybrid (GCH) model [40]. The Abkar model aims to represent velocity deficit of a wake in veered flow [80]. While the GCH model is commonly implemented in controllers used in field tests as it captures the generation of vortices in the wake, including the counter-rotating vortex (CRV) pair that form at the top and bottom of a yawed rotor and contributes to the secondary steering effect [40].

3.5.2 Wake Deflection

The wake deflection models include the Jiménez model [13], the FLOw Redirect In Steady state (FLORIS) model [11] and the Gaussian model from Bastankhah and Porté-Agel (Gaussian model) [39]. The derivation of and underlying concepts for these models was discussed in Chapter 2.1.5.

4. Results and Analysis

This section presents the results from the SOWFA simulations, as well as a comparison between the high-fidelity simulation results and established wake models, currently used in wake steering studies. The results presented below include observations on the wind veer profiles, shape of the wake cross-section, trajectory of the wake, deflection of the wake centre and wake recovery. An analysis on the power production of a two turbine array in veered flow, with and without wake steering, is also presented, followed by an examination into the efficacy of commonly used wake models in representing the dynamics of yawed wakes in veered inflow. For brevity, hereinafter each of the wind veer cases and yawing cases will be referred to using the abbreviated labels. For example, when referring to the turbine yawed 20° in wind flow at a latitude of 40°, it will be described as the Lat40 Yaw20 case, while a $-20°$ yaw at $-10°$ latitude will be Latneg10 Yawneg20.

4.1 Wind Veer Profiles

Each latitude tested corresponds to a different Coriolis force and so the inflow wind veer profile varies between each latitude case. This corresponds to the angle of the horizontal wind vector, α, changing across the rotor area and can be found using,

$$\tan(\alpha) = \frac{V(x, y, z)}{U(x, y, z)} \tag{4.1}$$

where U and V are the streamwise and spanwise velocity components, respectively. The wind veer profile can then be defined as how this wind vector angle changes with height as shown in Figure 4.1. At a latitude of 0°, or on the equator, the wind veer profile is effectively 0° at all heights. Note that a positive (negative) wind vector angle refers to a vector pointing to the left (right) of a turbine when viewed from upstream. From Figure 4.1, it is shown that for positive latitudes, the wind angle is positive below the hub height of the turbine and negative above, with the opposite relationship occurring for negative latitudes.

The differences in the wind veer profile shape are most prominent in the upper region of the wind turbine rotor. For latitudes of ±40° and ±70°, the wind vector appears to change direction and turn back toward the opposite direction in this upper rotor region. For the ±40° latitudes, this presents as a plateauing of the wind vector angle and maintaining an approximately constant angle from 150 m and above. While for the ±70° latitudes, the

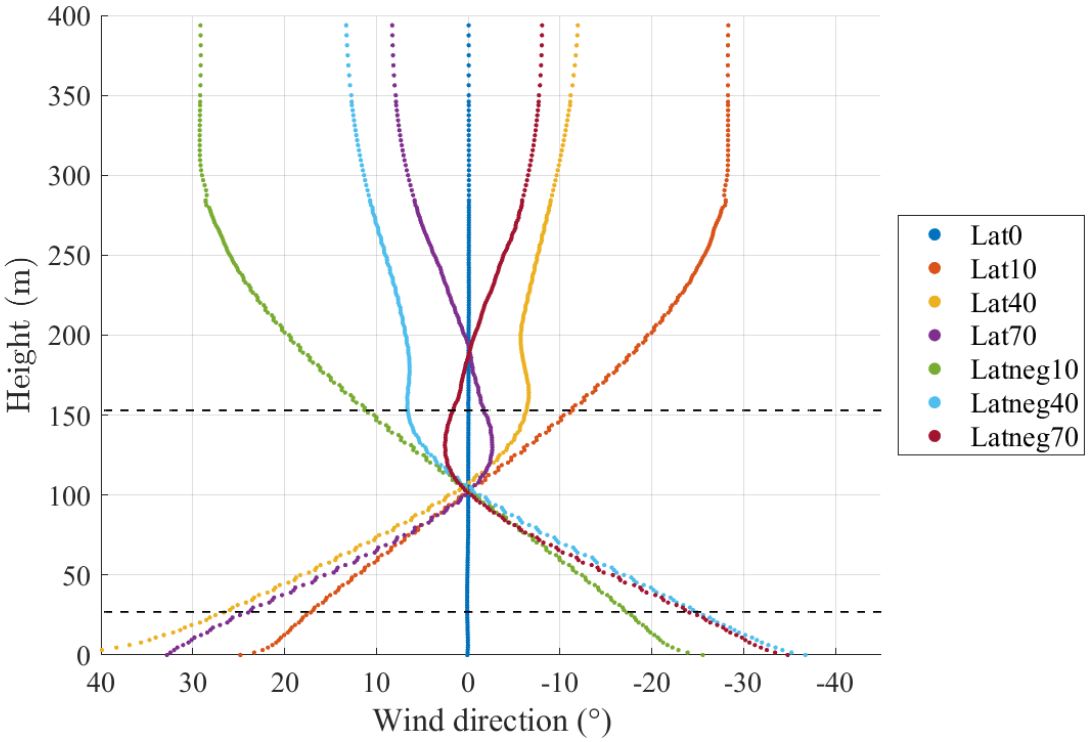

Figure 4.1: Wind veer profiles for each latitude. The dashed lines represent the span of the turbine rotor area.

wind vector direction begins to turn in the opposite direction at about 100 m, maintains an angle of magnitude less than 5° before changing polarity at 180 m.

SOWFA involves the user setting a desired horizontally-averaged streamwise wind velocity at a specified height [26]. This allows the turbine simulations to have controlled wind speeds across the rotor, which is relevant when considering turbine performance in rated and non-rated wind speed regions. Thus, at approximately 100 m, the horizontal wind vector angles for each latitude is 0°.

In the upper region of the SBL, the streamwise and spanwise velocities were observed to sinusoidally oscillate about a constant value over time with the frequency of the oscillation being proportional to the latitude, with Lat10 having the lowest frequency of oscillation. This drives the differences in the wind veer profiles above 100 m, causing them to change direction over time and the higher latitude cases experiencing sharper turns in the profile. The oscillation in velocity components and transient changes in wind veer profile are depicted in Appendix B.1

Although the wind veer profiles are mirrored for positive and negative latitudes, the behaviour of the wake will not necessarily be mirrored exactly for cases of latitude with opposite polarity. The direction of rotation for the blade rotation remains as clockwise under both veering conditions and contributes to the shape and deflection of the wake.

Thus the interaction between the wind veer and cross-stream velocity components due to blade rotation is expected to differ between all the wind veer cases.

4.2 Wake Shape

Figure 4.2 presents a top down view of the wake at hub height to depict the wake propagation with downstream distance. To characterise the shape of the wake, the wake cross-section at $5D$ downstream is first examined to relate the inflow conditions to the wake behaviour. The shape of the wake is influenced by both yawing and due to the wind

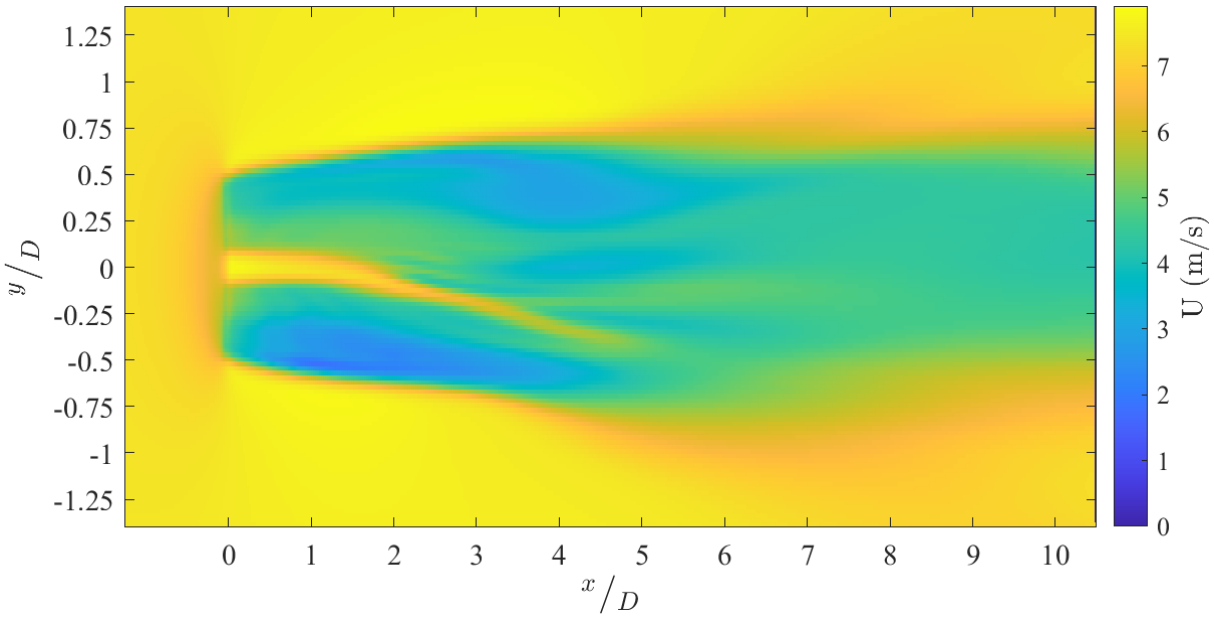

Figure 4.2: Streamwise velocity as viewed from above for a turbine operating in Lat0 Yaw0 conditions.

veer in the inflow conditions. Figure 4.3 presents the cross-section of the velocity deficit for Lat0 Yaw0 and serves as the baseline for comparison with cases of different veers and yaw angles. The cross-section was taken at $5D$ downstream as this distance is in to be in the far wake region, which is where the modelling of the wake is considered to be most applicable. At $5D$ the wake has also developed and recovery to the freestream conditions at this point is minimal.

As expected, Figure 4.3 depicts the reduction in velocity across the wake cross-section relative to the freestream conditions. The shear layer as the wake deficit transitions to the freestream conditions is evident near the edges of the wake as the colour gradient shifts from blue through green to yellow. This wake velocity deficit region is distinct from the freestream flow, with a relatively thin shear layer separating the wake from the surrounding wind. In SBL conditions, wake recovery is slow as there is reduced transfer of momentum from the freestream wind into the wake due to the low level of turbulence present [27].

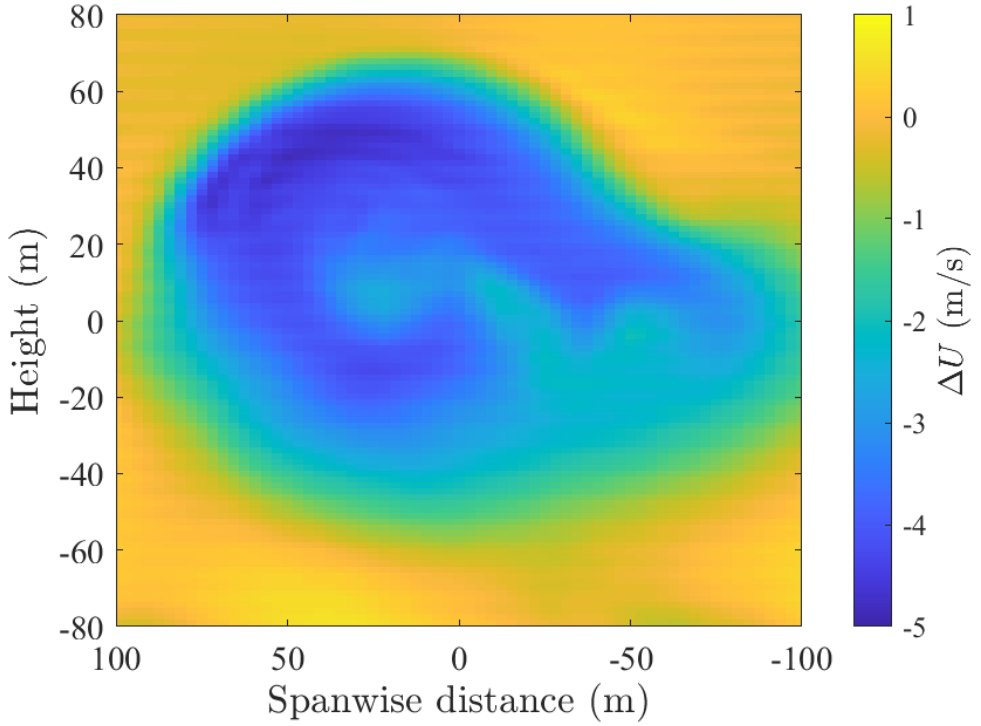

Figure 4.3: Cross-section of the velocity deficit, $\Delta U = U(x, y, z) - U(-1.5D, y, z)$, as viewed from upstream at $5D$ downstream from the turbine for the Lat0 Yaw0 case.

There is also evidence of some regions in the flow experiencing an increase in velocity, as shown by the brighter yellow areas in the bottom left and right of the figure. This occurs per the conservation of mass flow, as the streamtube of wind flow through the turbine expands as it approaches the rotor [10][71]. Thus, in stratified velocity profiles such as the ABL, higher speed air is forced down below the rotor and wake area, resulting in an increase in velocity measured below the wake.

The wake shown in Figure 4.3 has an approximately elliptical shape, with the lateral wake width larger than the vertical. Figure 4.4 thus presents the wake in the Lat0 Yaw0 case at 1D, 3D and 5D downstream from the turbine to depict the wake expansion as it propagates. As seen from Figure 4.3 and Figure 4.4, the wake expands faster laterally with the wake becoming wider in the spanwise direction than the vertical direction as it propagates downstream. The wake shape also appears to 'bulge' on the right side as it travels downstream. The area of freestream flow in the wake due to the absence of the nacelle in the SOWFA actuator line model (ALM) mixes with the wake velocity deficit and advects to the right of the turbine with downstream distance, causing the wake to bulge. The higher velocity freestream wind below the wake region appears to contribute in 'squishing' the wake vertically, causing the spanwise wake width to increase to conserve the mass flow rate in the wake.

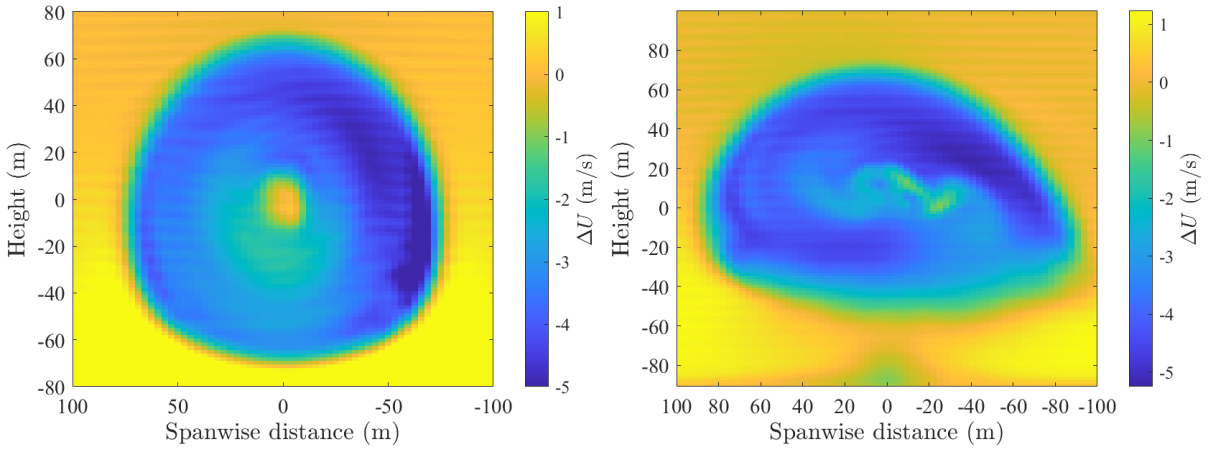

(a) 1D **(b)** 3D

Figure 4.4: Cross-section of the velocity deficit, ΔU, as viewed from upstream.

4.2.1 Effect of yaw on wake shape

The effect of yawing the turbine on the shape of the wake was best demonstrated in the Lat0 case, wherein the effect of veered flow is not involved. Figure 4.5 demonstrates the trajectory of the wake produced from a yawed turbine while Figure 4.6 presents the wake shapes produced by the yawed turbines under non-veered flow conditions. From Figure

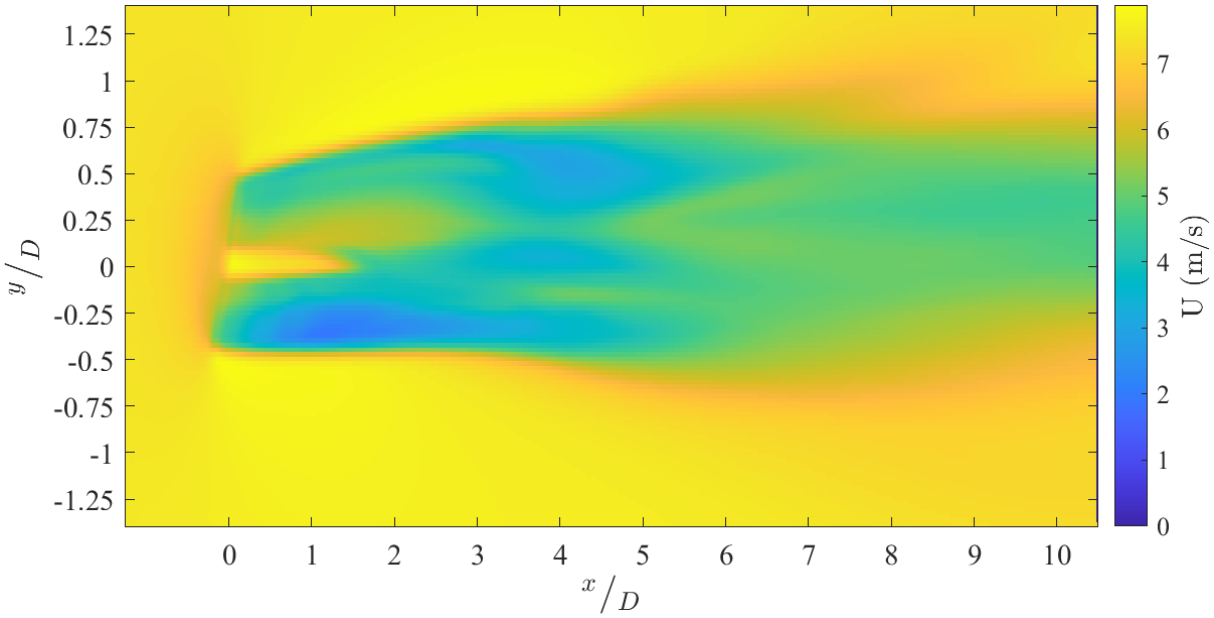

Figure 4.5: Streamwise velocity as viewed from above for a turbine operating in Lat0 Yaw20 conditions.

4.6, the deflection of the wake due to yawing is evident with the Yaw20 case wake having propagated to the right of the turbine and the Yawneg20 case has the wake shifted to the left. The irregular, almost 'kidney-like' wake shape observed from the un-yawed turbine is again seen with both the yawing directions, just offset laterally. The Yaw20 wake shape appears slightly more curled than Yaw0, while the Yawneg20 is less curled. The width of

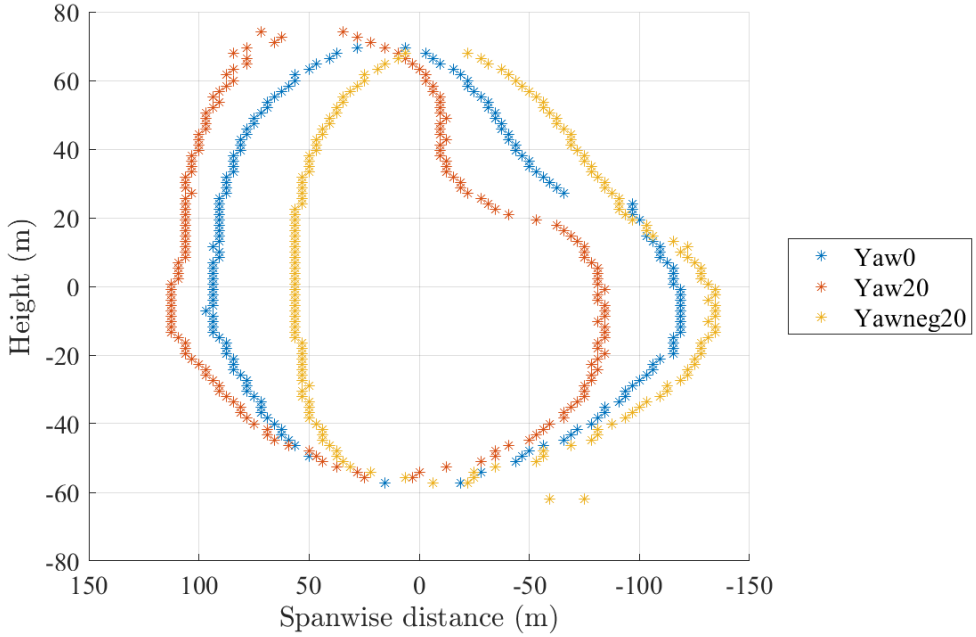

Figure 4.6: Cross-sectional view of wake shapes at 5D downstream of the turbine as viewed from upstream for the three yawing conditions in Lat0 flow.

the wakes from the yawed turbine also appears to be smaller than the un-yawed turbine. When the turbine is yawed, the area of the rotor perpendicular to the streamwise velocity reduces from a circle of diameter D to an ellipse with major vertical and minor horizontal axes of D and $D\cos\gamma$, respectively, where γ is the yaw angle [39]. Thus as the area over which the thrust force is applied is reduced when the turbine is yawed, the wake width is also expected to be smaller.

Figure 4.7 depicts the propagation of the yawed wake shapes as it travels downstream. As the wake propagates downstream, the shape becomes more irregular and continues to

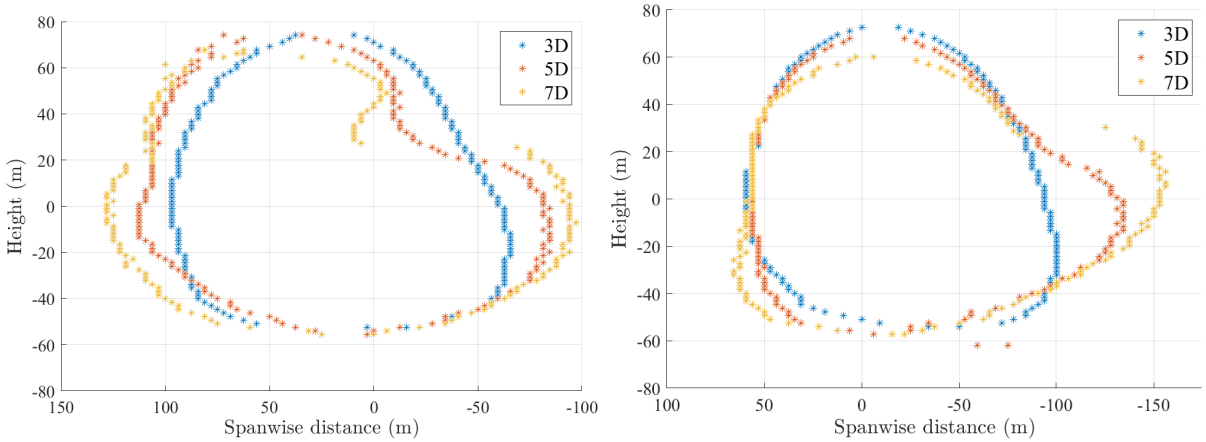

(a) Yaw20 **(b)** Yawneg20

Figure 4.7: Propagation of wake shape for a) Yaw20 and b) Yawneg20 at 3D, 5D and 7D downstream of the turbine.

protrude on the right side. As outlined above, this irregular shape is likely partly due to

the presence of the high speed velocity region in the centre of the wake, in combination with the wake rotation. Yawing introduces a pair of counter-rotating vortices (CRV) at the top and bottom of the rotor and these cause the wake to curl [39][48]. The effect of the CRVs is evident in the enhanced curling of the wake shape with downstream distance seen in Figure 4.7 for both yaw angles.

4.2.2 Effect of wind veer on wake shape

For wakes produced in veered inflow, a common feature across all the cases tested, and as seen above, was the skew of the wake in the same direction as in the wind veer profile for that latitude. Figure 4.8 demonstrates the trajectory of a wake in veered flow as viewed from above to highlight how the wake behaves at different heights across the rotor.

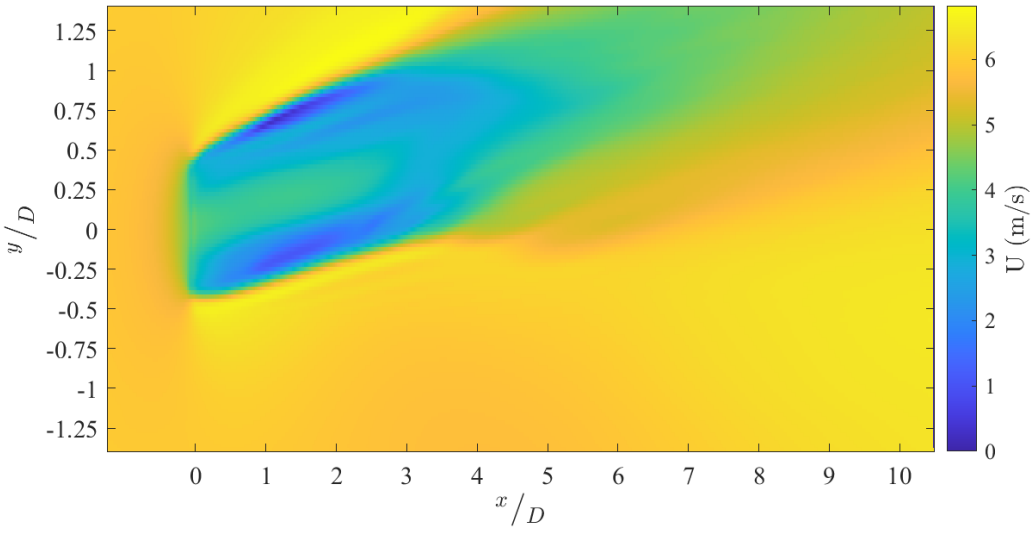

(a) $-0.25D$ below hub height

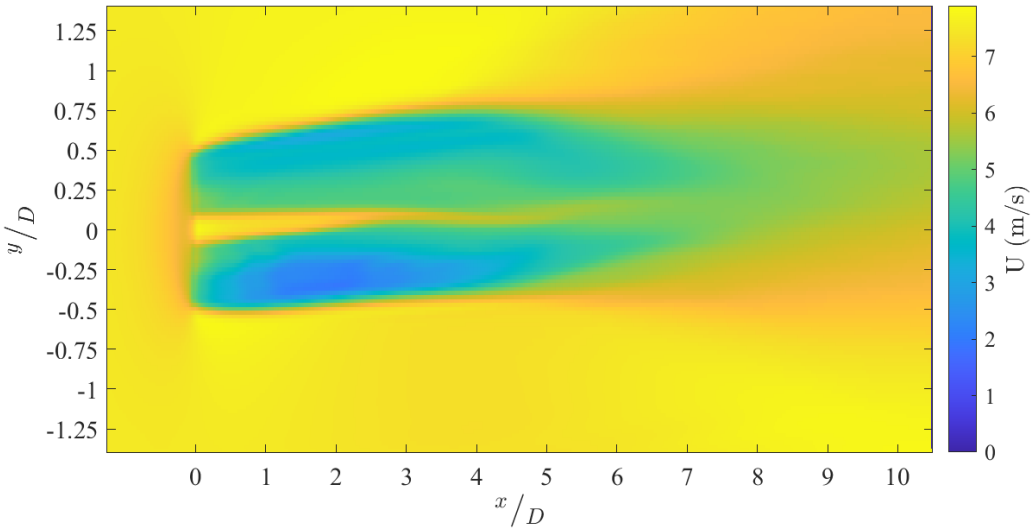

(b) Hub height

Figure 4.8: Streamwise velocity as viewed from above for Lat10 Yaw0 conditions at $-0.25D$ below hub height (top), hub height (middle) and $+0.25D$ above hub height (cont.)

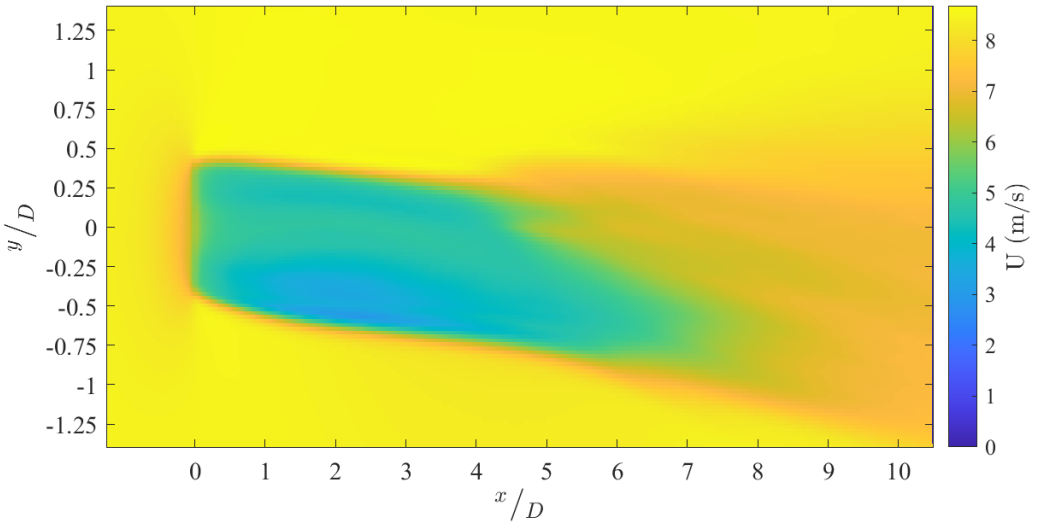

(c) $+0.25D$ above hub height

Figure 4.8: Streamwise velocity as viewed from above for Lat10 Yaw0 conditions at $-0.25D$ below hub height (top), hub height (middle) and $+0.25D$ above hub height.

Figure 4.9 then presents the velocity contour cross-sections as viewed from upstream for some of the latitude cases, depicting the variation in wake shapes associated with different wind veers. The wake skew due to wind veer has similarly been observed in a number of studies [31][32][33][37]. For both the Lat10 and Latneg10, the wake shape skews linearly across the rotor height into a diagonally stretched shape. Whereas for the other non-zero latitudes, the lower half of the wake appears similar to the Lat10 and Latneg10 cases, while the upper half exhibited a lesser degree of skewing. This corresponds to the difference in the wind veer profiles shown in Figure 4.1.

To compare the variations in wake shape between the different latitudes, the edges of the wake were mapped to outline the extent of the velocity deficit area, as exemplified in Figure 4.10 for the Lat10 Yaw0 case. This was achieved by locating the lateral locations where the velocity deficit had decreased to be 15% of the maximum deficit in the wake for various heights across the wake and at each downstream location. Therefore any differences in the wake recovery between conditions is not considered in this definition of the wake shape so that the comparison here only focuses on how the wake skews and not how it also recovers.

Figures 4.11 and 4.12 then present an overlay of each wake outline for both the positive latitudes and the negative latitudes, respectively. These figures contrast the differences in wake shape as produced in the various inflow wind veer conditions. Similar to how the wind veer profiles varied across the upper region of the turbine rotor, so too do the shapes of the wake for each veering case. The Lat0 cross-sectional area appears roughly circular, while the cases with veer exhibit significant skewing.

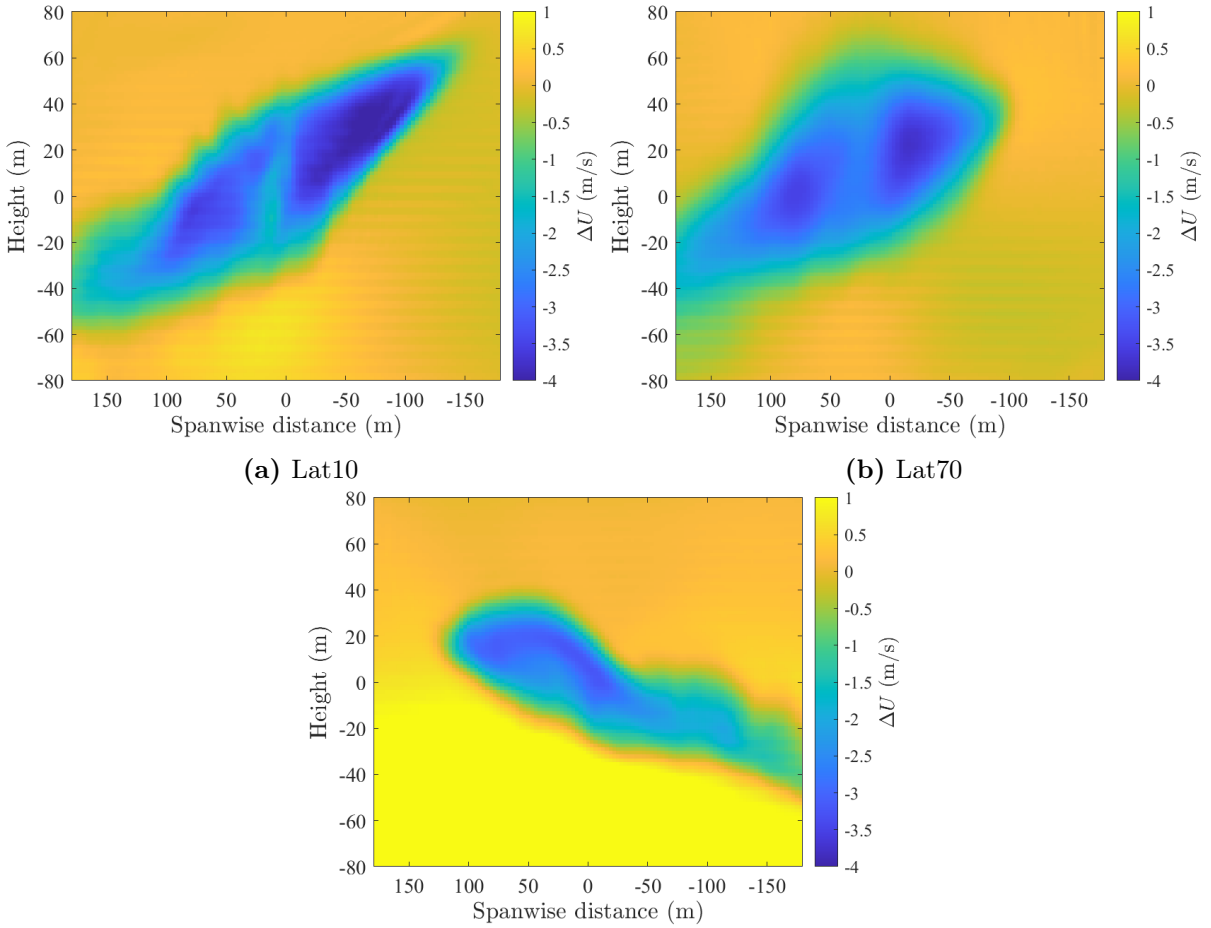

(a) Lat10 **(b)** Lat70

(c) Latneg40

Figure 4.9: Cross-section of the velocity deficit, ΔU, as viewed from upstream at $5D$ downstream from the turbine for various latitudes.

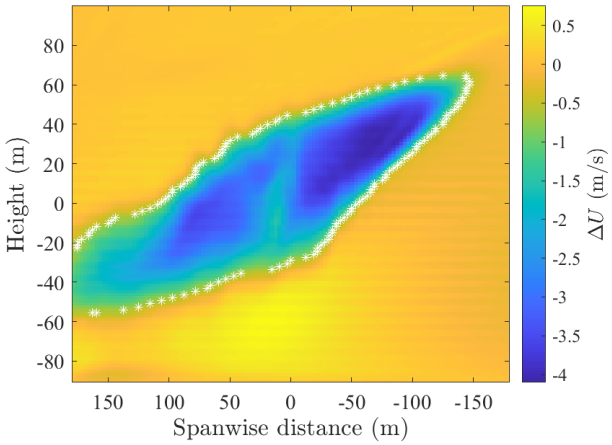

Figure 4.10: Cross-section of the velocity deficit, ΔU, as viewed from upstream at $5D$ downstream from the turbine for the Lat10 Yaw0 case with the wake shaped outlined in white.

The linear skew of the Lat10 case and lower region of the Lat40 and Lat70 cases is again shown by the wake shape in Figure 4.11. However the contrasting of shapes in the wake region above hub height shows the Lat70 shape to present similarly to Lat0. Considering the wind veer profiles as shown in Figure 4.1, this occurs as the wind vector angles are relatively small for Lat70, ranging between approximately 4° and 0° in the upper wake region. While the Lat40 case is more similar to Lat10 in this upper region, though the extent of the skew toward the top right of the figure is less. This relates to the smaller angle for the horizontal wind vector in the upper wake region, with the

Lat40 case maintaining an angle of approximately $-6°$, while the Lat10 case decreases linearly from 0° to -20° between heights of 100m and 200m. The variations in wake shapes observed for the positive latitudes is similarly observed for the negative latitudes, although they are mirrored.

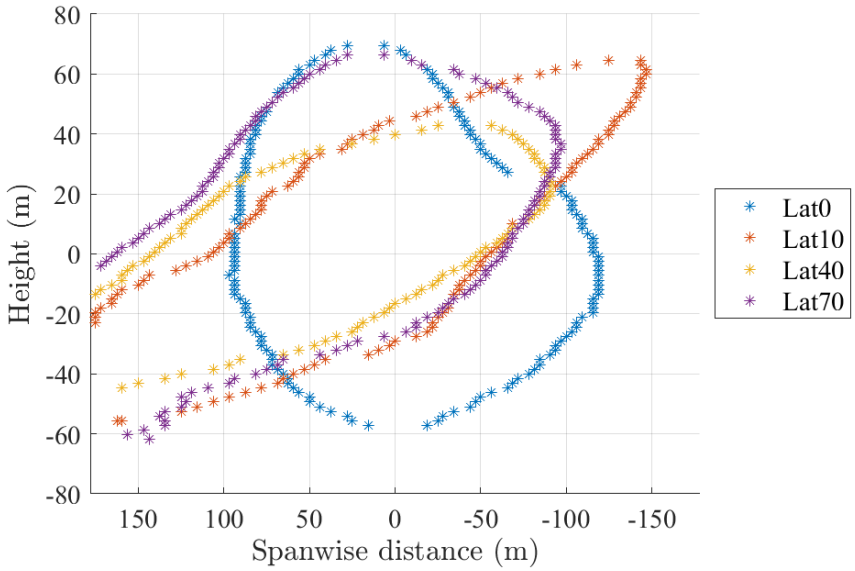

Figure 4.11: Cross-sectional view of wake shapes at 5D downstream of the turbine as viewed from upstream for the positive latitude cases.

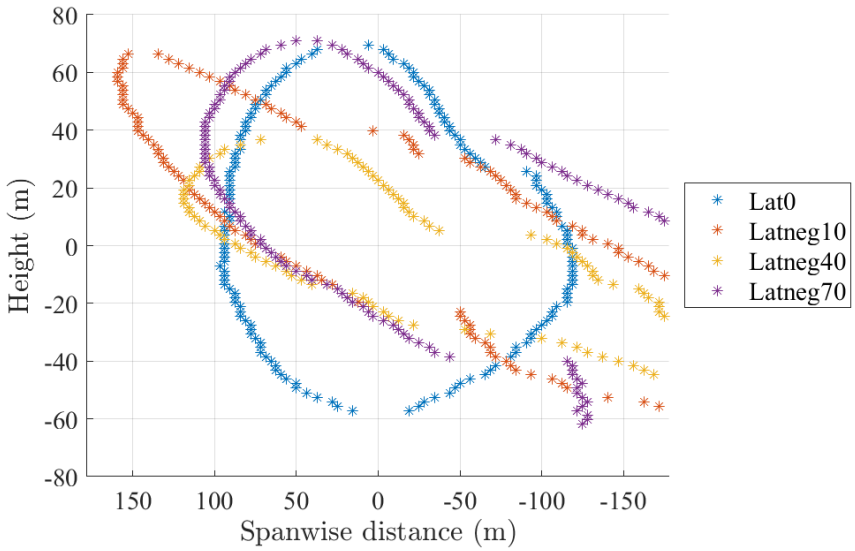

Figure 4.12: Cross-sectional view of wake shapes at 5D downstream of the turbine as viewed from upstream for the positive latitude cases.

4.2.3 Effect of wind veer and yaw on wake shape

When wind veer is present and the turbine is yawed, the shape appears to be mostly influenced by the veer and then slightly offset due to the yaw. Figure 4.13 presents the

wake shapes at various downstream distances for a few of the veer cases, demonstrating that the wake skew associated with the inflow wind veer profile is maintained when yawing is applied. It is also shown that the application of a yaw angle does affect the deflection of the wake, but not to the same extent as observed in Figure 4.6 with the non-veered flow conditions. As shown in Figure 4.13 (b), the Lat70 Yaw20 wake shape differs noticeably

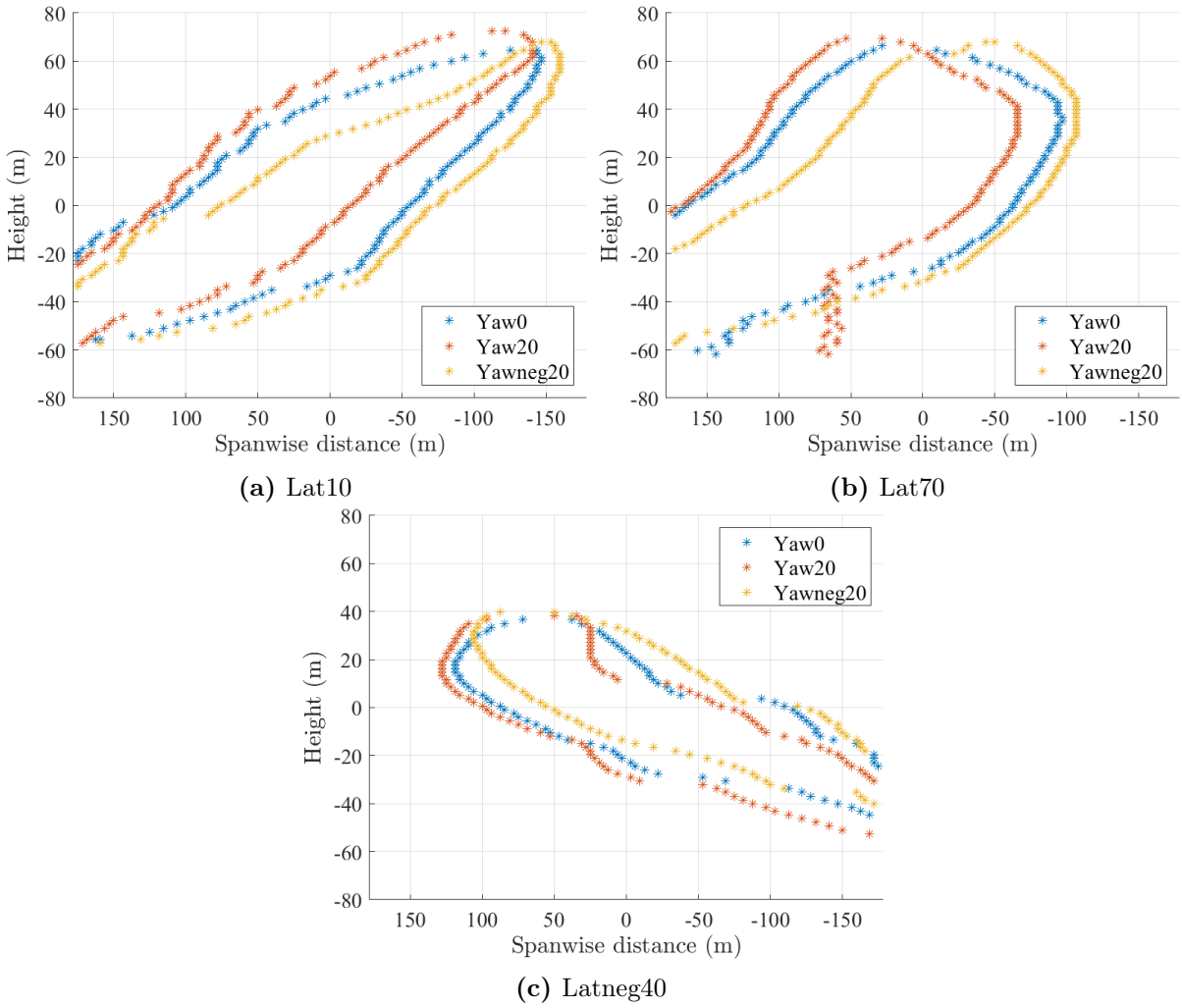

(a) Lat10 **(b)** Lat70

(c) Latneg40

Figure 4.13: Cross-sectional view of wake shapes at 5D downstream of the turbine for each yaw angle tested under a) Lat10 b) Lat70 and c) Latneg40 veering conditions.

in the wake region below hub height from the Yaw0 and Yawneg20 cases. This suggests that applying yaw angles of opposite polarity may affect the wake shape in different ways in veered flow.

4.3 Wake Recovery

The maximum velocity deficit in the wake was tracked at each downstream distance to demonstrate the recovery of the wake, as presented in Figure 4.14. From this Figure, it is seen that the veered inflow resulted in enhanced wake recovery, for both positive and

negative latitudes.

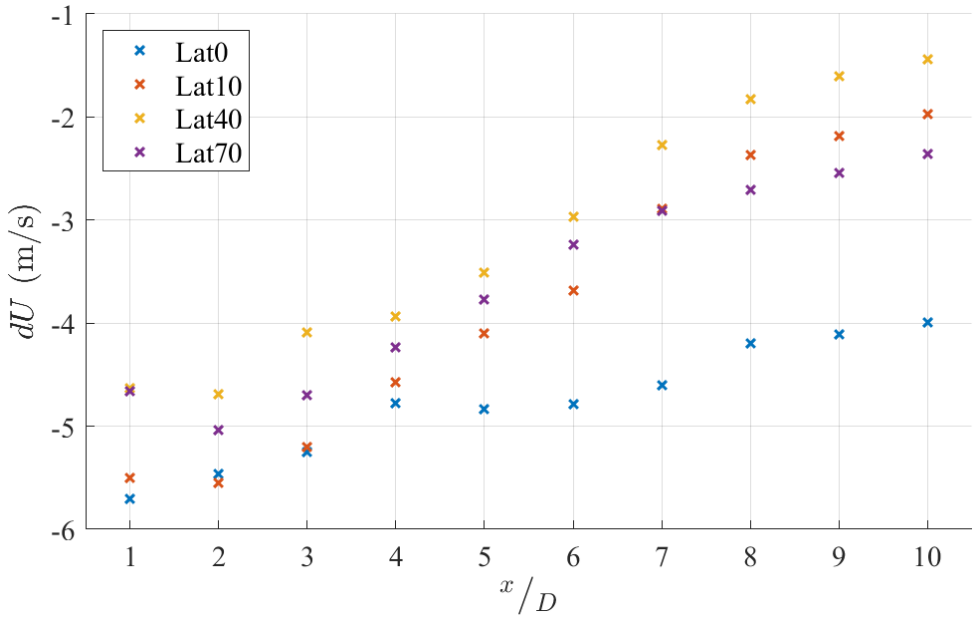

(a) Positive latitudes

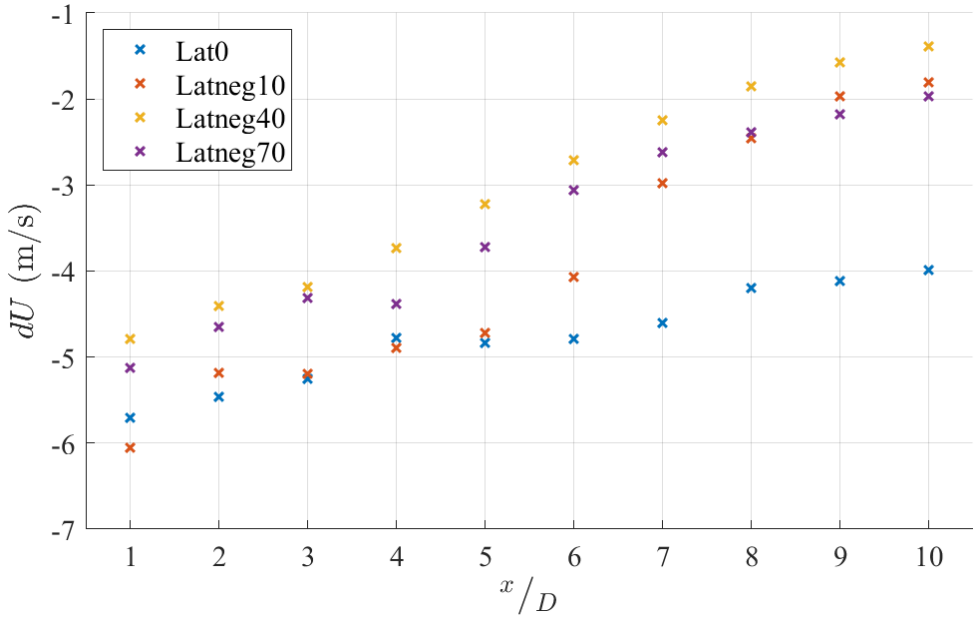

(b) Negative latitudes

Figure 4.14: Maximum velocity deficit in wake from un-yawed turbine at each downstream distance for various latitudes.

The cause for this enhanced recovery has been related to the stretched wake shape that occurs in veered flows having a thinner cross-section than wakes from non-veered flow, allowing the momentum from the freestream conditions to more effectively transfer into the centre of the wake, where the velocity deficit is generally highest [34]. Interestingly, the latitudes of the same magnitude, but opposite polarity, each perform generally the same relative to the other latitude values. Lat40 and Latneg40 both produce wakes that

recover faster than the other latitudes at all downstream distances, though the difference in maximum velocity deficit between each of the veering cases is generally within 1 m/s.

Figure 4.15 depicts the maximum velocity deficit in the wake and how it differs with yawing. Considering the non-veered flow, the recovery of the wake is enhanced by the yawing, with the streamwise velocity deficit. This arises in part due to the reduced thrust forced applied by the turbine onto the flow when the rotor is yawed, resulting in a decreased wake velocity deficit compared with the un-yawed scenario.

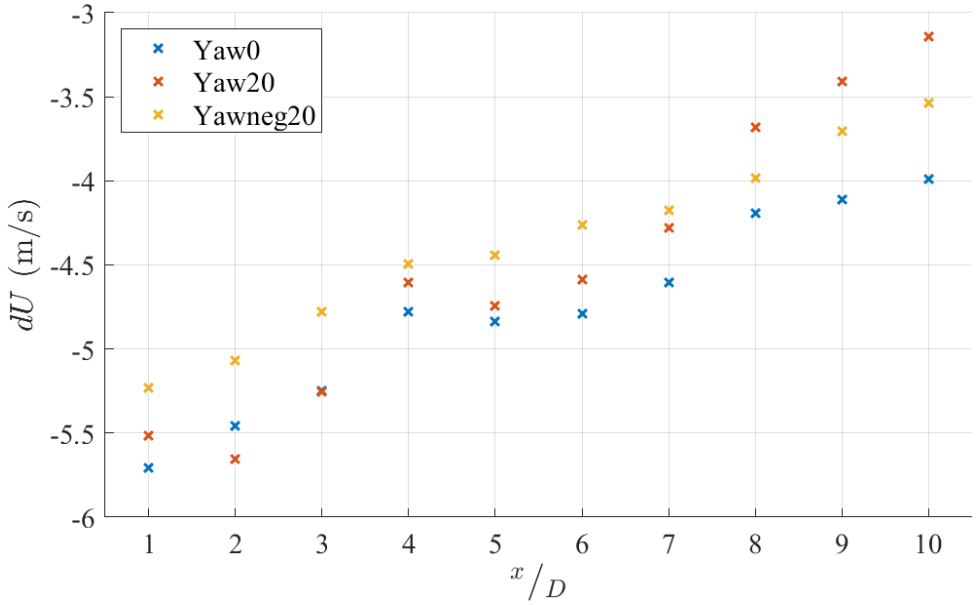

Figure 4.15: Maximum velocity deficit in wake from yawed turbines at each downstream distance in non-veered flow.

When the inflow is veered, the additional recovery due to the yawing is effectively removed, with the three yawing cases producing similar maximum velocity deficit values at each downstream distance for both positive and negative latitudes. This is demonstrated in Figure 4.16 for various latitudes, with the same trends being observed for the latitudes not presented.

4.4 Wake Veer

In veered flow, the trajectory of the wake appears to vary with height, as suggested by the skew in the various wake shapes presented in Section 4.2 and similarly observed by Bromm *et al.* [35]. This occurs as the wake exhibits its own veer profile similar to that of the inflow wind veer, as has been previously indicated by various authors [33][34].

The location of the maximum deficit at each height across the rotor was mapped at each downstream distance to observe the veer of the wake, 'wake veer', and how it compares

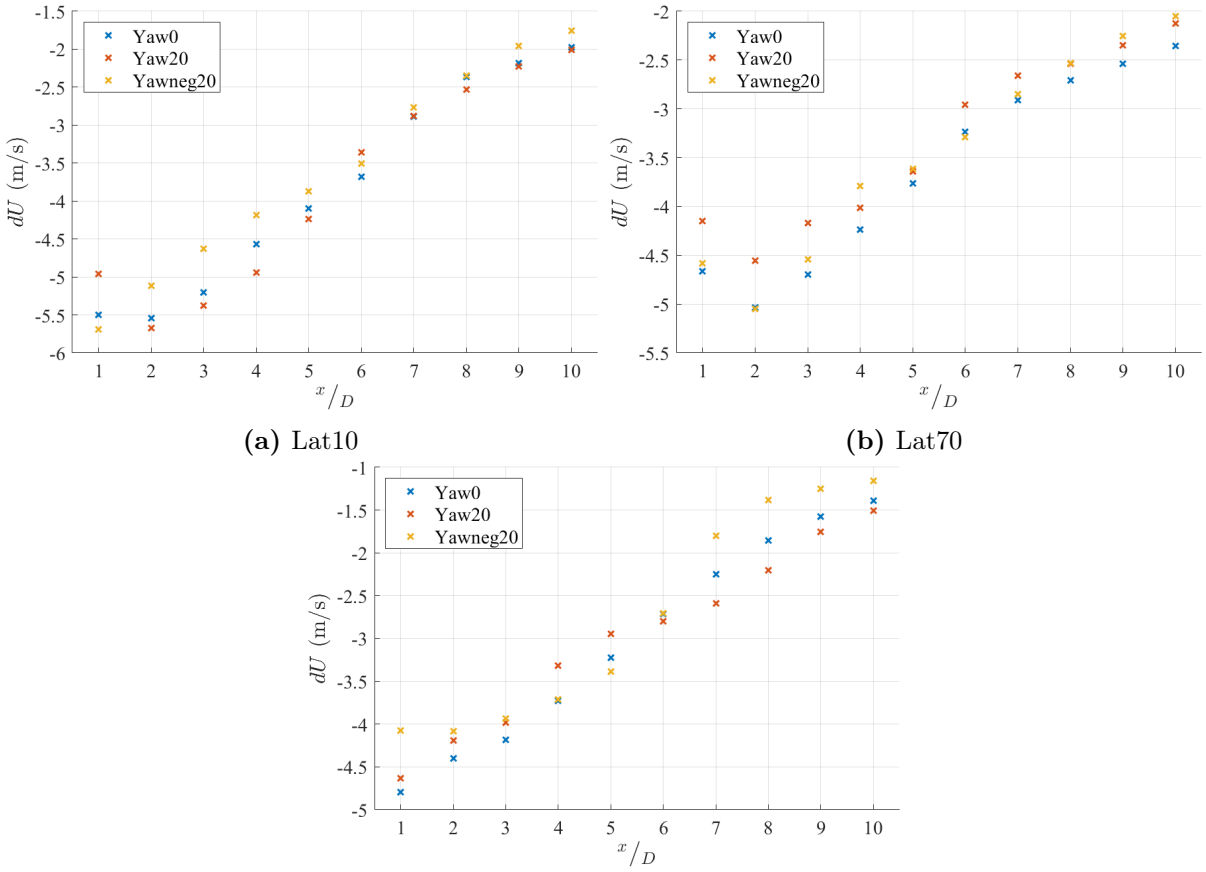

(a) Lat10 **(b)** Lat70

(c) Latneg40

Figure 4.16: Maximum velocity deficit in wake from yawed turbines at each downstream distance for various latitudes.

to the veer of the inflow wind, 'inflow wind veer'. The inflow wind veer was calculated by considering the theoretical displacement of a set of tracer particles due to the inflow wind veer profile [34]. Initially the particles are aligned along the centre, vertical axis of the wind turbine and the lateral displacement is calculated based on the wind speed at each height and the angle of the inflow wind vector at each height, for each downstream distance. This is demonstrated in Figure 4.17 for the Lat10 case as the wake travelled downstream. From Figure 4.17, it is demonstrated that as the wake travels downstream, the wake veer profile tends towards the inflow wind veer profile. For the $3D$ wake veer profile, the curvature arises due to the maximum velocity deficits occurring near the edges of the wake, rather than along the centreline. At this distance, the wake involves a region of relatively high velocity flow in the centre as the nacelle is not modelled by SOWFA. While the exclusion of the nacelle is considered to not influence the far wake region [105], it is present in the near wake and was observed to persist into the far wake, contributing to the maximum velocity deficit at each height being found near the wake edges.

To quantify how the actual wake veer varies from the inflow wind veer, the gradient angle between each consecutive data point in both profiles is calculated and the difference

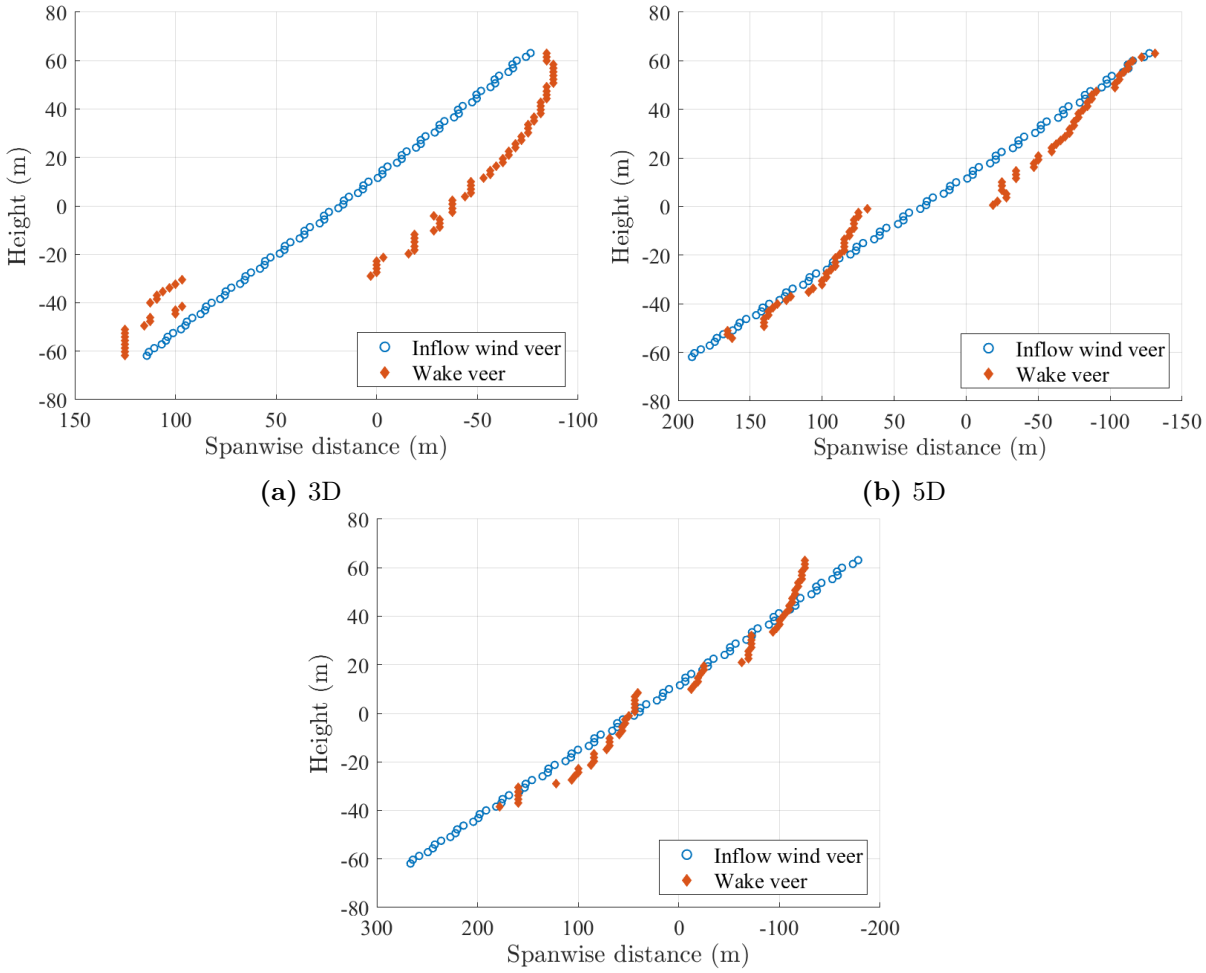

(a) 3D **(b)** 5D

(c) 7D

Figure 4.17: Observed wake veer and inflow wind veer as viewed from upstream for the Lat10 Yaw0 conditions at various downstream distances.

found. The average of these differences is then determined to give an overall indication of how the inflow and wake veer profiles differ. This is similar to the approach taken by Churchfield *et al.* [34] in their comparison of inflow veer and wake veer. However the authors compare the overall gradient angles of linear lines of best fit through their inflow veer and wake veer data. This may be applicable to the Lat10 and Latneg10 cases here, as these exhibit constant gradient, linear wind veer profiles. However, for the other non-zero latitudes, the wind veer profiles are non-linear and the gradient of the inflow veer profile changes with height, so it is more appropriate to compare the piece-wise gradients of each profile. The gradient angle was calculated with respect to the horizontal axis, so a ratio of greater than one indicates the the wake veer data gradient is larger than the inflow veer gradient and thus is less veered – profile is more vertical. Whereas a ratio of less than one indicates the wake veer is more veered – profile is more horizontal.

The veer data was filtered to only include the values within the refined region of the mesh and thus any values that were recorded at the boundary of the refined region were

removed. This is done to limit the comparison of the expected wake veer and observed wake veer profiles to within the refined region. If sections of the wake extended beyond this region, the calculation of the observed wind veer profile would incorrectly return the displacement value associated with the edge of the refined region for multiple heights. This would lead to an inaccurate calculation of how the observed veer profile deviates from the expected veer.

Figure 4.18 presents the ratio of observed wake veer to expected wake veer at each downstream distance for each latitude tested with Yaw0. As depicted, the similarity

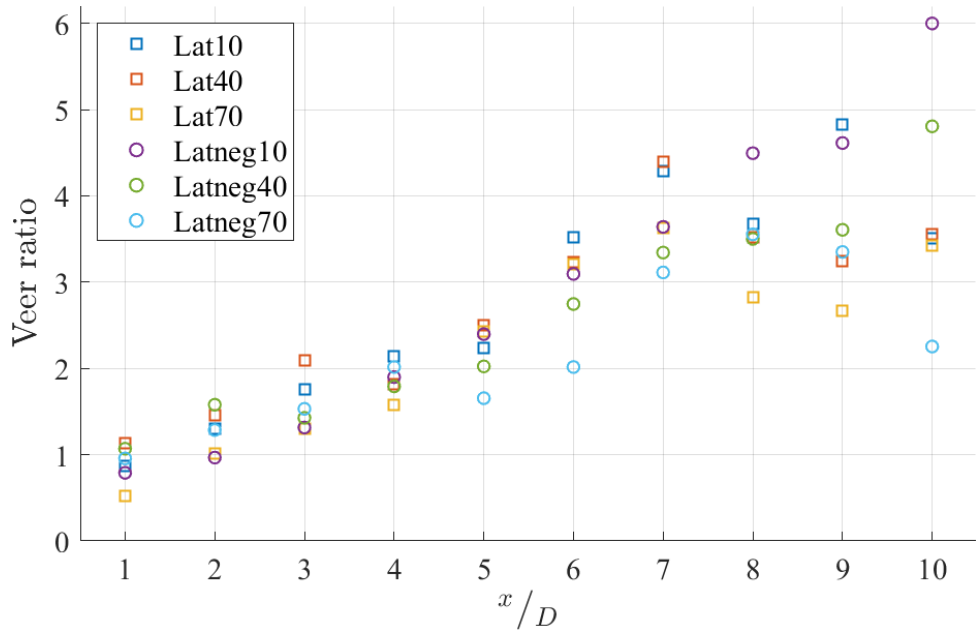

Figure 4.18: Average ratio between angle of wake veer profile and angle of inflow veer profile at each downstream distance for each latitude case. A value of 1 indicates the profiles are on the same angle relative to the horizontal, while a value of greater (less) than 1 indicates the wake veer profile is aligned closer to the vertical (horizontal) axis and is considered to be less (more) veered than the inflow.

in profile angle between the wake and the inflow wind veer decreases with downstream distance. This was similarly observed by Churchfield *et al.* [34], who found the ratio of wake to inflow veer profiles to decrease with downstream distance, with the wake veer being most similar to the inflow at $1D$ downstream. Here the wake veer profiles are most closely aligned with the inflow veer profile at $1D$ or $2D$ downstream for each latitude.

As the wake propagates downstream, the wake veer profile becomes less correlated with the inflow veer as indicated by the increasing average ratio. Bodini *et al.* [33] also observed the wake veer profile to differ with the inflow veer, with the authors relating this difference to the interaction between wake rotation and inflow veer profile reducing the influence of the inflow veer on the wake. Churchfield *et al.* [34] also highlight that the wake velocity deficit does not act as a passive tracer, but is advected by the momentum of the rotating wake.

The trend shown in Figure 4.18 is the same for both positive and negative latitudes. The clockwise rotation direction and speed of the blades was the same for all simulations and so each wind veer profile is interacting with the same cross-stream components from rotation in the wake.

As both Churchfield *et al.* [34] and Bodini *et al.* [33] suggest the wake veer is less than the inflow veer as the cross-stream velocity components due to rotation lessen the effect of the inflow veer cross-stream velocity for positive latitudes, a different relationship between wake veer and inflow veer would thus be expected for negative latitudes. Further analysis on how the interaction between cross-stream velocity components from the inflow veer and wake rotation varies across the height of the rotor is thus needed to understand the relationship between wake veer, wake rotation and inflow wind veer profiles.

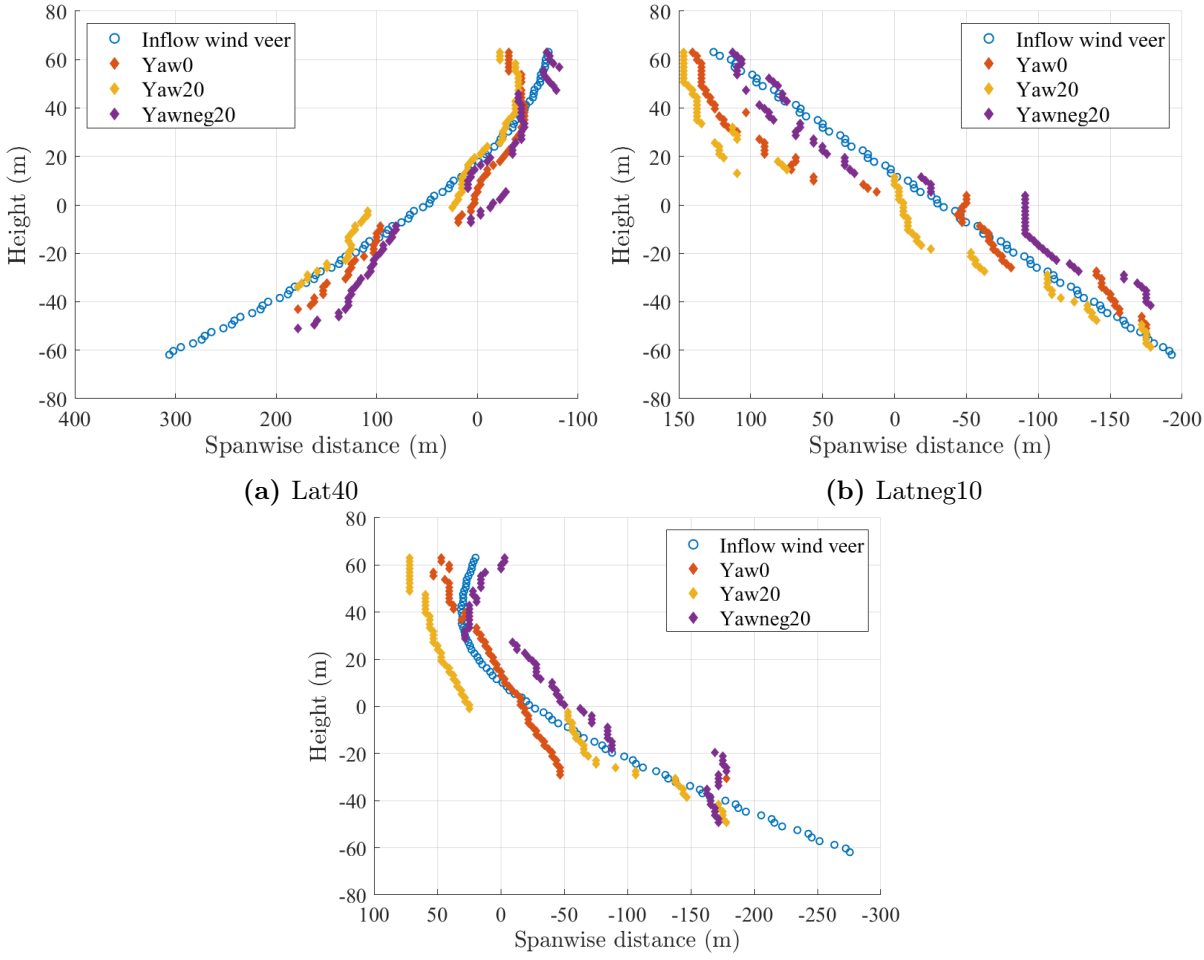

(a) Lat40 **(b)** Latneg10

(c) Latneg70

Figure 4.19: Observed wake veer and inflow wind veer as viewed from upstream for the a) Lat40 b) Latneg10 and c) Latneg70 conditions for each yaw angle at $5D$ downstream of the turbine.

When the turbine is in yaw, the gradient of the wake veer profile appears to remain the same as the Yaw0 case, however the profile is offset laterally, with the displacement direction corresponding to the sign of the yaw. Figure 4.19 presents the wake veer profiles

for each yaw angle at various latitudes and thus suggests that the wind veer primarily causes the wake shape to skew, while yawing displaces the wake laterally. How the wake is offset due to yaw and the nature of the wake shape skew, however, both contribute to the flow conditions experienced by downstream turbines in a wind farm. So while veer may not necessarily displace the wake in the same way yawing does, there is a directional impact on the downstream turbine power production due to the extent and direction of the wake skew. Some skew directions in certain regions of the wake may result in favourable downstream flow conditions, while a different direction of skew may lead to poorer conditions. Thus the effect of both veer and yaw on the effective wake deflection must be considered in wake steering.

4.5 Wake Deflection

Wake steering works on the principle that yawing the rotor of the turbine will cause the wake to deflect away from turbines downstream. As discussed previously, the inflow veer does not necessarily cause the wake to deflect but the directions in which the wakes skew does influence the downstream flow conditions and thus where the minimum power method considers the wake centre. This effect will henceforth be referred to as 'deflection due to veer' and treated as a source of deflection.

4.5.1 Effect of yaw on wake deflection

Yawing the turbine in non-veered flow results in the wake deflecting proportional to the applied yaw angle, as shown in Figure 4.20. The deflection for the Yaw0 case demonstrates that some wake deflection occurs due to wake rotation and the stratified velocity profile. As the wake rotates counter-clockwise, opposite to the clockwise rotation of the blades, slower velocity air flow near the ground is rotated up toward the right side of the wake [11][19]. Similarly, the faster velocity air is rotated down from near the top of the wake to the left side of the turbine. This causes the wake to propagate slower on its right side and faster on the left, resulting in the wake deflecting to the right. Figure 4.20 suggests this deflection to the right due to wake rotation occurs in the near wake, for up to 3D downstream, after which the wake deflects to the left of the turbine.

The wake deflection to the left of the turbine in the far wake region coincides with the downstream distances where the observed 'bulging' in wake shape occurs, as seen in Figures 4.6 and 4.7. The wake centre is considered to be the lateral location with the least favourable flow conditions for power production by a downstream turbine, which are influenced by the propagation of the irregular, curled wake shape generated from the un-yawed turbine in non-veered flow. As the region of velocity deficit experienced by the

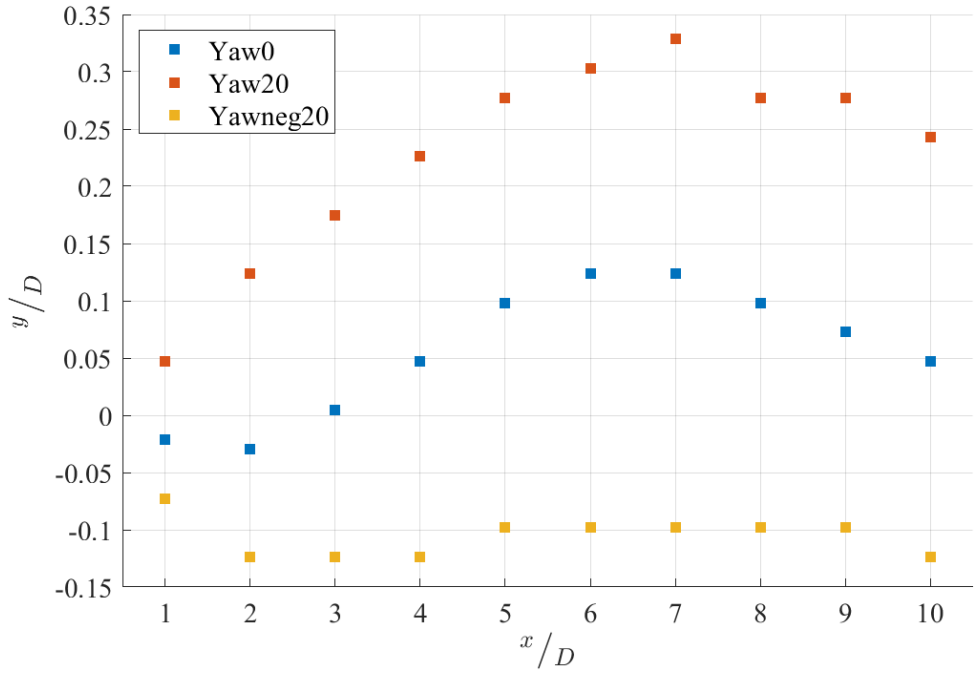

Figure 4.20: Wake centre location with downstream distance as viewed from above the yawed turbine for Lat0 flow conditions. Positive (negative) values refer to deflection to the left (right) of the turbine and both streamwise and spanwise distances have been normalised by the turbine diameter, D.

downstream turbine is larger, available power in the flow is lower on the left and the wake centre tends to this side. Whereas, on the right side of the turbine, the curled wake shape means a downstream turbine is partially exposed to the wake and partially exposed to the freestream flow, thus the available power is more favourable on the right.

The magnitude of deflection associated with the Yawneg20 turbine is also noticeably smaller than that of the Yaw20 turbine and similar to Yaw0, though the direction of deflection is opposite. Relative to the deflection observed for Yaw0, however, the offset of the wake centre for Yaw20 and Yawneg20 is quite similar. This suggests that when applying a yaw angle of $-20°$, the deflection must counter-act the Yaw0 deflection and so the net deflection to the right is less effective than the deflection achieved by implementing a 20° yaw angle.

The change in direction of the deflection observed at $7D$ downstream for Yaw0 and Yaw20 coincides with regions of the wake recovering and the extents of the wake shape becoming less defined. From 7D, the region of velocity deficit begins to diffuse vertically and laterally outward and its influence on the available power in the wind changes. The wake centre trend is then observed to converge toward zero as the areas of the wake with the largest velocity deficit that persist downstream become more concentrated near the centre of the lateral domain. For Yawneg20, the maximum velocity deficit areas persist at a negative offset location and so the trend of the wake centre toward zero is not observed.

Should the region of wake analysis be extended beyond $10D$ downstream, all three yawing conditions are expected to demonstrate a convergence of the wake centre location back to zero as the wakes recover.

4.5.2 Effect of veer on wake deflection

The skew of the wake due to inflow wind veer has an impact on the location of the wake centre, with Figure 4.21 presenting the wake deflection associated with the various latitudes tested in this study. While the wake skew, particularly for Lat10 and Latneg10, was observed to occur toward the top-right and bottom-left, the direction of deflections shown in Figure 4.21 correspond to the direction the wake skews due to veer in the region below hub height. It should also be noted that $y/D = \pm 0.8492$ are the maximum lateral offsets possible from this data as beyond these values, the theoretical downstream turbine rotor area would extend beyond the refined region of the domain. For positive latitudes,

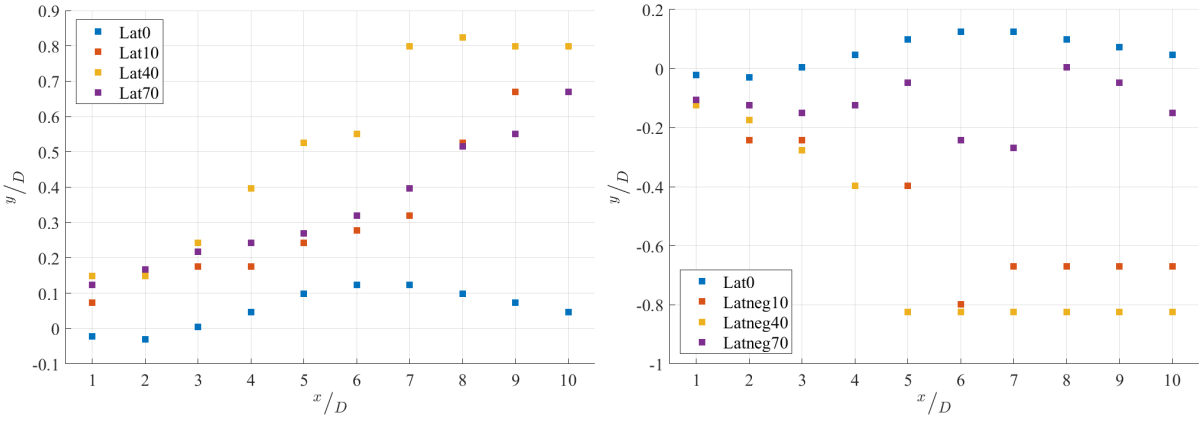

(a) Positive latitudes **(b)** Negative latitudes

Figure 4.21: Wake centre location with downstream distance as viewed from above the turbine for a) positive and b) negative latitudes for the Yaw0 turbine.

the wind veer skews the lower wake to the left, while the lower wake is skewed to the right for negative latitudes. Considering the wind veer profiles for the $\pm 40°$ and $\pm 70°$ latitudes, as shown in Figure 4.1 the veer is stronger in this lower wake region. The lateral propagation of the wake velocity deficit is thus more prominent below hub height for these latitudes, whereas above hub height the wake is skewed comparatively less and so the overall velocity deficit region remains more central and to the left of the upstream turbine. While the veer profile is linearly increasing, for the Lat10 and Latneg10 flow conditions, the magnitude of the wind vector angle is larger below hub height than those above the hub and so greater wake skew of the lower wake region is expected. For the Lat40 case, the magnitude of the wind vector angle below hub height is larger than the other positive latitudes and the effect of this is demonstrated in the greater deflection achieved by the Lat40 Yaw0 case relative to the other latitudes. Similarly, Latneg40 Yaw0 demonstrates a

slightly greater magnitude wake deflection compared with the other negative latitudes.

While the wake skew is greater in the region below hub height, Figure 4.9 shows the maximum velocity deficits generally occurred in the centre and upper region of the wake, which was similarly observed for the latitudes not presented. Thus, the locations of the wake centres are not occurring where the maximum velocity deficits are measured. This suggests that the presence of the surrounding freestream flow conditions and perhaps also the definition of wake centre used in this study contribute to the determined wake deflection. The freestream velocity is stratified, with slower velocities occurring close to the ground and increasing in speed with height. As the lower wake region expands and skews, the wake mixes with the slower velocity flow nearer the ground, whereas the upper wake region expands and skews into higher velocity flow, as depicted in Figure 4.22 for various latitudes. It is thus possible that overall flow conditions observed near where the lower wake skews are less favourable for power production than in the region where the upper wake skews as the higher velocity freestream flow conditions in this area balance out or compensate for the presence of the wake velocity deficit. The stratified inflow also means that a velocity deficit closer to the ground results in slower streamwise wind conditions than the same velocity deficit nearer the top of the rotor. Thus the available power in the wind flow below hub height could be less than that above hub height, depending on the magnitude and distribution of the velocity deficit in the wake.

4.5.3 Effect of veer and yaw on wake deflection

The general trend from the comparison of wake centre deflection for the veered and non-veered cases, is that the wind veer significantly affects the location of the wake centre and often negates any effect of the yawing. As shown in Figure 4.23, the overall deflection direction generally remains as positive for positive latitudes and negative for negative latitudes, regardless of the applied yaw angle. This suggests that relative to the wake skew from the inflow wind veer, the deflection due to yaw has a lesser impact on the wake behaviour in these simulations. As the latitude and thus Coriolis forcing increases, the similarity between the Yaw20 and Yawneg20 deflections profiles is observed to diverge. The change in direction of the wake centre from approximately $7D$ downstream that was observed for the Yaw0 and Yaw20 cases in the non-veered flow is also not observed in these veered conditions, suggesting the change in wake shape and presence of strong lateral velocities influences how the wake recovers and thus how it is observed to deflect.

This is again demonstrated in Figure 4.24, which presents the wake deflection that occurs for the same yaw angle, but different latitudes.

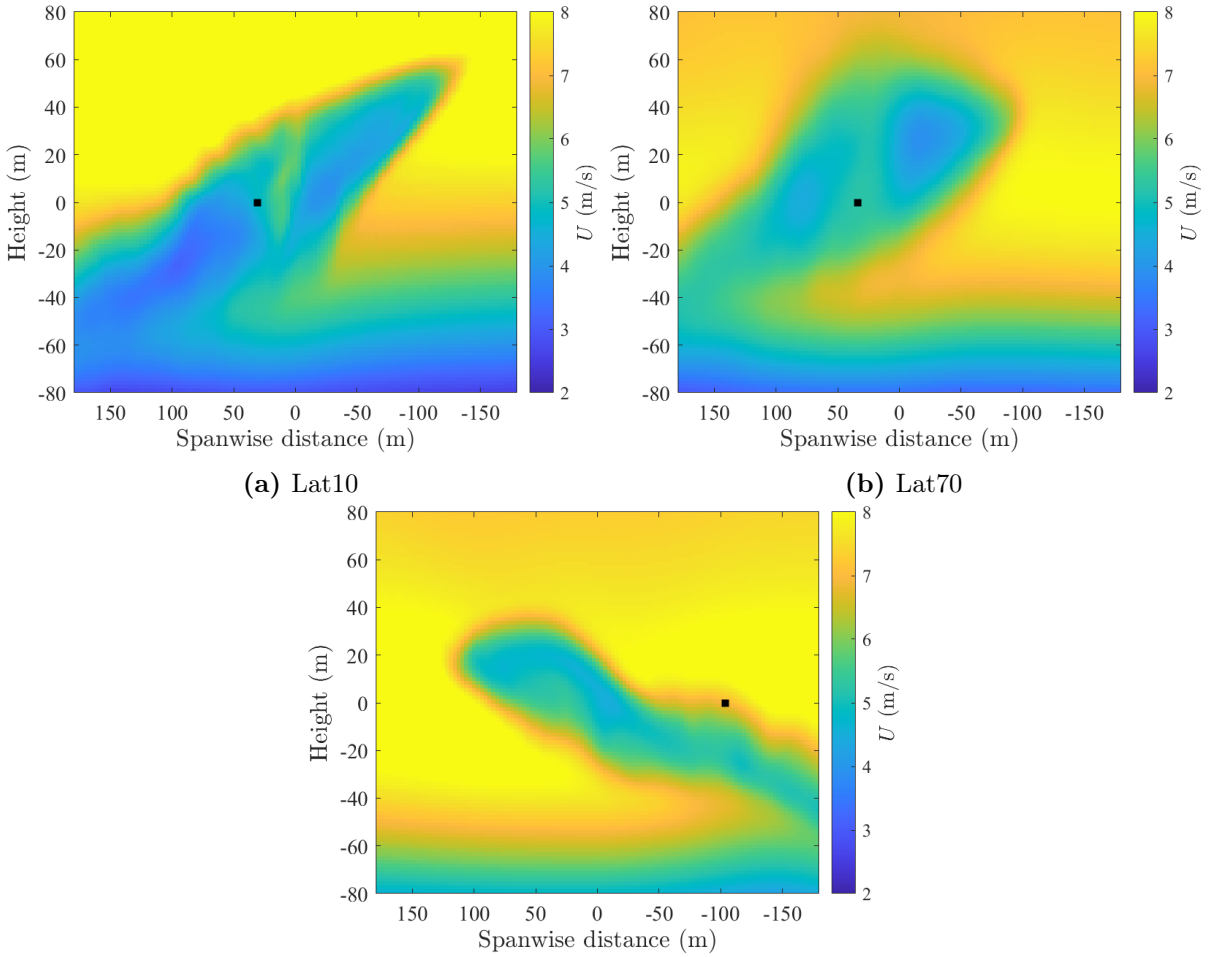

(a) Lat10 **(b)** Lat70

(c) Latneg40

Figure 4.22: Streamwise velocity contours as viewed from upstream at $5D$ downstream for various latitudes. The black square indicates the location of the wake centre.

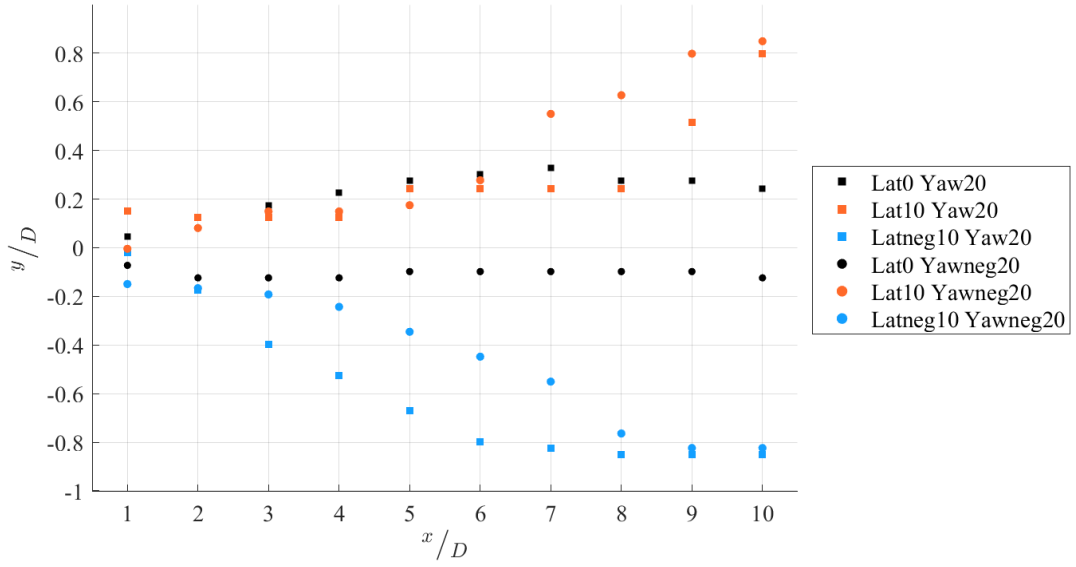

(a) Lat10 and Latneg10

Figure 4.23: Wake centre location with downstream distance as viewed from above the turbine for each of the latitudes and yaw angles tested. The deflections due to yaw for Lat0 are also included as a reference point (cont.).

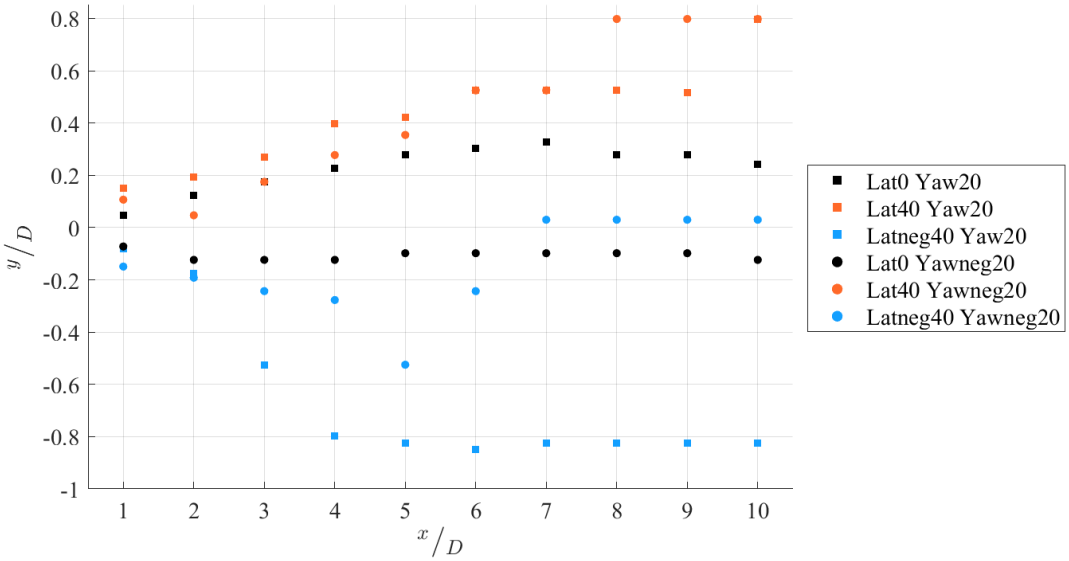

(b) Lat40 and Latneg40

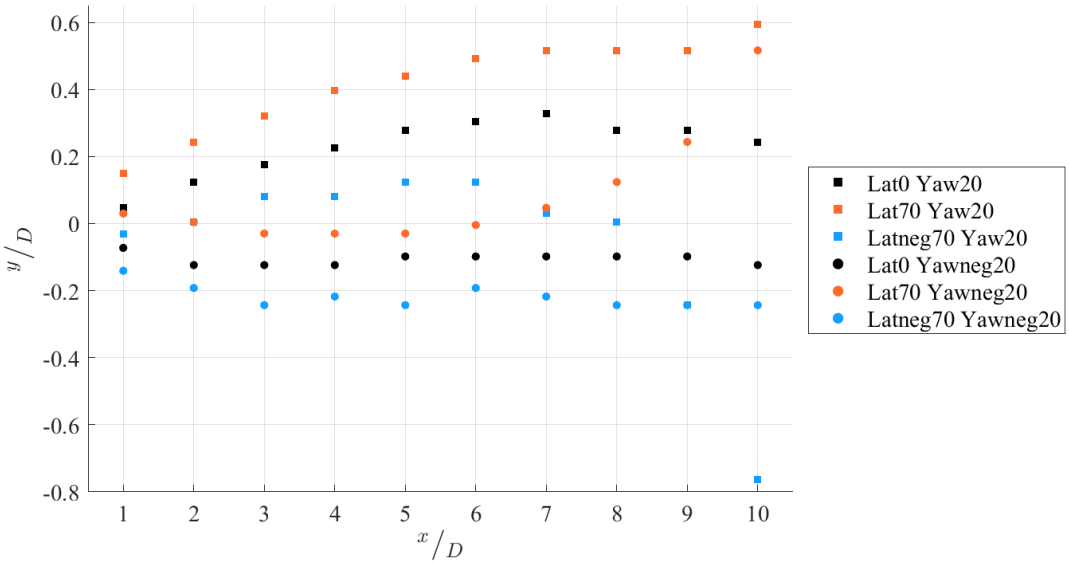

(c) Lat70 and Latneg70

Figure 4.23: Wake centre location with downstream distance as viewed from above the turbine for each of the latitudes and yaw angles tested. The deflections due to yaw for Lat0 are also included as a reference point.

To analyse how veer and yaw separately influence the wake deflection in veered flow, the deflections due to both veer and yaw were isolated. This assists in revealing if the deflections from yaw and veer superimpose when both are present or if the interaction between the yawed turbine and veered inflow is more complex. The isolated deflection due to yaw was found by considering a baseline deflection given by Lat0 Yaw0 and calculating the change in wake centre location that occurs between this baseline case and that of Lat0 Yaw20 and Lat0 Yawneg20. Figure 4.25 thus presents the isolated deflection due to yawing.

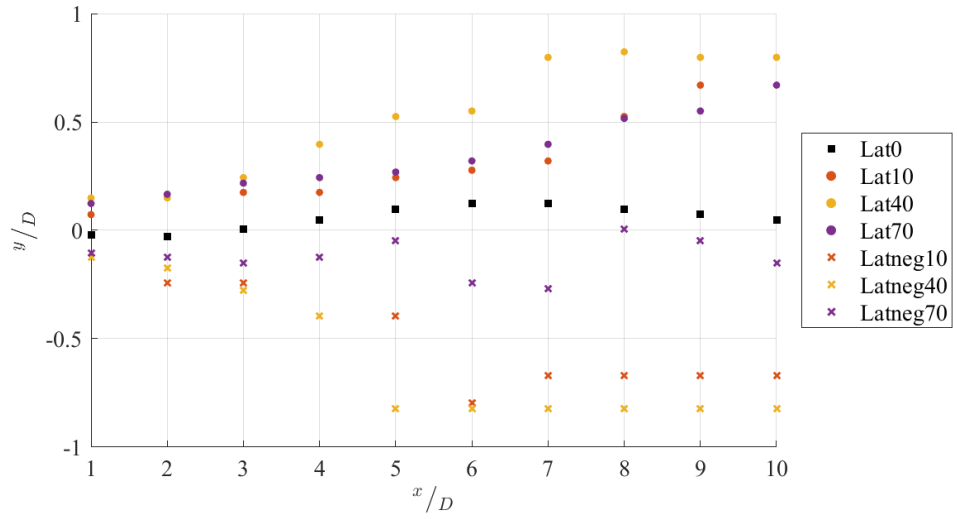

(a) Yaw0

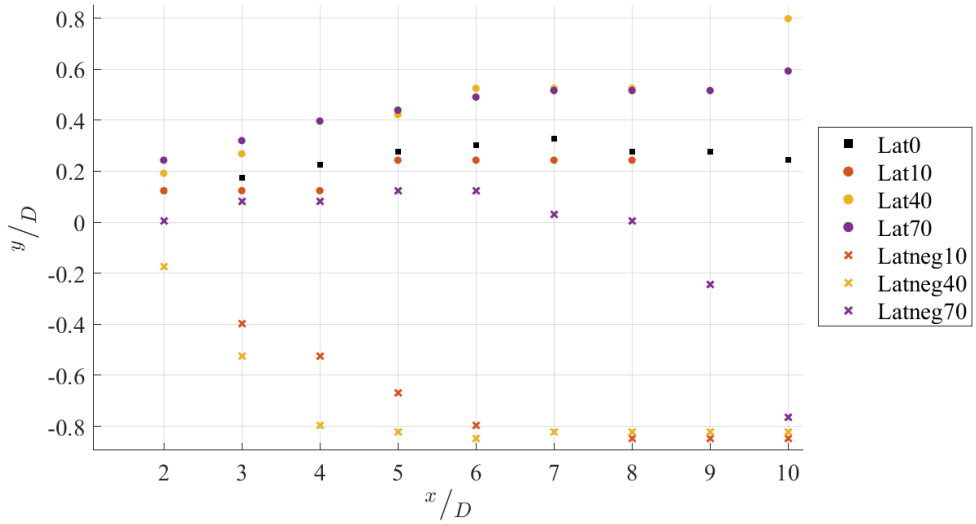

(b) Yaw20

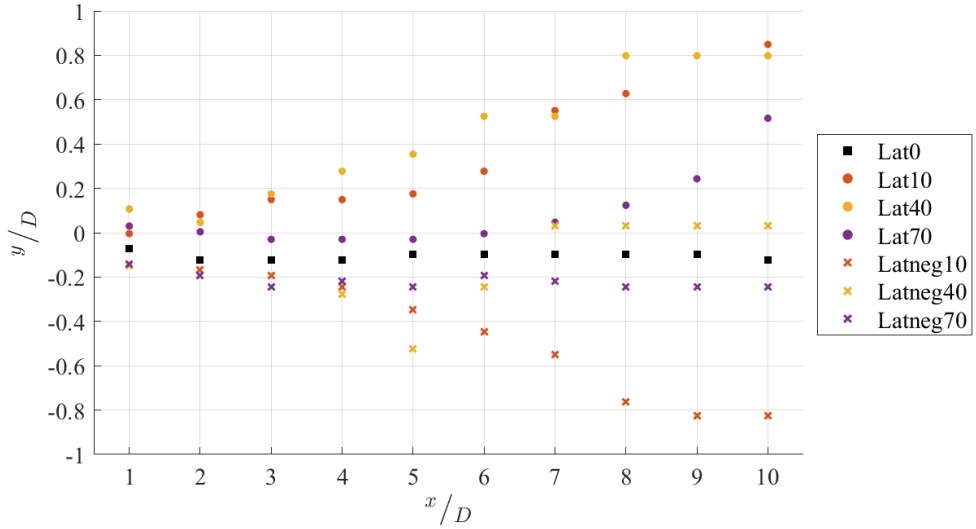

(c) Yawneg20

Figure 4.24: Wake centre location with downstream distance as viewed from above the turbine for each of the latitudes and the same yaw angle. The deflections due to yaw for Lat0 are also included as a reference point.

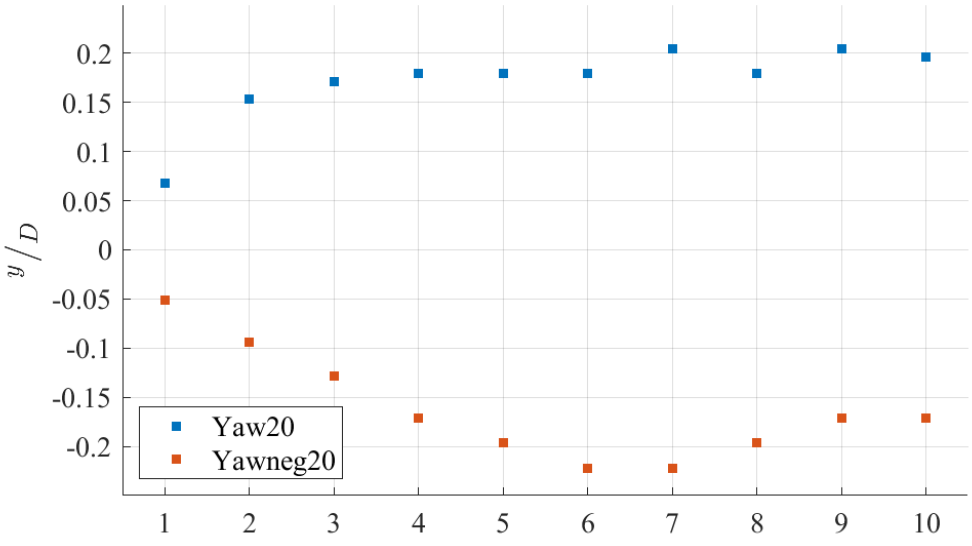

Figure 4.25: Isolated wake deflection with downstream distance for both Yaw20 and Yawneg20.

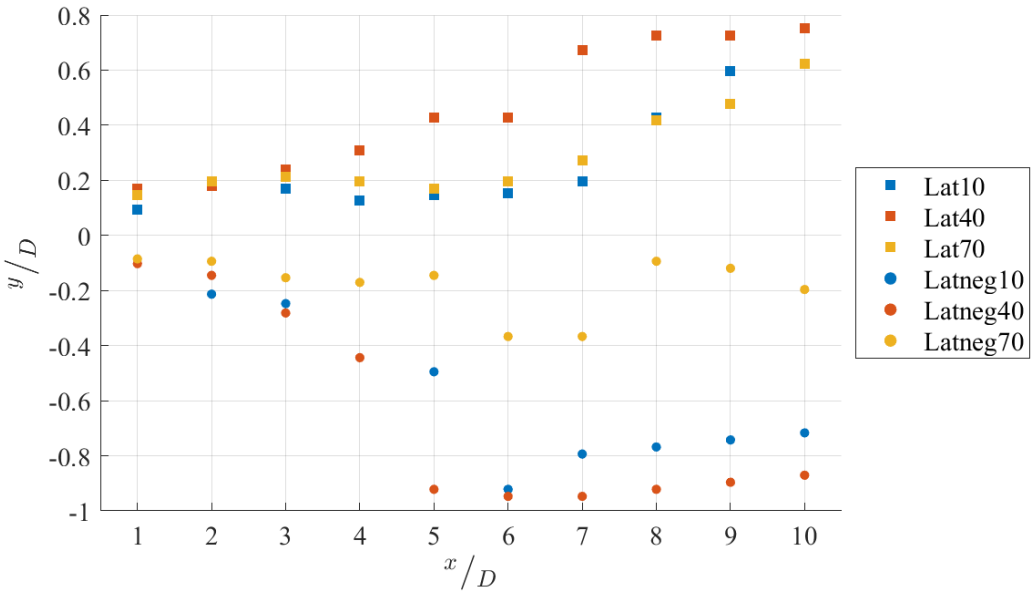

Figure 4.26: Isolated wake deflection with downstream distance for each of the latitudes.

The same approach was taken to obtain the isolated deflections due to veer, with Lat0 Yaw0 again providing the baseline deflection and change in wake centre location from this baseline calculated for the Yaw0 case of each latitude, as presented in Figure 4.26. If the deflections due to veer and yaw superimpose, then the deflection associated with Lat40 Yaw20, for example, would be the sum of the deflection due to a 20° yaw angle and the deflection due to 40° latitude veer. Figure 4.27 depicts the superimposed wake deflections alongside the observed wake deflection and the deflection due to veer alone for various combinations of yaw and latitude.

From this analysis, it was observed that the deflections due to yaw and veer do not just simply add together. Instead, the deflection of the wake appears to be very much

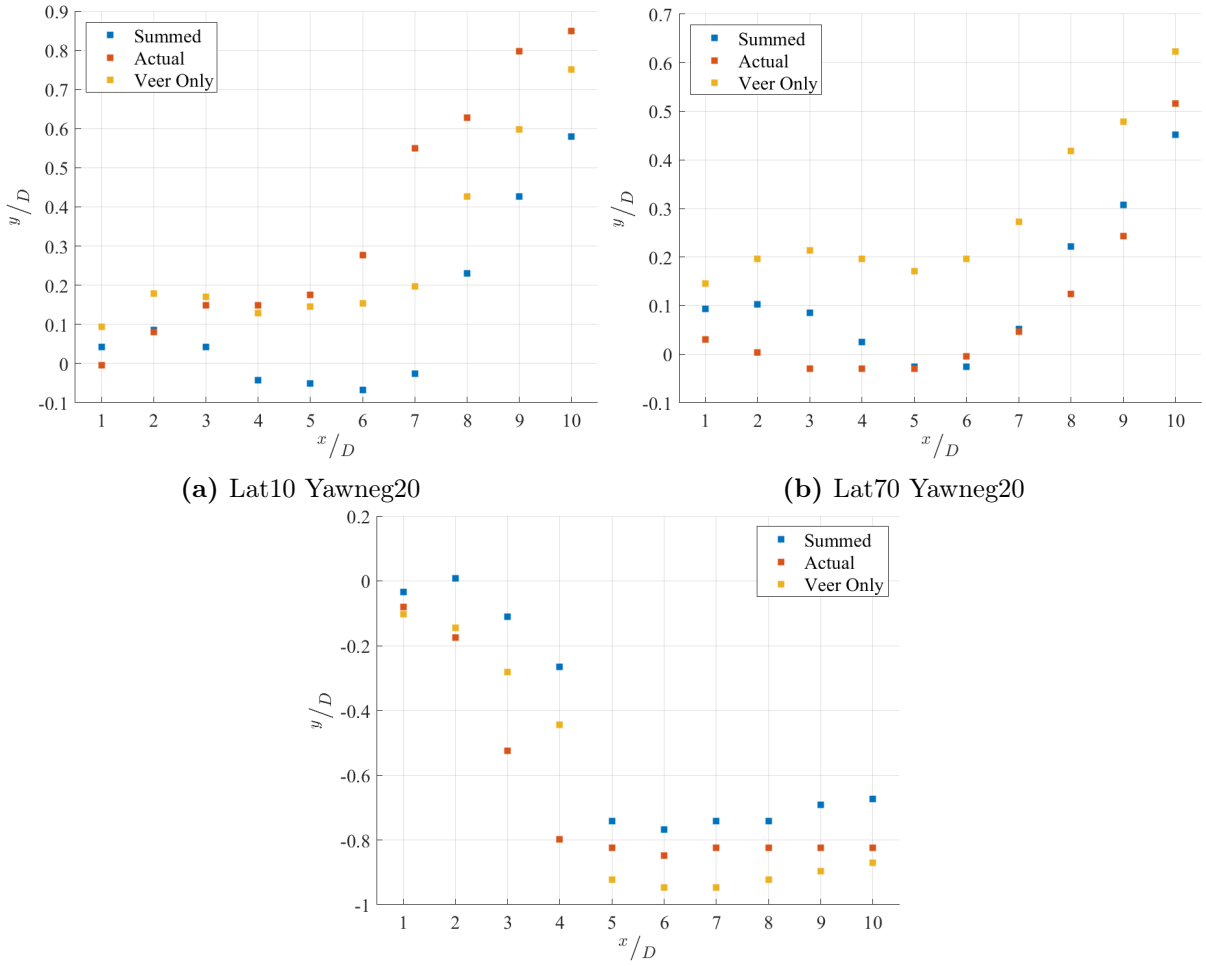

(a) Lat10 Yawneg20

(b) Lat70 Yawneg20

(c) Latneg40 Yaw20

Figure 4.27: Superimposed and actual wake centre location with downstream distance as viewed from above the turbine for various cases. The deflection due to veer is also included as a reference.

dominated by the deflection due to the wind veer. This may occur as the force applied on the flow by the yawed turbine does not act as effectively or uniformly when there is wind veer in the flow and the wind vector direction varies across the height of the rotor [106]. Thus, the same wake deflection achieved in non-veered flow for yawed turbines would not be achievable when wind veer is present. The relative angle between the horizontal wind vector and the turbine rotor plane also changes when yawing is applied, which could similarly contribute to the weakened effect of deflection due to yaw.

It is also possible that the wake skewing effect due to the wind veer has a greater impact on the wake centre location compared with the deflection achievable through yaw. The wind veer profiles describe significant changes in the horizontal wind vector angle over the turbine rotor area and the wake is notably skewed under the different veer conditions. Figure 4.28 presents the wake deflection observed for Lat0 Yaw20 alongside the deflections obtained for the positive latitudes when the turbine is un-yawed. From this Figure, it is shown that, without additional yawing, Lat10 and Lat70 achieve similar deflection as the

Lat0 Yaw20 case up to $7D$ downstream and after which both cases exceed the deflection due to yaw. While the Lat40 conditions result in greater wake deflection from $3D$ onward and so relative to yawing in non-veered flow, the influence of inflow veer on the wake appears to be more effective at wake deflection than yawing.

It is noted that some of the latitude and yaw combinations, give distinct results compared with the other cases that require a closer look at the wake behaviour in these conditions. These include Latneg40 Yawneg20, Lat70 Yaw20 and Latneg70 for all yaw angles. Ultimately, it appears the combination of the wake skew due to veer, wake rotation and generation of a vortex at the bottom of the yawed rotor result in these variations in the wake behaviour. A common feature across these specific cases is the lower wake region recovering faster than the other cases due to enhanced mixing with the freestream conditions. As previously outlined, the skew direction of the lower wake region dominates the wake centre location and so when its recovery is enhanced, the wake centre location via the minimum power method, is perceived to change. As the upper wake region for the $\pm 40^{\circ}$ and $\pm 70^{\circ}$ latitudes does not undergo much skewing, the maximum velocity deficit in the wake occurs closer to $y/D = 0$. So when the lower wake region has sufficiently recovered, the wake centre location is more likely to be calculated as the location of the maximum velocity deficit and thus return a lateral offset position close to $y/D = 0$. This interaction between inflow veer, wake rotation and lower wake region vortex is discussed further in Section 5.1, though further investigation into the specific dynamics is needed to fully understand how yawed wakes behave in the presence of wind veer.

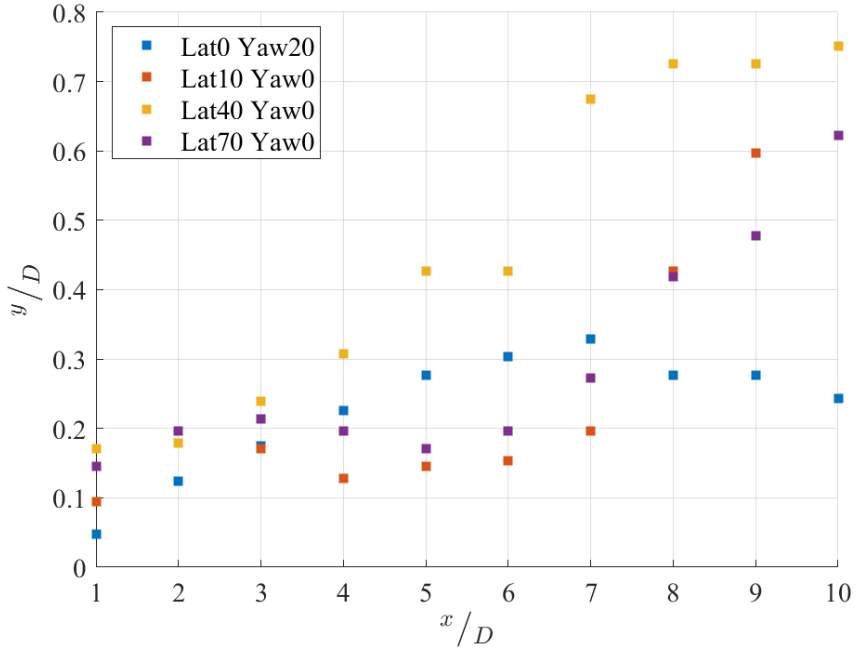

Figure 4.28: Wake deflection with downstream distance for Lat0 Yaw20 wake and the positive latitudes for the Yaw0 case.

4.6 Two Turbine Array

An array of two turbines, with the second turbine located $7D$ downstream, operating in veered and non-veered flow was simulated to observe how wind veer and wake steering influence the performance of an upstream and downstream, waked turbine. Table 4.1 and 4.2 present the power of the turbines in the array for the non-veered and veered flow conditions, respectively.

Table 4.1: Turbine power production for the Lat0 conditions.

	Power (kW)		
	Yaw 0°	Yaw 20°	Yaw -20°
Upstream turbine	1570	1410	1411
Downstream turbine	429	785	440
Total	2000	2195	1851

Table 4.2: Turbine power production for the Lat10 conditions.

	Power (kW)		
	Yaw 0°	Yaw 20°	Yaw -20°
Upstream turbine	1442	1305	1315
Downstream turbine	841	908	974
Total	2283	2213	2289

From Table 4.1, it is evident that applying a yaw angle of 20°resulted in an improvement in the net power produced by the turbine array, demonstrating the potential of wake steering in yielding an improvement in power production in non-veered flow. It is also shown that wake steering effectiveness is not symmetrical, as discussed in Section 2.1.4, with the application of a $-20°$ yaw angle resulting in a reduction in net power.

Whereas, when the flow conditions involve wind veer, applying a yaw angle of 20° to the upstream turbine resulted in an overall reduction in net power as shown in Table 4.2. While the downstream turbine under these conditions did experience an improvement in power production, the loss in power of the upstream turbine was not compensated. Instead a $-20°$ yaw of the upstream turbine yielded an increase in the total array power, albeit only a small increase.

Comparing the power produced by the upstream turbine reveals differences in the performance of turbines in veered and non-veered flow. In non-veered flow, an un-yawed turbine produces more power than if it were in veered flow. The downstream turbine exposed to the upstream wake also produces greater power when the inflow was veered compared with non-veered flow, which was similarly observed by Churchfield *et al.* [34].

This is likely due to the skew of the upstream wake, thinning the wake cross-sectional area and resulting in more favourable partial wake conditions on the downstream turbine. Whereas, in non-veered flow, the wake maintains a relatively circular shape and so, if the wake is not deflected using yaw, the downstream turbine is effectively entirely waked and only exposed to a velocity deficit.

The power of the turbines in the two turbine array was used to validate the power determined as per the wake centre location calculation. SOWFA calculates turbine power by summing the point-value powers at each actuator point and includes a coefficient of power, C_p, associated with the turbine model and blade design, as shown in Equation 2.1. Dividing the power values output by SOWFA by the values obtained per the wake centre location method for an un-yawed turbine at $7D$ downstream of the simulated turbine thus gives an approximation of the power coefficient for the turbine. These values are presented in Table 4.3, with an overall average value of 0.39, which is a reasonable value for the coefficient of power and is less than the Lanchester-Betz limit [10]. For reference, the peak coefficient of power for the NREL 5-MW turbine modelled in this study is 0.482 for uniform flow at 8 m/s [98]. The results in Table 4.3 indicate the numerical integration of power is producing a practical result.

Table 4.3: Coefficient of powers obtained from the numerical integration.

	Yaw 0°	Yaw 20°	Yaw −20°
Lat0	0.36	0.39	0.34
Lat10	0.41	0.43	0.40

4.7 Wake Model Comparison

The results from the high fidelity, SOWFA simulations are compared with various wake deflection and wake velocity deficit models that have been used in a number of wake steering controller tests. These models contain elements that have been derived analytically, based on the conservation of mass and momentum, as well as terms obtained from experimental analysis on wake behaviour. Analysing how effectively these wake models can represent the wake dynamics in veered flow would reveal how well equipped the current state of wake steering controllers are to operate in realistic, veered inflow conditions. To simplify the comparison and give an overall indication of how they hold up in veered flow, the wake models are mainly compared with the results for the Lat10 conditions.

4.7.1 Alternative Wake Deflection Method

The minimum power method for locating the centre of the wake varies from that used to develop the wake deflection models and so an alternative method for calculating the wake deflection is also tested to see how this difference in approach may influence the results. This is the geometric wake centre method, which determines the lateral extents of the wake as the points where the wake velocity at hub height is 95% of the freestream wind velocity and then finds the midpoint between these edges of the wake [13]. Under more ideal inflow wind conditions, such as those used to develop the wake deflection models, the wake behaves with Gaussian profiles describing properties such as the velocity deficit. The midpoint of the velocity deficit profile, where the velocity deficit would be maximum, is thus considered to be the wake centre.

The minimum power method was chosen for the main analysis of the wake deflection occurring due to veer and yaw as it does not make prior assumptions on the behaviour of the wake. It can capture the variations in wake shape and velocity deficit distribution that occurs when veer is present in the inflow wind for yawed turbines when computing the wake centre location. The geometric wake centre method, however, is more similar to the approaches used to develop the different wake deflection models. Thus, the results from applying the geometric wake centre method are included below to observe how well the wake models track the trajectory of the velocity deficit, as compared with the minimum power results, and the geometric wake centre.

4.7.2 Wake Deflection Models

The wake deflection models are first compared with the Lat0 wake deflections to gain an idea on how well the models represent wake steering under non-veered, but still SBL conditions. As the models have been developed for the far wake region behaviour, the comparison is also only performed from $4D$ downstream of the turbine. Figure 4.29 presents the wake deflection for each of the wake models and yaw angles. For both the Jiménez and Gaussian model, a yaw angle of 0° yields no deflection in the wake. The FLORIS model does account for deflection that is present in wakes from un-yawed turbines, though compared with the SOWFA results, it deviates from the simulated results from $8D$ downstream of the turbine.

For Yaw20, the models do reasonably well in depicting the wake deflection trend, particularly from $4D$ to $7D$, with FLORIS estimating the largest offset values and Jiménez estimating the smallest. The Gaussian model also appears to predict the wake centre location of the simulated wake sufficiently well from $4D$ to $7D$, with the SOWFA deflection values reducing in magnitude, while the Gaussian model increases.

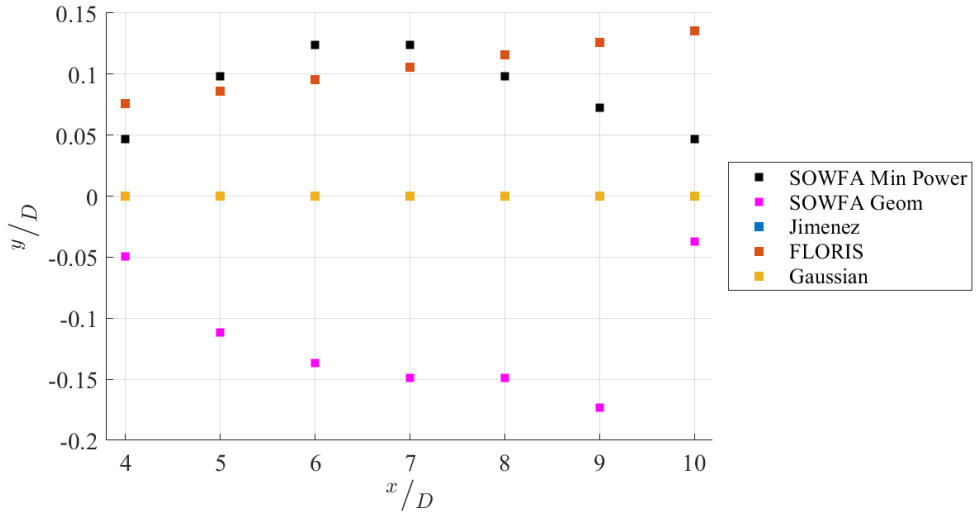

(a) Yaw0

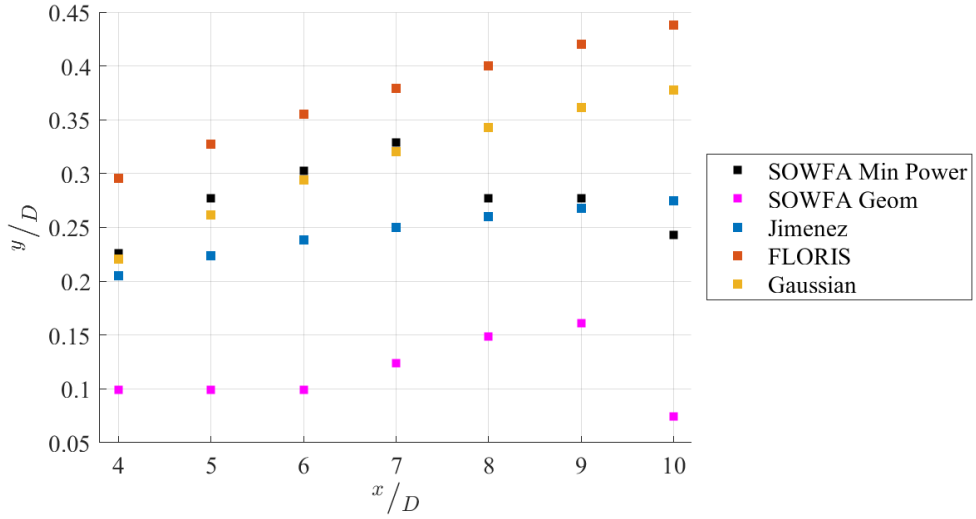

(b) Yaw20

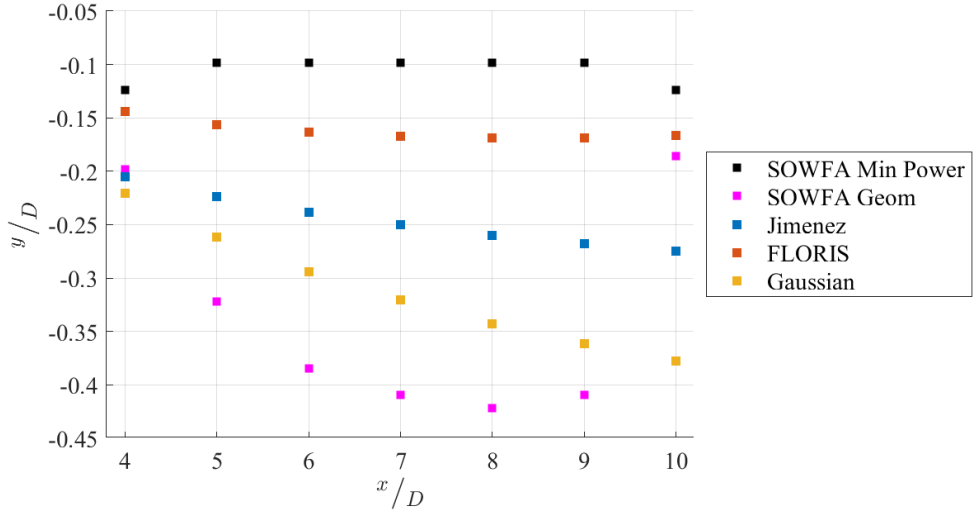

(c) Yawneg20

Figure 4.29: Wake deflection from SOWFA Lat0 results and wake models for each yaw angle. Note that the Jiménez and Gaussian models return the same zero wake deflection in (a).

For the Yawneg20 deflections, all three models overpredict the magnitude of the wake deflection. This is expected from the Gaussian and Jiménez models as neither accounts for the deflection occurring from a un-yawed turbine and assume positive and negative yaw angles to induce deflection of equal magnitude. Having captured this Yaw0 deflection, the FLORIS model slightly over-predicts the magnitude of the wake centre location in the negative direction, though the maximum difference across the downstream distances is only about $0.06D$.

The two methods used to determine the wake centre location in the SOWFA results for the non-veered cases produced differing results. For Yaw0, the geometric wake centre method yields a trend in the wake centre location in the opposite direction to the minimum power results and the wake models. For Yaw20 and Yawneg20, the returned results are in the same direction as the other methods, though the lateral offset values are noticeably different, with the Yaw20 offset values being much smaller and the Yawneg20 values being larger in magnitude. As shown in Section 4.2, the shape of the wake under both no yaw and yaw is asymmetric and the velocity deficit distribution is non-uniform. This would influence the geometric wake centre results as this method assumes a direct relationship between wake shape and wake centre, which explains the clear variation from the minimum power results.

To quantify how well each model represents the SOWFA results, the standard deviation of the profile from the simulation results is calculated to give an indication of which model represents the wake deflection best. Table 4.4 thus presents the standard deviation between the wake deflection generated by each model with that of the SOWFA simulations for Lat0 conditions and each yaw angle. Based on the results in Table 4.4, the FLORIS model is deemed to be the most effective of the three in modelling the wake deflection from the presented SOWFA results when the inflow is not veered, under the given conditions in this study, while the Gaussian and Jiménez models appear to capture the geometric wake centre best.

Table 4.4: Standard deviation of model wake deflections compared with the SOWFA results for Lat0 conditions. The smallest values for each yaw angle have been bolded and the values are normalised by the rotor diameter

	Minimum Power Method			Geometric Wake Centre Method		
	Yaw 0°	Yaw 20°	Yaw −20°	Yaw 0°	Yaw 20°	Yaw −20°
Jiménez	0.11	**0.049**	0.15	**0.13**	**0.14**	0.13
FLORIS	**0.059**	0.103	**0.053**	0.25	0.28	0.21
Gaussian	0.094	0.048	0.186	**0.13**	0.22	**0.10**

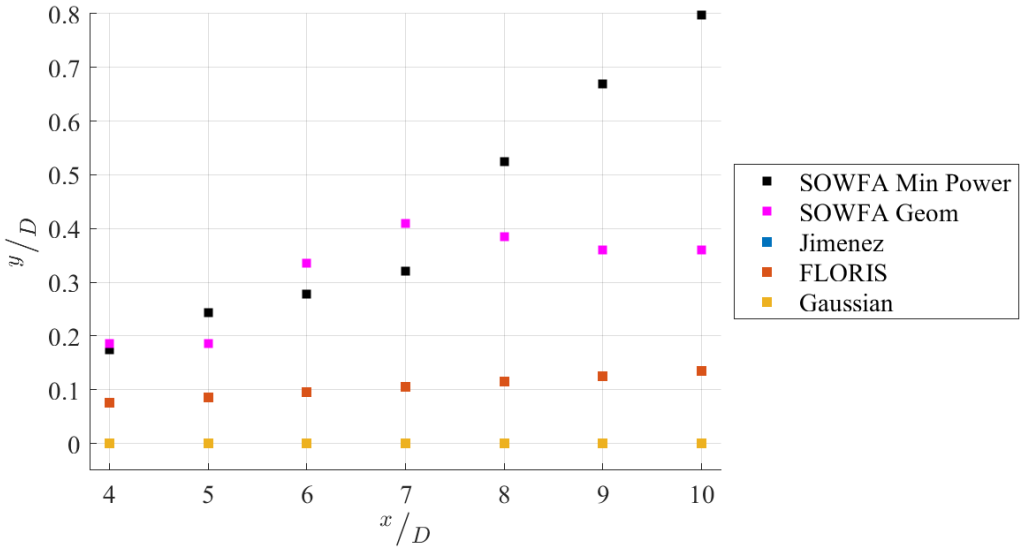

(a) Yaw0

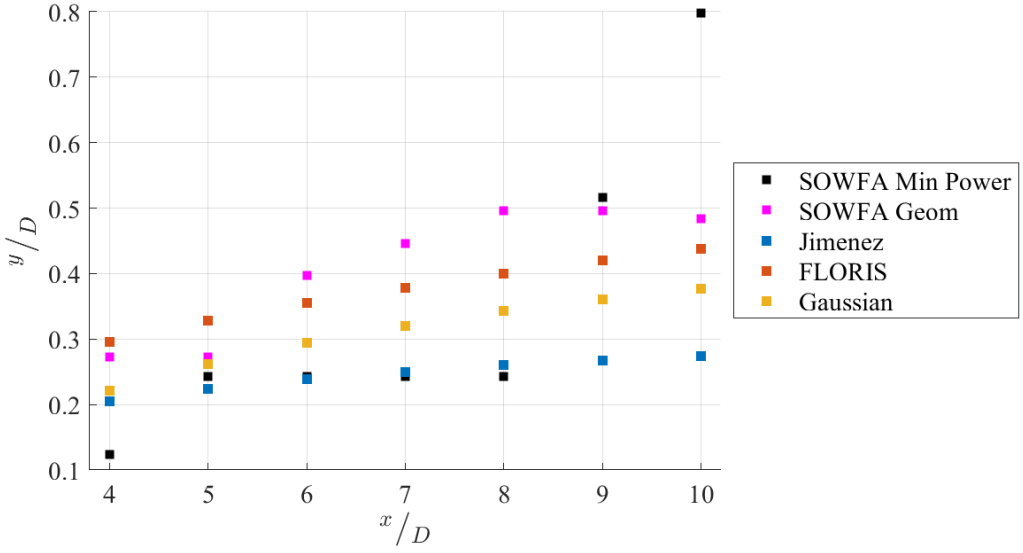

(b) Yaw20

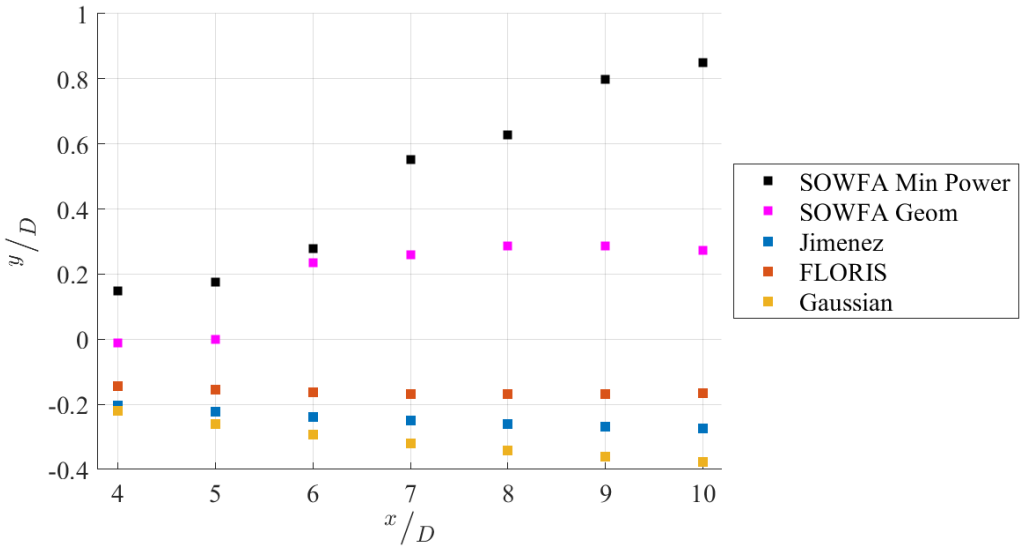

(c) Yawneg20

Figure 4.30: Wake deflection from SOWFA Lat10 results and wake models for each yaw angle. Note that the Jiménez and Gaussian models return the same zero wake deflection in (a).

Figure 4.30 then presents the wake deflection from both the SOWFA results and wake models for the Lat10 flow conditions. The wake deflection models do not incorporate any inflow data into the calculation of wake centre and so the same results are returned for Lat0 and Lat10. Thus when the wake deflection in Lat10 conditions vary substantially from the Lat0 conditions, the wake models cannot capture this change.

For Lat10 Yaw0, the wake models noticeably under-predict the wake deflection, returning values that differ by up to nearly $0.7D$. When Yaw20 is applied, the wake models are more effective, though this is driven by the deflection for Lat10 Yaw20 being quite similar to Lat0 Yaw20, at least up to a distance of $8D$ before the SOWFA minimum power calculated wake deflection increases rapidly. If the inflow veer caused the wake deflections to vary considerably from the Lat0 yawed conditions, the wake models would not capture this. The Lat10 Yawneg20 results are remarkably different from those predicted by the model, as the SOWFA wake deflections are heavily influenced by the wind veer and the comparative effect of yawing is minimal, thus deflection is maintained toward the positive, left side of the turbine and not the right as the models compute.

Under veered flow conditions, the minimum power method and geometric wake centre method produce results that are more similar to each other compared with those output for the non-veered flow. As presented earlier in this chapter, the wake behaviour is heavily influenced by the presence of inflow wind veer, with veer having a dominant effect on the wake shape and velocity deficit distribution overall and particularly relative to the effect of yawing. This dominance is likely why both wake centre calculation methods with the SOWFA results return similar results. Where the two methods do differ, is from $7D$ or further downstream, due to the recovery of the wake and lateral advection of the nacelle jet across the wake cross-section both influence the wake shape and velocity deficit distribution, accounting for the variation in wake centre trajectory between the two methods.

Table 4.5 presents the standard deviations between the model outputs and the Lat10 SOWFA results. Here it is demonstrated that the FLORIS model performed the best of the models relative to the simulated results for both the minimum power and geometric wake centre approaches, however the increase in standard deviations calculated compared with those in Table 4.4 is significant. Considering the discrepancies between model results and simulated results shown in Figure 4.30, none of the three models are particularly effective in representing wake deflection in veered flow in terms of velocity distribution or geometric centre.

It should also be noted that for negative latitudes, where the wake deflection is predominantly in the negative direction, the wake models are expected to perform poorly as they do not account for wind veer. This can be seen in Figure 4.31, which depicts both

Table 4.5: Standard deviation of model wake deflections compared with the SOWFA results for Lat10 conditions. The smallest values for each yaw angle have been bolded and the values are normalised by the rotor diameter

	Minimum Power Method			Geometric Wake Centre Method		
	Yaw 0°	Yaw 20°	Yaw −20°	Yaw 0°	Yaw 20°	Yaw −20°
Jiménez	0.53	0.25	0.85	0.35	0.19	0.50
FLORIS	**0.42**	**0.19**	**0.76**	**0.24**	**0.067**	**0.41**
Gaussian	0.53	0.20	0.93	0.35	0.12	0.57

the minimum power and geometric wake centre results for the Latneg10 Yaw20 conditions compared with the model results. As seen in this Figure, each of the models still assumes the deflection to be positive based on the 20° yaw angle and so inaccurately capture the effect of the negative latitude wind veer. Evidently, the absence of wind veer and its effect on wake behaviour results in the wake models under-performing in veered flow and would have detrimental implications for the effectiveness of wake steering controllers should these model results be relied upon when veer is present in the inflow.

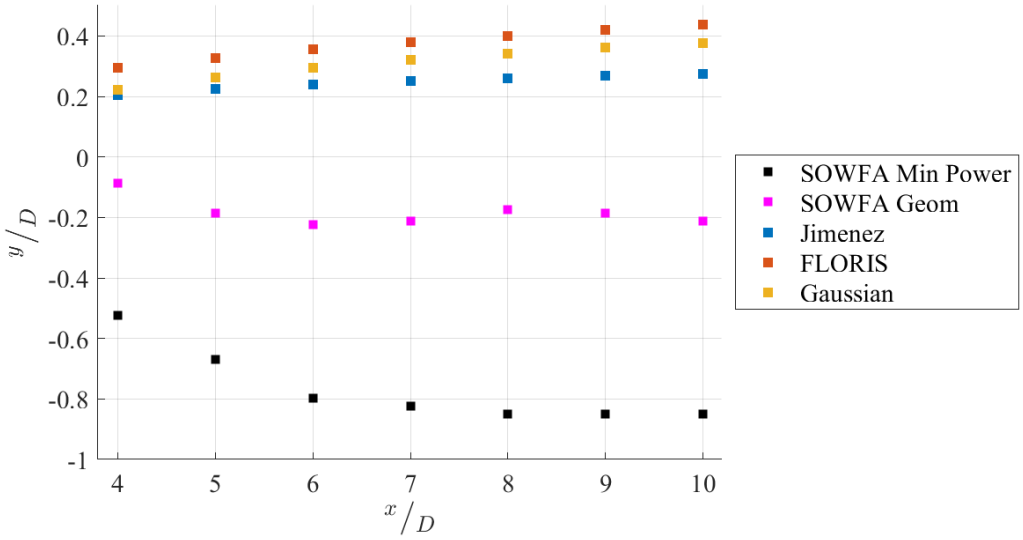

Figure 4.31: Wake deflection for SOWFA Latneg10 Yaw20 results and wake models for Yaw20 conditions.

4.7.3 Velocity Deficit Models

In terms of the velocity deficit models, the wake shape, maximum velocity deficit and velocity deficit distribution from the models are compared with the SOWFA results to analyse how the models represent the veered wake flow. Similar to the wake deflection models, the GCH and Abkar models were developed for the far wake only and so again, the comparison with the SOWFA results is made for $4D$ onward. The GCH model involves calculating the length of the near wake region, referred to as the 'potential core' length and this was found to be approximately $4D$ for both inflow cases. The freestream velocities

from the SOWFA simulations were used as in the inflow conditions for both the models.

Figures 4.32 and 4.33 present the streamwise velocity contours for both of the velocity deficit models and SOWFA results for Lat0 Yaw20 and Lat10 Yaw0 to visualise how the models capture yaw and veer separately.

Figure 4.32 depicts how the GCH model represents the lateral offset of the wake that occurs with yawing as seen in the SOWFA results for Lat0 Yaw20. The velocity deficit distribution for both models is a similar Gaussian profile, as expected since both models expand on the Gaussian velocity deficit model proposed by Bastankhah and Porté-Agel [39][40][80]. Neither model appears to capture the curl of the wake shape seen in the SOWFA results or the areas of wind velocity increase observed around the turbine. In terms of the Lat10 Yaw0 inflow conditions, shown in Figure 4.33, the Abkar model incorporates the profile of horizontal wind vector angle with height and so the diagonally skewed wake shape is thus represented. Whereas the GCH model, which does not include any veer term, appears the same as it did for the Lat0 Yaw20 inflow conditions, albeit not deflected laterally.

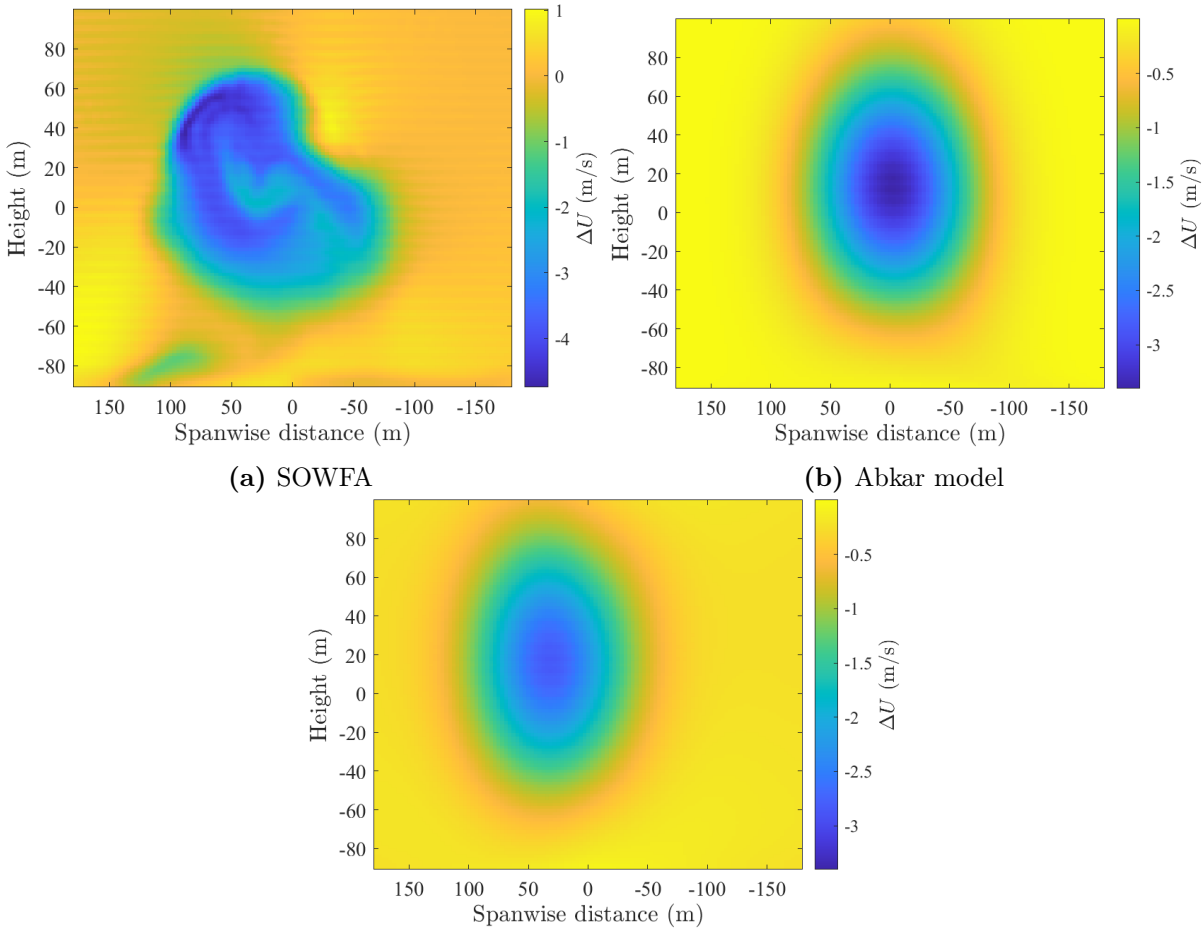

(a) SOWFA

(b) Abkar model

(c) GCH model

Figure 4.32: Streamwise velocity deficit as viewed from upstream at $5D$ for the SOWFA results, Abkar model and GCH model with Lat0 Yaw20 conditions.

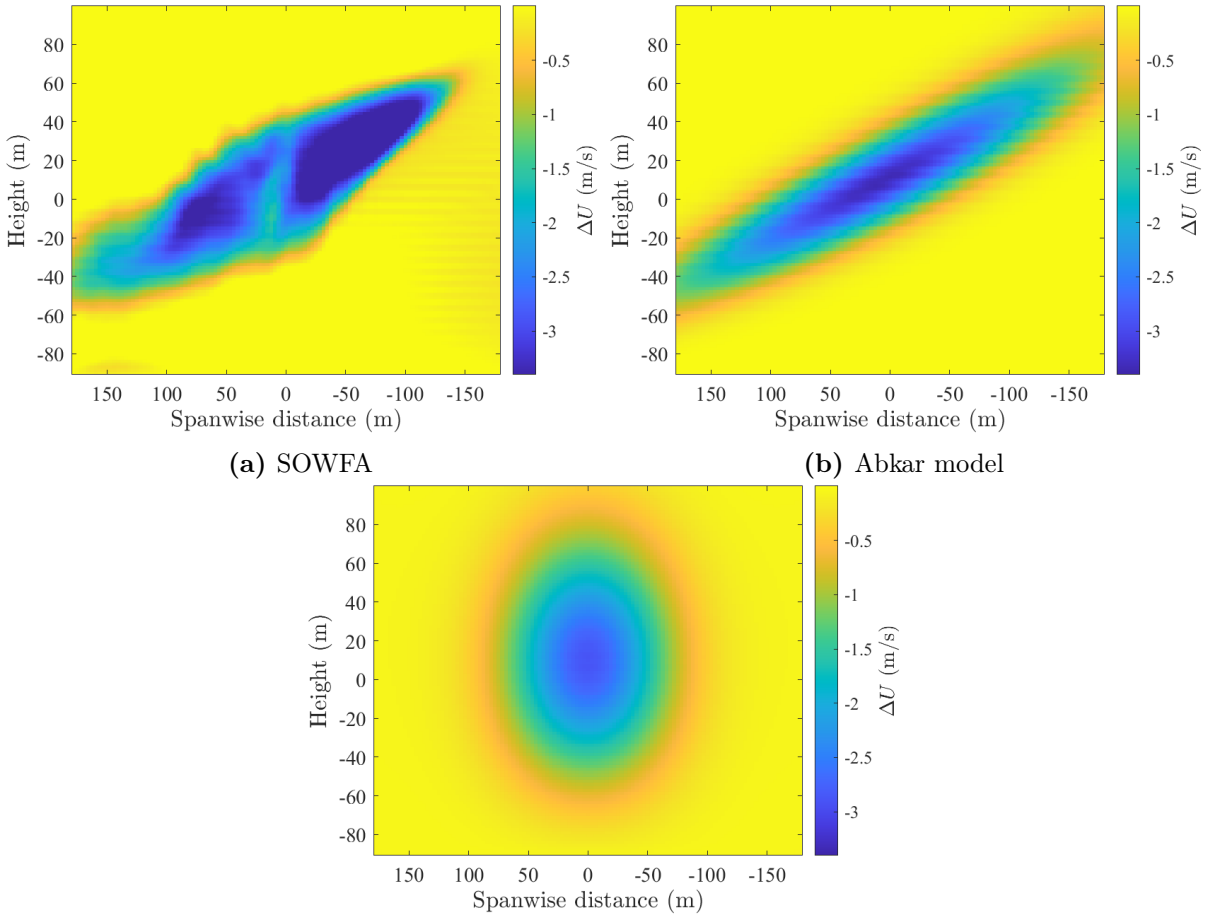

(a) SOWFA **(b)** Abkar model

(c) GCH model

Figure 4.33: Streamwise velocity deficit as viewed from upstream at $5D$ for the SOWFA results, Abkar model and GCH model for Lat10 Yaw0 conditions.

To compare the shapes of the wakes produced by the models, the same approach was taken as in Section 4.2, and the outline of the modelled wakes were overlaid with the SOWFA results. Figures 4.32 and 4.33 already indicate that the GCH model will not produce a skewed wake, which is clearly demonstrated in Figure 4.34, and the absence of a yawing term in the Abkar model means the modelled wake does not change with applied yaw angle. Thus the GCH model wake shape is only compared with the Lat0 conditions to demonstrate how the model depicts the change in wake shape due to yaw in Figure 4.35. While the Abkar model is compared with the Lat10 inflow conditions for each yaw angle to highlight any changes in the wake shape due to yawing that are missed by the model in Figure 4.36.

As shown in Figure 4.35, the GCH model predicts a more circular shaped wake compared with the irregular, curled shape generated by SOWFA. The GCH model computes the wake shape to be larger in the vertical direction relative to the SOWFA results. The lateral offset of the wake due to yawing is captured quite well, with the position and horizontal width of the wake being quite similar between the GCH model and the SOWFA results.

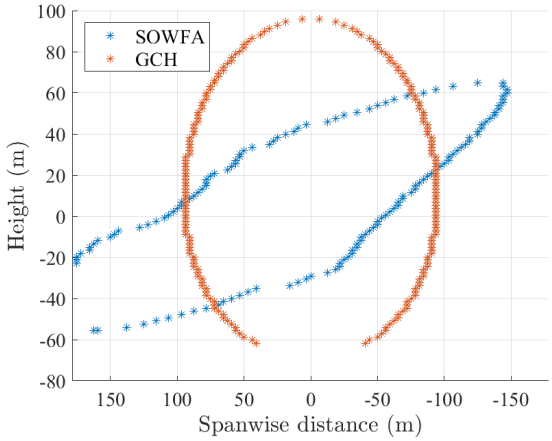

Figure 4.34: Wake shape for GCH model compared with the SOWFA results for Lat10 Yaw0.

The Abkar model appears to represent the skew of the wake in veered flow conditions very well, as shown in Figure 4.36, though it does compute a slightly larger wake with the Abkar results shown to extend beyond the refined region of the domain while the SOWFA results do not. The curvature of the wake that occurs due to yawing is evident in the SOWFA wake shape for Yaw20 and Yawneg20 and it thus demonstrated how the absence of a yawing term in the Abkar model means variations in the flow are not resolved.

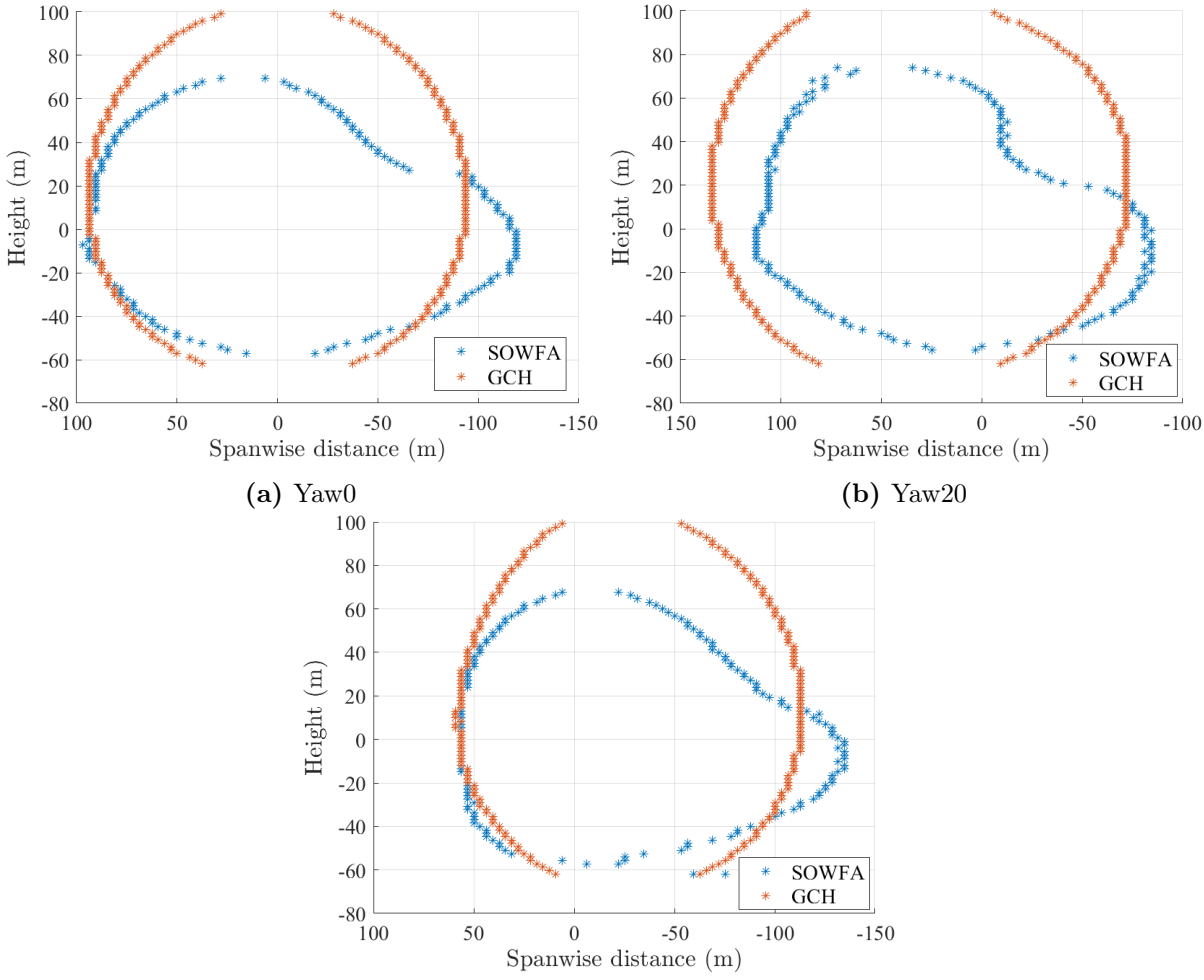

(a) Yaw0

(b) Yaw20

(c) Yawneg20

Figure 4.35: Wake shape comparison between the GCH model and SOWFA for Lat0 conditions and each yaw angle.

The maximum velocity deficit with downstream distance for each model was measured to show how the models depict the wake recovery rate. Figure 4.37 depicts this for

un-yawed turbine in Lat0 and Lat10 conditions for both the models and SOWFA, while Figure 4.38 depicts the GCH model under Lat0 conditions for the different yaw angles relative to the simulation results.

Both the models under-predict the velocity deficit for non-veered and veered flow, though this difference is greatest for Lat0 conditions as shown in Figure 4.37. As the inflow velocities vary between Lat0 and Lat10 flow, the models return slightly different maximum velocity deficit values between the two conditions, though not to the same extent as demonstrated by the SOWFA results.

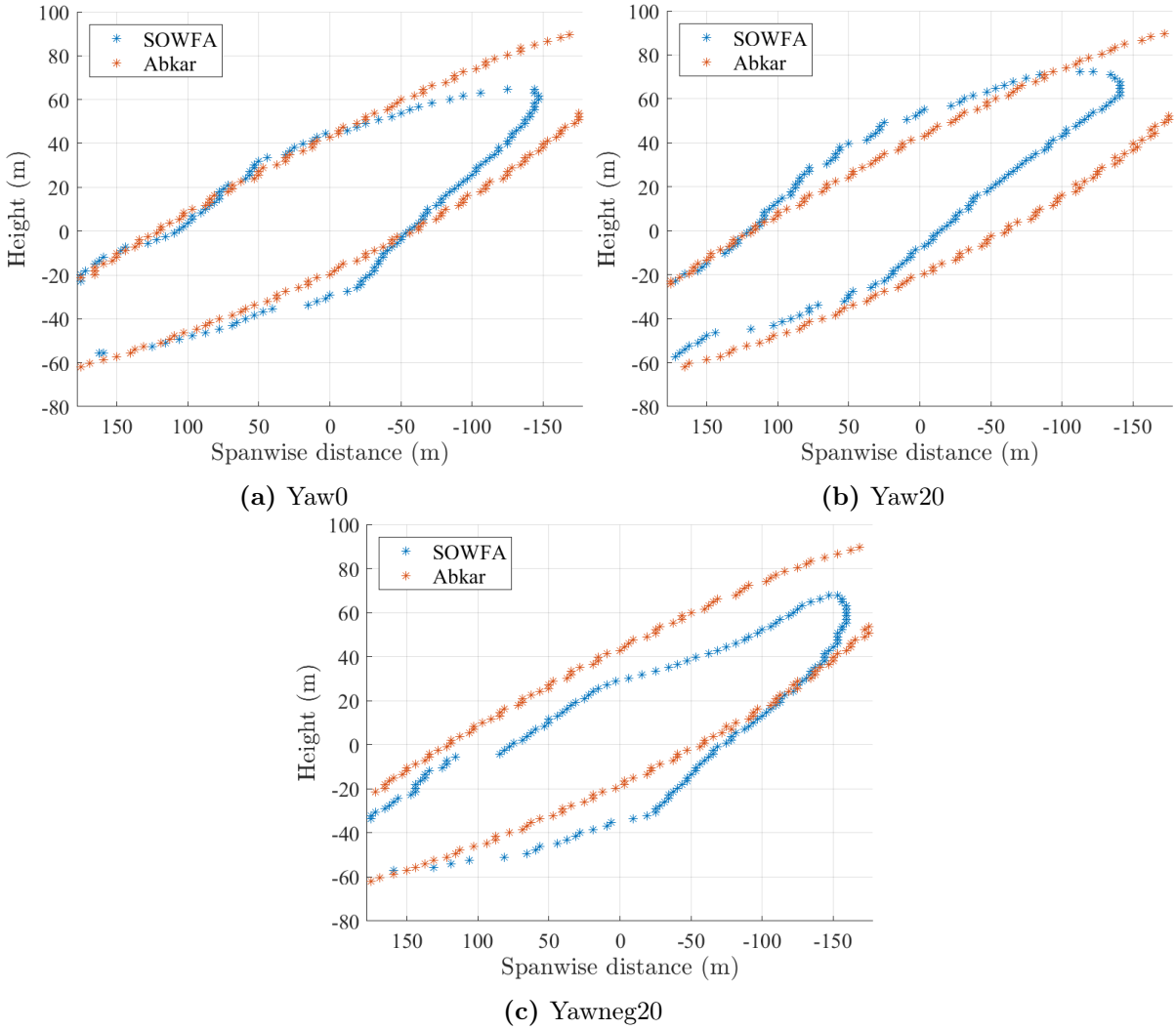

(a) Yaw0

(b) Yaw20

(c) Yawneg20

Figure 4.36: Wake shape comparison between the Abkar model and SOWFA for Lat10 conditions and each yaw angle.

The GCH model does account for some additional wake recovery due to yawing and so the maximum streamwise velocity deficits at each distance downstream vary with the yaw angle, as shown in Figure 4.38. Compared with the SOWFA results, the difference in maximum deficit between each yaw angle is smaller than that observed in the simulations. SOWFA recorded the Yaw20 wake to have the smallest maximum deficit, followed by

Yawneg20 and then Yaw0 to give the largest streamwise velocity deficit in the wake. The variation in deficit between the yaw angles also increases with downstream distance, reflecting how recovery is enhanced in yawed wakes. The GCH model captures this too, though it returns the Yaw20 case as having the largest deficit and Yawneg20, the smallest.

Given neither of the two models capture the impact of both veer and yaw on wake behaviour, an effective approach to modelling wakes in veered flow could be to combine the strengths of the two models to predict the skewed and deflected wakes observed in the SOWFA results. In addition, there are aspects of each model that could be improved to better represent the wake behaviour in veered and SBL flow.

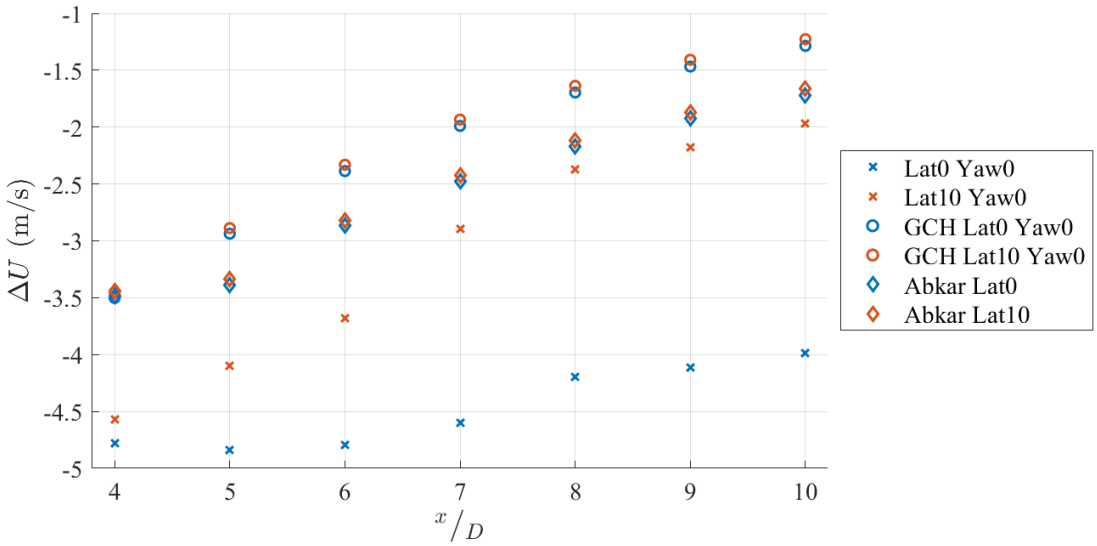

Figure 4.37: Maximum velocity deficit with downstream distance for the GCH model, Abkar model and SOWFA results for an un-yawed turbine in Lat0 and Lat10 conditions.

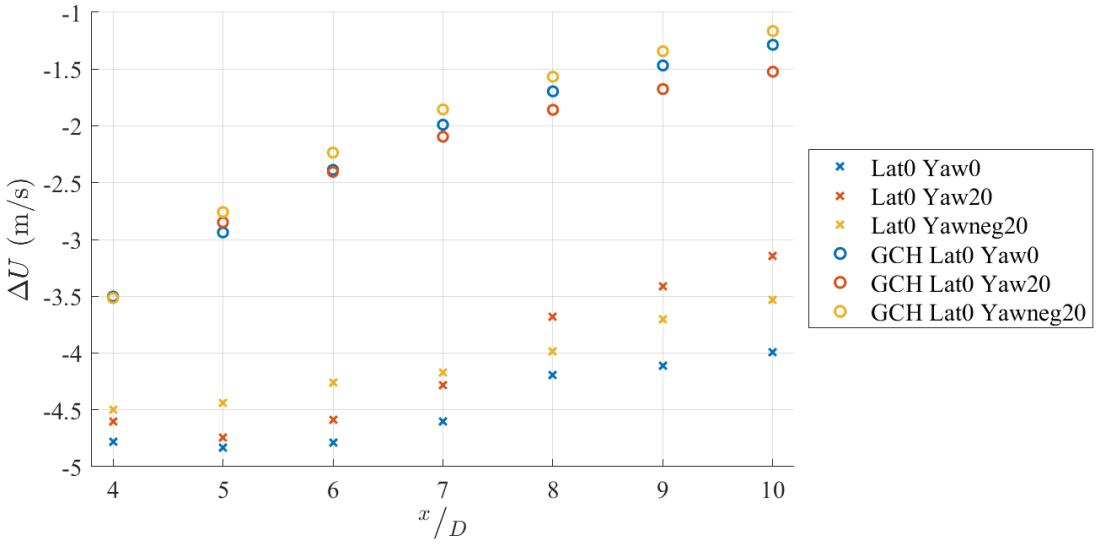

Figure 4.38: Maximum velocity deficit with downstream distance for the GCH model and SOWFA results for Lat0 conditions and various yaw angles.

5. Discussion

The following discussion centres around the following two key questions at the core of this research:

- How can wake models be modified to better represent wakes generated in realistic, veered conditions?
- What are the implications for wake steering in wind flows with various wind veers?

The discussion surrounding the first question delves into how the wake behaviour varied in veered flow and how these observations could be incorporated into wake models. Most wake models utilised by wake steering controllers do not account for both veer and yawing and thus must be modified to better reflect the wake dynamics in veered flow. The second question then considers what the veered wake behaviour and the output of the current wake models for the varied inflow conditions means in the context of wake steering control for wind farms operating in veered flow.

5.1 Modelling Wake Responses in Veered Flow

Modelling wind turbines is the most accessible and controllable method to analyse turbine performance and wake dynamics. Wake models are also a critical component of wake steering controllers as the optimal yaw angles for the given inflow are generally calculated based on the results of models. The presence of wind veer across the turbine rotor significantly affects the behaviour of the wake and available power for any downstream wind turbines. A number of wake models were compared with the SOWFA simulations to observe their effectiveness at representing a wake produced in veered flow. Similarly, the SOWFA requires turbine modelling using the actuator line method (ALM), so while higher in fidelity than the parametric wake models, the simulation results also involved a representation of the turbine wake dynamics.

Previous investigations into wakes in veered inflow have focused on the skew of the wake shape due to veer [33][34][37], changes to the wake trajectory at different heights [35][78] and the observed wake veer compared with the inflow veer profile [33][34]. However, there has been little to no analysis on how the wakes of yawed turbines respond when the inflow involves wind veer. As demonstrated in Chapter 4, the presence of wind veer affected the wake shape, its recovery, the veer exhibited by the wake and the deflection of the wake centre. The two turbine simulation in veered and non-veered inflow also revealed

the power production and effectiveness of wake steering to be influenced by wind veer. These variations in wake behaviour are not well captured by currently used wake models in wake steering controller development and so adjustments to the models is necessary to better replicate the dynamics of wakes undergoing veer and yaw.

In addition to the effect of veer on the wake behaviour, the freestream wind conditions change with the latitude. The velocity profiles for the streamwise direction differ in magnitude between the latitude cases, which would contribute to differences in the wake recovery, wake deflection due to yaw and velocity deficit. Figure 5.1 presents the streamwise velocity vertical profile for Lat0 and the positive latitude cases, noting that the negative latitude cases presented near identical profiles to their positive magnitude counterparts. It is shown in Figure 5.1, that below hub height, increasing the latitude results in faster

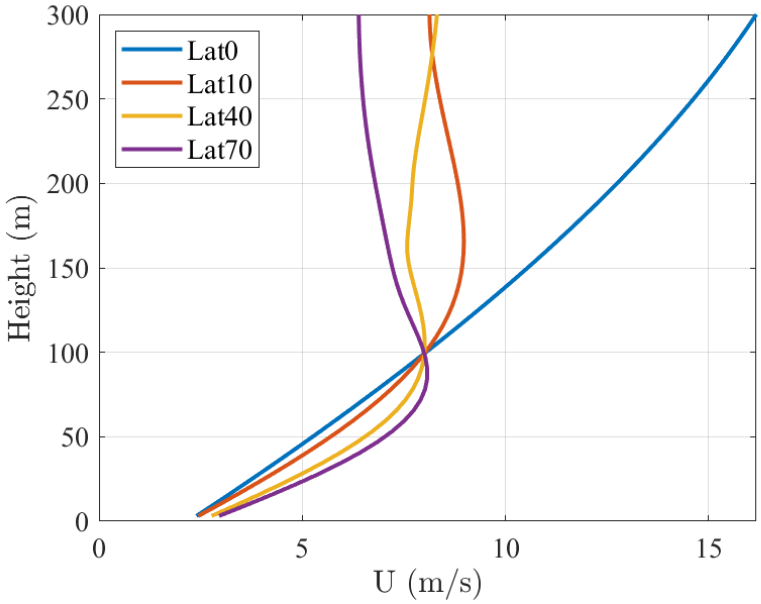

Figure 5.1: Freestream streamwise velocity profile with height for the positive latitude conditions

streamwise velocities, with Lat70 conditions presenting the fastest streamwise component wind speeds and Lat0 presenting the slowest. The streamwise velocity profile trend below hub height in the Lat0, Lat10 and Lat40 cases is similar, with a maximum difference in velocity magnitude of approximately 1 m/s occurring at 20 m below hub height between the Lat40 and Lat0 flows. Above hub height, the velocity profiles differ noticeably, with the Lat0 conditions increasing in wind speed, while the non-zero latitudes appear to settle on constant wind speeds. The Lat70 profile reaches its maximum speed of approximately 8 m/s at hub height and the speed of the wind flow is then shown to decrease with increasing height above hub height.

This variation in freestream velocity magnitudes would affect the wake deflection achieved when the turbine is in yaw. As the deflection due to yaw is proportional to the

velocity vector perpendicular to the rotor, should the magnitude of this vector vary across the turbine height [13], so would the deflection force imparted on the flow. This could explain why in veered flow cases, the deflection of the wake is dominated by the wind veer and the effect of yawing on the deflection is minimal, as alluded to in Section 4.5.3. Thus, as the analysis on the superimposition of deflection due to veer and yaw suggests, modelling the deflection of wakes produced in veered inflow cannot involve just adding together the deflections due to both sources and requires consideration of how the wind veer profile, applied yaw angle and inflow wind conditions interact to yield wake deflection.

The spanwise velocity profiles, in terms of shape and magnitude were also observed to differ between the latitude cases. This could be at the root of why the behaviour of the lower wake region for the yawed turbines differs between the latitude cases even though the magnitude of the horizontal wind vector angles in this region is quite similar for the veering cases. Figure 5.2 demonstrates the vertical profile of the spanwise velocity in the inflow wind conditions for Lat0 and the positive latitudes. The Lat70 profile involves a spanwise velocity of nearly double that of the Lat10 profile in the region below hub height and particularly near the bottom of the rotor.

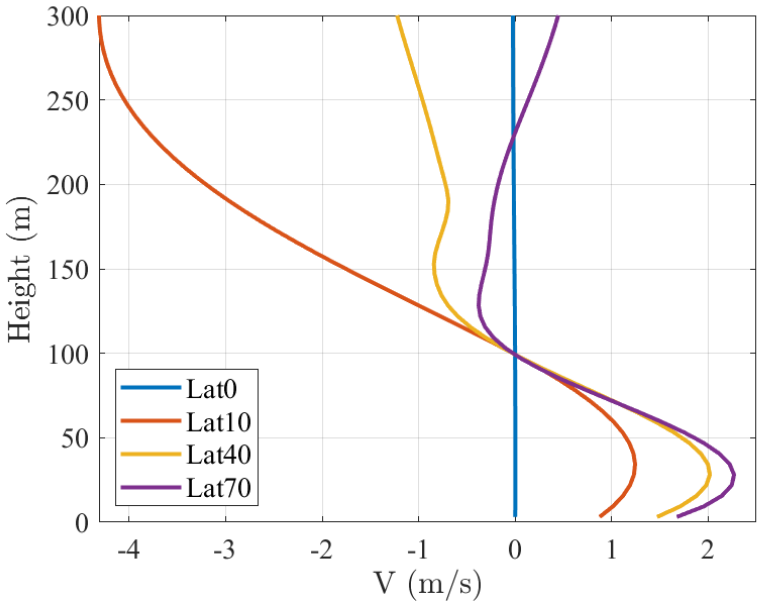

Figure 5.2: Freestream spanwise velocity profile with height for the positive latitude conditions

It is theorised that the interaction between the spanwise velocity due to the inflow veer and the vortex at the bottom of the yawed rotor results in the behaviour differences between yaw cases of the same latitude. Yawed turbines exhibit a pair of counter-rotating vortices (CRVs) at the top and bottom of the rotor. The deflection of the wake is observed to be significantly influenced by the direction of skew of the wake region below hub height, as highlighted in Section 4.5.2. As the spanwise velocity profiles for the different latitudes

vary, as demonstrated in Figure 5.2, this likely causes the deviation in wake behaviour between cases of the same yaw angle under differing veered inflow conditions. For the Lat70 case, the deflections measured for Yaw20 and Yawneg20 differed greatly up to approximately $9D$ downstream. Figure 5.3 presents a top down view of the hub height streamwise velocity and wake deflection for both yaw angles in Lat70 flow, while Figure 5.4 depicts the streamwise velocity deficits as viewed from upstream at $5D$ and $9D$.

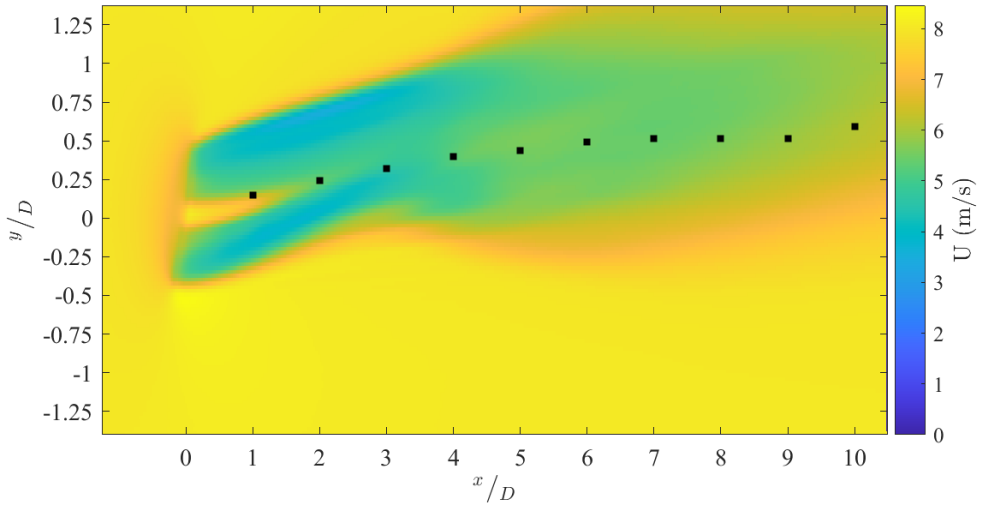

(a) Lat70 Yaw20

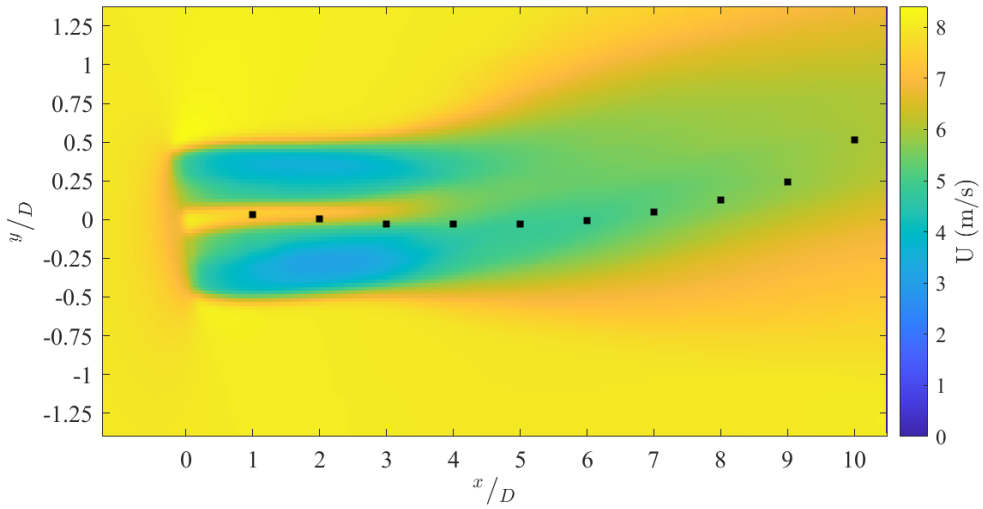

(b) Lat70 Yawneg20

Figure 5.3: Top-down view of the streamwise velocity for Lat70 Yaw20 (top) and Lat70 Yawneg20 (bottom). The wake deflection with downstream distance is shown by the black squares

As shown in Figure 5.4, the Yaw20 wake appears to curl more downward, with the cross-sectional shape exhibiting some downward concavity. Whereas, the Yawneg20 is curled up, exhibiting upward concavity in the cross-sectional wake shape. There is also a noticeable difference in the recovery of the lower wake region, with the Yaw20 wake experiencing greater recovery below hub height than observed in the Yawneg20 wake.

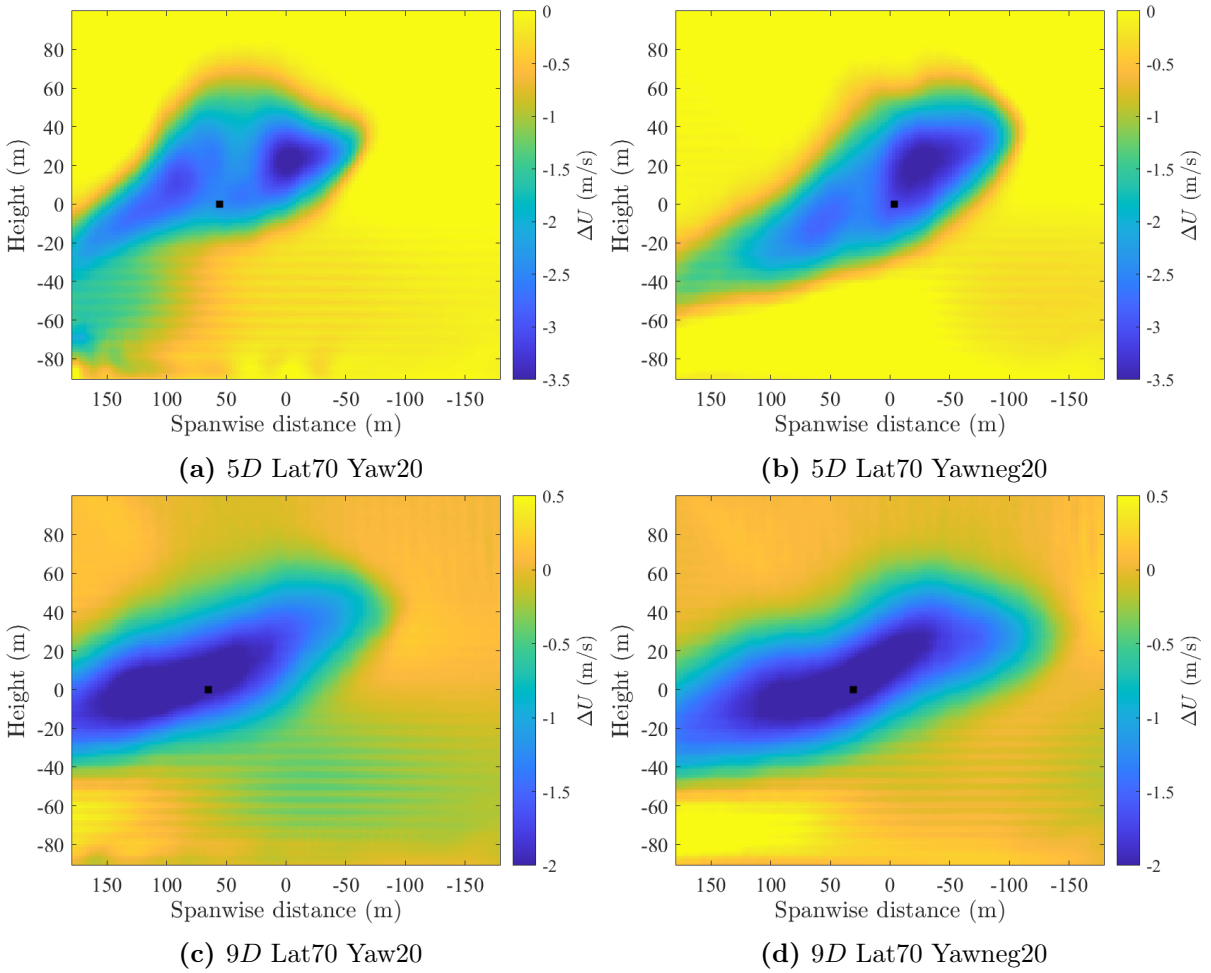

(a) 5D Lat70 Yaw20 **(b)** 5D Lat70 Yawneg20

(c) 9D Lat70 Yaw20 **(d)** 9D Lat70 Yawneg20

Figure 5.4: Streamwise velocity deficit as viewed from upstream for Lat70 Yaw20 (left) and Lat70 Yawneg20 (right) at 5D and 9D downstream. The black square indicates the wake centre

Comparing this with the Lat10 case, the wakes from Yaw20 and Yawneg20 behaved similarly, recording the same trend toward the positive direction for wake deflection. The shapes of the wake were seen to differ slightly in direction of its curvature, though the recovery of the lower wake region with downstream distance remained very similar between both yaw angles. Applying a 20° yaw angle in Lat70 flow resulted in enhanced wake deflection toward the positive direction relative to the un-yawed deflection. Whereas in Lat10 flow, the wake deflection was approximately the same, if not less, for Yaw20. Again, a distinction is observed between the recovery of the lower wake region for the Lat10 Yaw20 case and the Lat70 Yaw20 case, with the latter exhibiting enhanced mixing with the freestream flow up to about 9D. This difference in recovery of the lower wake is likely driving the dissimilarities in flow behaviour between wakes from the same yaw angle, but different latitudes.

A difference in wake behaviour was also observed between the positive and negative latitudes. The Lat40 Yaw20 and Latneg40 Yawneg20 cases would be expected to perform as mirror opposites, however the deflection as shown in Figure 5.5, wake shape and recovery

of the lower wake region, both shown in Figure 5.6, differed between the two. The wake rotation for all simulations was counter-clockwise and so variations in the wakes generated in these mirrored cases is likely due to the the rotation of the wake interacting with the veer and CRV at the bottom of the wake.

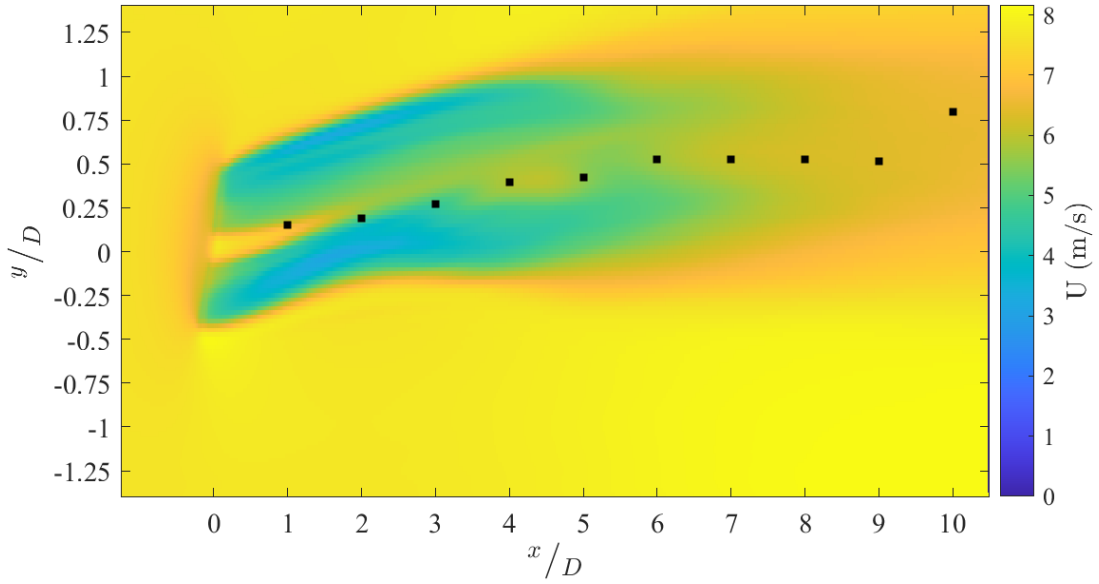

(a) Lat40 Yaw20

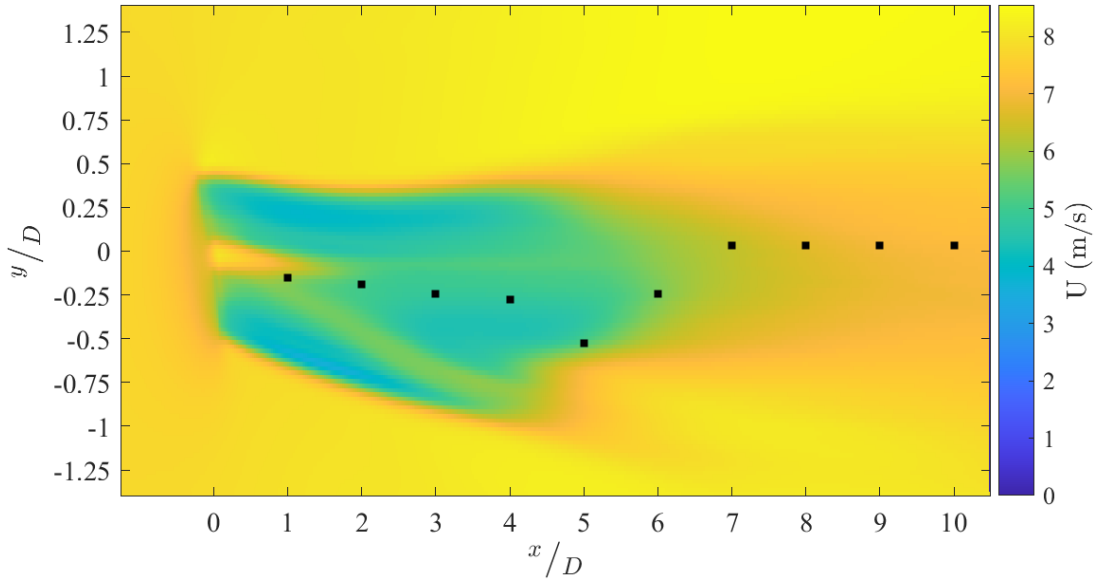

(b) Latneg40 Yawneg20

Figure 5.5: Top-down view of the streamwise velocity for Lat40 Yaw20 (top) and Latneg40 Yawneg20 (bottom). The wake deflection with downstream distance is shown by the black squares

The effect of the SBL freestream flow on wake behaviour was outlined in Section 2.2.2, in which it was discussed that wake recovery is slower and wake deflection more distinct in the SBL compared with the NBL and CBL. Both the velocity deficit models were developed based on the Gaussian velocity deficit model proposed by Bastankhah and Porté-Agel [39], which was derived from an analysis on wind tunnel measurements of wakes in a neutrally

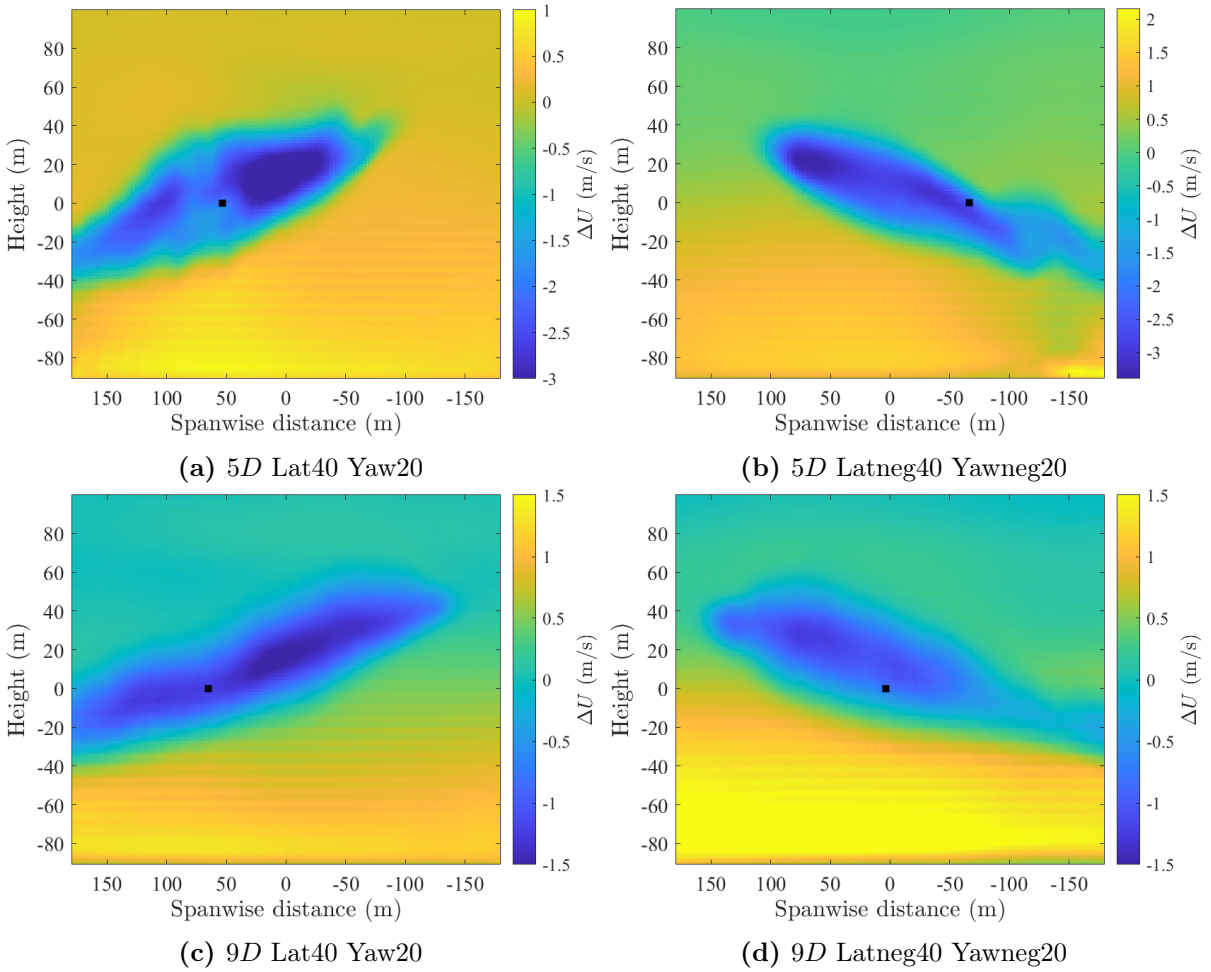

(a) 5D Lat40 Yaw20

(b) 5D Latneg40 Yawneg20

(c) 9D Lat40 Yaw20

(d) 9D Latneg40 Yawneg20

Figure 5.6: Streamwise velocity deficit as viewed from upstream for Lat40 Yaw20 (left) and Latneg40 Yawneg20 (right) at 5D and 9D downstream. The black square indicates the wake centre

stratified boundary layer (NBL). Vollmer *et al.* [28] observed wakes generated in the SBL to have higher velocity deficits and a thinner shear layer between the core of the wake and the freestream flow compared with wakes produced in the NBL. Thus, the variation in velocity deficit distributions between the models and SOWFA results is perhaps due to the model derivation from NBL flow conditions.

This difference was similarly observed when comparing the velocity deficit distribution from the SOWFA results with those produced by the velocity deficit models, as shown in Figures 4.32 and 4.33. The SOWFA results depicted a more top-hat like distribution of the velocity deficit in the wake, with high velocity deficit occurring over a large proportion of the wake cross-section and a sharp transition from this high deficit region to the freestream flow along the wake edges. Whereas, the models output a more regular Gaussian distribution for the velocity deficit. This difference in velocity deficit distribution would likely lead to the models under-predicting the power losses associated with downstream turbines operating in both fully waked and partially waked flow conditions. If wake steering was

then implemented based on the model outputs for turbines operating in SBL flow, it would likely lead to the wind farm or turbine array performing sub-optimally or yield greater losses in power.

The deflection models demonstrated sufficient capacity to reflect the wake behaviour in non-veered, but yawed turbine flow conditions. However, when the inflow was veered, the model results did not account for the effect of wind veer on the wake behaviour. This is to be expected as the models only consider a geometric centre of the wake and are based on more simple wake shapes, not accounting for the variation in wake behaviour caused by the presence of wind veer. Both the FLORIS and Gaussian models assume a self-similar profile for the velocity deficit and skew angle with downstream distance [11][39], while the Jiménez model assumed a top-hat velocity deficit with the profile mid-point considered to be the wake centre [13]. The behaviour of yawed wakes in veered flow differed significantly from these assumptions, with regions of the wakes recovering at different rates, the wake expanding in varying directions with height and influence of the inflow veer and stratified velocity profile on the propagation of the velocity deficit downstream.

Two methods of calculating the wake centre were applied when comparing how well the models capture the wake deflection. The minimum power method provides insight into the trajectory of and changes in the velocity distribution across the wake cross-section, while the geometric centre method locations the centre of the wake shape. Should the wake behave in an ideal manner, with Gaussian profiles describing the velocity deficit in the wake, the wake deflection from both methods is expected to be approximately the same [13]. However, the wake behaviour observed does not match the ideal scenario and the two methods returned different wake trajectories. This demonstrates how veer and yaw, via the influence on the wake recovery, wake shape and velocity distribution, leads to a variation in the geometric wake centre deflection relative to how the available power in the wake deflects.

Analysing whether the deflections due to veer and yaw superimpose demonstrated that this is not the case. So, modifying the deflection models to account for the effect of wind veer cannot simply involve adding an additional offset term in the deflection calculation. Further research is thus needed to parameterise the relationship between the inflow veer profile and wake centre as it appears to be coupled with the recovery and skew of the cross-sectional wake velocity deficit.

The domain and extents of the refined region for the SOWFA simulations required setting prior to running the simulations. This was thus done before the trajectory of the full wake cross-section was known. The size of the refined region was also limited as increasing the width of the region significantly increased the computational time and resource required to obtain results. Similarly, it was then not feasible to repeat the

simulations with a modified refined region due to the computational requirements.

Thus, the boundaries of the refined region are at ±175 m for all simulations. As a result, at some downstream distances, areas of the wake were observed to deflect or skew out of this region of analysis. This likely would have an influence on the results, particularly for the wake deflection and the wake veer trends.

The wake centre location calculation was limited to the refined region with the range of lateral offsets for the theoretical downstream turbine set such that the entire rotor of the theoretical turbine would be within the refined region. Therefore, the maximum wake centre offset distance was limited to ±0.8492. This value was observed from some pairings of veer and yaw, including Latneg40 Yaw0 from 5D downstream and Latneg10 Yaw20 from 7D downstream, which demonstrated a plateau in the wake centre location at ±0.8492. These results can be viewed as the wake centre deflecting beyond the refined region limits and while the exact location of the wake centre is not determined, the direction of the wake trajectory and an idea of the deflection magnitude is provided. The majority of the wake remained within the refined region for all simulations up to 10D downstream, with only the edges of the wake observed to extend out of view. Thus, for the wake veer results, the general trend of the veer in the wake is effectively captured for most of the wake cross-section.

However, given the complex dynamics of the wake in terms of recovery, rotation and presence of a counter-rotating vortex pair in the wake, the full wake should ideally be analysed to confirm the trends and behaviours observed in this thesis. Therefore, future computational investigations in to wakes produced from veered inflow and as a result of yaw should thus consider the trajectory of the full wake cross-section, using the results of this thesis as a gauge. This would improve the observations and analysis of the wake behaviour and further validate the results presented in this thesis.

Notably, the power results of the two turbine array are not affected by the extents of the refined region as the power is calculated over the area of the rotors, both of which are entirely encased within the region of analysis. These results highlighted the disparity between the production of a turbine array undergoing wake steering and the individual turbines in the array when the inflow wind involves veer and when it does not. These results are significant in demonstrating how the effectiveness of wake steering is susceptible to the nature of the inflow wind conditions. The results also demonstrate that applying the same control logic for the yaw angle in varying inflow conditions is not a suitable approach for optimal power production and consideration of the inflow wind conditions must be incorporated into the control logic of wake steering controllers.

The current version of the ALM implementation in the SOWFA code does not include

the presence of the nacelle or tower and so the effect of both these features on the flow is not represented by the results. The higher velocity region observed in the centre of the wake due the absence of the nacelle appears to have contributed to the irregular shape of the wake, as shown in Figures 4.3 and 4.4. In wakes generated by actual turbines in real flow, a vortex is observed to shed from the hub of the turbine [10][107]. Zong and Porté-Agel [107] report the velocity deficit due to the presence of the hub is "quickly smeared out" over a short downstream distance due to wake rotation and turbulent diffusion. There is also some freestream flow over the nacelle that is not affected by the turbine blades and so some higher speed velocity flow observed in the wake surrounding the nacelle wake [105]. The drag of the nacelle is relatively small compared with that of the middle to outer sections of the turbine blades [34]. Gao *et al.* [108] suggests that the nacelle wake should be included as it affects the development of the wake and its behaviour in terms of meandering, wake velocity and turbulent kinetic energy in the near and far wake. They also highlight that the effect of the nacelle on wakes from yawed turbines is greater than for those generated in un-yawed conditions, thus indicating that the nacelle should be included in simulations of wakes [108]. The presence of the turbine tower has also been shown to influence the behaviour and deflection of the wake [105][109]. Pierella and Saetran [109] noted the tower wake and its interaction with the main wake resulted in an asymmetric velocity deficit that is displaced away from the turbine centreline. Whereas Churchfield *et al.* [105] outlined how the wake recovery varies when the tower drag is implemented or not. Including its effect when considering the impact of wind veer and its directional influence on the behaviour of yawed turbines would provide a more representative output for how real wakes from physical turbines would respond to veered inflow. Including both the tower and nacelle wakes was considered when developing the methodology for this analysis. However, the implementation and testing required to do so accurately was ultimately beyond the scope of this thesis.

5.1.1 Model Modifications

Improving wake models, for both deflection and velocity deficit, to account for the effect of wind veer would lead to more accurate wake steering controllers. It would also allow the dynamics of the veered wake behaviour to be represented without needing the significant computational resource required of high fidelity simulations. Based on the wake behaviours observed in Chapter 4, various suggestions for wake model modifications are made below that would improve the capacity of currently used models to capture how wind veer affects the wake of yawed turbines.

The most obvious modification to the velocity deficit models would be to incorporate the inflow wind veer profile and how it influences the skew of the wake velocity deficit

area. The Abkar model achieves this via the following lateral displacement term,

$$\Delta y_{veer} \approx x \tan(\alpha_{in}) \tag{5.1}$$

where Δy_{veer} is the lateral change in wake centre due to veer, x is the distance downstream and α_{in} is the angle of the horizontal wind vector given by $\alpha_{in} = \frac{V_{in}}{U_{in}}$ with V_{in} and U_{in} as the height dependent lateral and streamwise inflow velocities, respectively. Introducing this term into the GCH model method in a similar approach as done with the wake deflection term would improve the modelled wake shape. The GCH model would then account for both the wake displacement due to yaw and the wake veer when calculating how the velocity deficit region is distributed. It should be noted that in Section 4.4, the veer of the wake was observed to match well with the inflow veer within $1D$ to $2D$ downstream of the rotor, after which the similarity between wake veer and inflow veer profile diminished with downstream distance. Therefore including a weighting term, proportional to downstream distance as a coefficient to the lateral displacement due to veer would then reflect how the skew magnitude changes with downstream distance.

Modifying the distribution of the velocity deficit to better match the more top-hat shaped profile observed in the SOWFA results would improve the estimates of available power for downstream turbines made by the models. This can be done by modifying the elements of the Gaussian function that control the spread of the profile. The GCH streamwise velocity deficit is given by the following Gaussian function [40],

$$\frac{u_G}{U_\infty} = 1 - C \exp\left(\frac{-(y - y_0 - \delta)^2}{2\sigma_y^2} - \frac{(z - z_h)^2}{2\sigma_z^2}\right), \tag{5.2}$$

where U_∞ is the freestream velocity, C_T is the thrust coefficient, δ is the wake deflection as calculated in Equation A.15, y_0 is the spanwise turbulent position, z_h is the hub height, σ_y is the wake width in the lateral direction and σ_z is the wake width in the vertical direction. The subscript "0" refers to value obtained at the start of the far wake, the location of which is determined as done in Equation A.8. This is nearly identical to the Gaussian used in the Abkar model, though deflection due to the veer rather than yawing is included [80]. The spread of the profile is proportional to σ and the magnitude of the power in the exponent term [110][111]. Varying these parameters would then improve the model representation of the velocity deficit profile shape observed in the simulation results, though further investigation into the specifics of how the velocity deficit changes in different atmospheric stabilities and with distance from the turbine is needed to fully understand what drives the variation in wake velocity.

The model constants used in these wake models, as based on prior experimental, numerical or field test results, should be selected to reflect the atmospheric stability

conditions the wake is generated in. These constants relate to various behaviours such as the wake expansion, wake deflection and momentum entrainment, and influence the model results for maximum velocity deficit and the recovery of the wake. Both the velocity deficit models appeared to under-predict the maximum velocity deficits at each downstream distance in the wake for both veered and non-veered flow, as shown in Figure 4.38. This could be related to using constants obtained from atmospheric conditions that differ from the stable atmospheric conditions tested in the simulations, rather than simply relying on generic values used in previous studies. This may require running high fidelity simulations of various atmospheric flows or isolating the wake behaviour for the atmospheric stabilities and fitting the model solution to those results. The use of varying model constants depending on the stability of the atmospheric flow should also be considered, given the behaviour of the wake has been shown to vary in different atmospheric conditions [27][28]. For example, Niayifar and Porté-Agel [112] suggested linking the growth rate to the local turbulence intensity within the wind farm.

The comparison of the deflection models and the SOWFA results revealed the models to not capture the deflection associated with veer. The effect of yawing on the wake deflection when turbines are in veered flow was also found to be minimal compared with the influence of veer on the wake centre location, for both methods tested. As the horizontal wind vector changes direction across the height of the rotor, the relative angle between inflow wind vector and the rotor plane changes with height, which likely causes the reduced impact of yawing on wake deflection. Thus it is worth investigating whether the models should include a height dependent, yaw angle that is relative to the inflow wind vectors across the full rotor, rather than one constant yaw angle. This could potentially improve the representation of yawed turbine wakes as produced in veered flow and relative contributions of veer and yawing to the location of the wake centre.

While the above modification considers the specific deflection variables in the models, it was also demonstrated that the wake skew and recovery of particular wake regions heavily influenced the wake centre location as determined via the minimum power method. Thus the above modifications to the velocity deficit model, and any others suggested from further investigations into yawed wakes in veered flow, should be tested prior to modifying the deflection models. It should also be noted that while the deflection profile output by the minimum power method provides relevant information on how wake steering affects downstream turbines, it is not suitable for wake modelling and was observed to differ from the results of the geometric wake centre method. The wake deflection models are generally used to identify the centreline of the wake at different heights and then use that location as a reference for modelling the spatial distribution of the velocity deficit. For this reason, methods that consider geometric wake centres are preferred in model development.

Given the irregular shapes of the skewed wakes and thus difficulty in locating a geometric wake centre based on Gaussian profiles, an alternative approach could be employed to determine the spatial centre of the simulated wakes, rather than simply the midpoint. For example, the 'centre of mass' method used by Howland *et al.* [46], which is applicable to asymmetric and non-Gaussian wakes with three-dimensional qualities is one such alternative. Applying this method to the SOWFA wake results and comparing the wake deflection profiles to those obtained from the deflection models could potentially highlight how the geometry of the wake shape is displaced due to veer and yaw in a manner that is conducive to the development of wake deflection models.

5.2 Implications of Wind Veer on Wake Steering

A clear and significant implication for wake steering in veered flow is the observation that high magnitude horizontal wind vector angles substantially skew the wake and modify the wake behaviour. This then has repercussions on the available power in waked flow and how a wake is perceived to deflect.

Whether veer is present or absent from the inflow conditions has an impact on the yaw angle that would achieve an improvement in power. Considering the results of the two turbine array simulations, as presented in Tables 4.1 and 4.2, when there is no veer present, yawing the upstream turbine by 20° results in a 9.81% or 196 kW increase in net power production. This exemplifies how wake steering can yield an improvement in wind farm or turbine array performance and has previously been demonstrated comprehensively in generally non-veered flows [11][19][20][22]. However, applying this same 20° yaw angle in veered flow, results in a 3.06% reduction in the total power production. There is, however, an increase in net power produced, albeit only a slight increase, when a yaw angle of −20° was instead applied, yielding a 0.29% or 6.35 kW increase in the total power from both turbines relative to the un-yawed turbine array in the same veered inflow conditions.

Yawing the upstream turbine in the veer profiles tested appears to be less effective in improving the downstream turbine power than as observed for the non-veered flow conditions. It is noted that the increase in power achieved in veered flow with the −20° yawed turbine is not a significant change and would perhaps not encourage the implementation of yaw in the upstream turbine, especially when accounting for any power losses that may be associated with the transient dynamics of the yaw actuator reaching the required yaw angle and the increase in loads experienced by the yawed turbine. However, it does reveal that yawing an upstream turbine still affects the conditions at the downstream turbine even in veered flow. Therefore, in veered flow with a smaller magnitude change in horizontal wind vector angle across the rotor, the comparative effect of veer and yaw on the wake deflection may be such that implementing wake steering yields a greater positive

change in the net power production of a turbine array.

The presence of wind veer also affects other aspects of the wake behaviour, beyond simply the wake deflection, and so the performance of both turbines in the array is influenced by the inflow veer profile. In veered flow, the total power of the two turbine array for all yaw angles is higher than that measured for all yaw angles in the non-veered flow. This increase in net power appears to be driven by the higher power produced by the downstream turbine in the array when the inflow is veered. As demonstrated in Section 4.2.2, skewed wakes have thinner cross-sections and so downstream turbines, particularly when no yawing is applied, would be exposed to partial wake conditions rather than the fully waked flow, which is more favourable for power generation. Section 4.3 also revealed that skewed wakes recover faster and so the velocity deficit experienced by the downstream turbine in veered flow would be less than that present in non-veered flow.

The necessity of implementing wake steering when the inflow involves veer is then questioned with both enhanced wake recovery and skew of the wake velocity deficit area being observed in veered flow. Again, the small improvement in net power yielded by the $-20°$ yaw angle in veered flow suggests wake steering can still have an effect, however this effectiveness may be dependent on the inflow conditions. For wake steering to be beneficial, any losses associated with yawing the upstream turbine must be overcompensated for by the net improvement in power production. So while applying a $-20°$ yaw in Lat10 conditions for a two turbine array improved the instantaneous power produced, the yaw actuator takes time to reach the desired yaw angle during which power losses may occur [16][24]. Similarly, yawing the upstream turbine increases the loads experienced by the turbine, which may cause the turbine to become damaged over time and possibly result in increased maintenance costs. These are additional factors that would be included in the decision to apply wake steering in commercially operating wind farms. It may thus be the case that the specific conditions at a wind farm site would need to be considered prior to implementation of wake steering to determine if it would be suitable or the method is only applied under specific conditions and 'turned off' when conditions change to avoid unnecessary losses in power production.

A critical concept to thus recognise when implementing wake steering is that the optimal yaw angle under veering conditions would be different to the optimal angle determined for non-veered flow. The disparity between the power improvement yielded between the veered and non-veered flow conditions for the same yaw angle applied to the upstream turbine in the array demonstrate that a wake steering controller needs to respond to the specific inflow conditions in a farm. In the strong veer conditions presented in this study, employing the optimal yaw angles determined by a wake steering controller that does not account for changes in deflection due to wind veer would very likely lead to

sub-par operating conditions or result in reduction in total power production, as occurred when 20° yawing was applied in Lat0 and Lat10 conditions. Based on these results of the two turbine simulations, it is suggested that implementing no yaw angle would be most effective. Therefore, the development of a wake model that incorporates both yaw and veer is necessary to achieve an increase in net power and to ensure that any applied yaw angle should not lead to power losses. As discussed above, the current models generally used in studies on wake steering do not depict the wake generated in veered flow well. Thus wake steering controllers, in their current iteration, would not be suitable for operating in veered wind conditions.

When multiple turbines are involved, the inflow wind veer profile may interact with notable features of the yawed turbine wakes that change how it deflects. The observation of secondary steering and identifying CRVs as its source in wind farms with yawed turbines was a substantial development in further understanding the behaviour of wakes generated in waked or partially waked flow [39][113]. The occurrence of secondary steering means yaw angles applied with the aim of steering the wake can be less than previously predicted as the deflected wakes also induce deflection [48]. Thus, power losses associated with yawing turbines can be minimised and unnecessary yawing avoided. Secondary steering occurs as the cross-stream velocity components due to the CRVs merge with the rotation and any CRVs from yawing of the turbine downstream in a manner that induces or enhances deflection in the downstream wake [48]. The presence of veer in the inflow wind also introduces an additional spanwise velocity component into the flow dynamics, as indicated by Figure 5.2 which would interact with the wake rotation and any CRV spanwise velocities present due to yawing. Similar to secondary steering due to CRVs, the downstream turbine wake exposed to the upstream turbine wake generated in the Lat10 flow conditions also demonstrated some wake deflection as shown in Figure 5.7. This behaviour in the downstream turbine wake exposed to a skew wake is important to understand as it would affect any how and if wake steering is applied to downstream turbines in large wind farms.

Capturing this more complex interaction between inflow veer and yawed turbines would also need to be accounted for in the wake models. While the GCH velocity deficit model was developed to account for the effect of secondary steering from yaw, it does not account for wind veer and so, as highlighted in Section 4.7, it does not capture the velocity deficit behaviour generated in veered flow. It is also unclear how a skewed and yawed upstream wake would affect the wake produced by a yawed turbine downstream and whether that may enhance or reduce the additional deflection due to secondary steering. Implementing the model modifications outlined in the previous Section may be sufficient for the GCH model to represent some aspect of the spanwise velocity component influence on deflection due to both veer and yaw. Though without further wake model development and increased

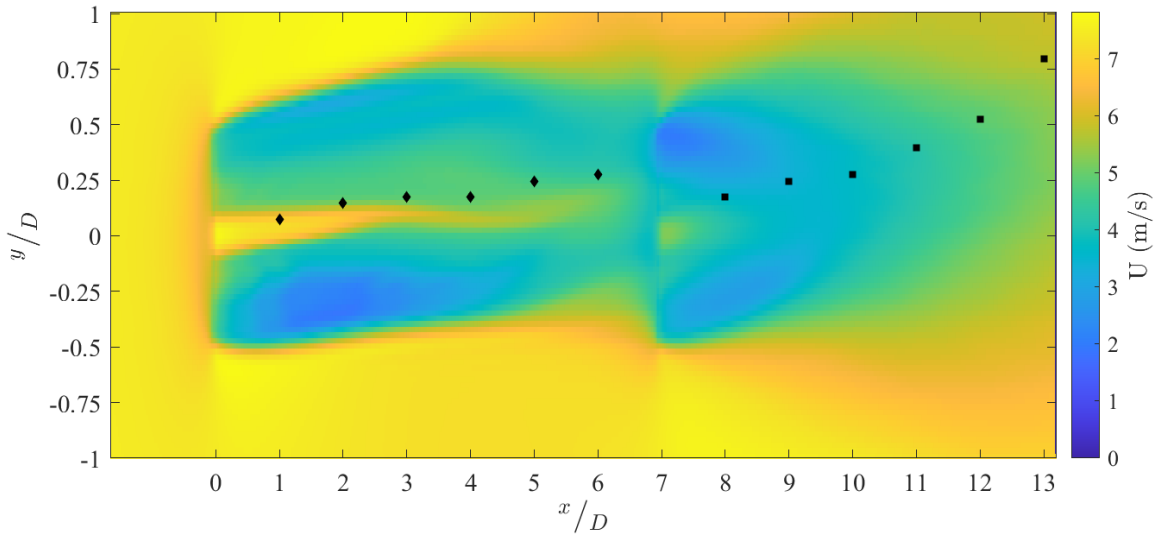

Figure 5.7: Top-down view of the streamwise velocity associated with 2 turbines in Lat10 flow without any yawing applied. The black diamonds and squares indicate the wake centre location for upstream and downstream turbine wakes, respectively.

understanding on how veer and yawing combine, the full effect of wind veer on yawed turbine wakes cannot be represented.

6. Conclusion

The outcome of this research is the confirmation that wind veer does affect wake behaviour, in a way that impacts the efficacy and implementation of wake steering. Wind veer was shown to influence the wake shape, its skew, how it recovers and its deflection, all of which contribute to the available power in the inflow conditions for downstream turbines.

The deflection of the wake was observed to be heavily influenced by the shape of the wind veer profile and the corresponding skew of the cross-sectional wake. The direction of skew exhibited in the wake region below hub height appears to indicate the direction of the wake centre deflection. When yawing is applied to turbines in veered flow, the impact of yaw on the wake deflection is significantly less than when it is applied in non-veered flow. As the relative angle between the horizontal wind vector and the turbine rotor plane changes across the height of the rotor, the same deflection achieved in non-veered flow via yawing cannot be obtained when veer is present. Similarly, the overall deflection of yawed wake in veered flow cannot be determined by summing the expected deflections from both sources, but rather, there is a more complex relationship between veer and yaw that requires further analysis to fully understand. Wakes in veered flow demonstrated their own degree of wake veer, though the magnitude of this wake veer was less than the inflow veer profile and decreased with downstream distance. Skewed wakes were also found to recover faster than those generated in non-veered flow.

The simulation of the two turbine array with wake steering also demonstrated that applying yaw angles deemed effective in non-veered flow would not have the same effect on power production in veered flow and may lead to a reduction in net power. Downstream turbines operating in veered flow conditions also produced more power than those in non-veered flow, due to the faster recovery of skewed wakes and thinner wake cross-sections. Several key aspects of the currently used wake models for wake steering controllers were also identified as areas where the models could be improved to better represent wakes from veered inflow. These include the shape of the wake and the distribution of the velocity deficit, while the relationship between deflections due to veer and yaw was revealed to be more complex than simply adding together a lateral offset associated with each.

While the results of this study reveal some patterns in the behaviour of the wake due to veer and yaw, there is not one general trend that can describe or predict how the wake would behave in such conditions. The interaction between the inflow and the turbine is

multi-variable and complex, thus further investigation into wake behaviour in veered flow is necessary to truly understand the dynamics occurring in the wake. This is particularly demonstrated by the variation in flow behaviour observed for some combinations of latitude and yaw angle and how they differed from the wake behaviours demonstrated by the same yaw angle in different latitudes and same latitude with different yaw angles. For example, the difference in downstream deflection profiles between Lat70 Yaw20 and Lat70 Yawneg20, as well as between Lat40 Yaw20 and Latneg40 Yawneg20. These results highlighted how various factors contribute to the propagation of the wake, how changes in the inflow wind conditions vary the wake behaviour and the theory that the presence of the counter-rotating vortex pair in yawed turbine wakes is affecting the wake dynamics.

Ultimately, the effectiveness of wake steering comes down to the ability to register and respond to the varying conditions of the inflow wind. The wake models currently used in wake steering controllers need to better capture the wake dynamics that contribute to the deflection of the wake and how the available power in the waked flow varies in magnitude and location relative to downstream turbines. Modifying the existing models such that factors, such as wind veer, which are shown in this thesis to influence the wake behaviour are included in the model calculations is a key step forward in the development of wake steering as a viable control approach for commercial wind farms.

While this research presents insights on how the wake changes as some aspects of the inflow wind changes, the relationship between turbine performance and inflow wind remains complex and dependent on a greater range of parameters than those tested in this thesis. As such, further analysis on wake steering in a wider range of realistic wind, atmospheric flow conditions is still required to sufficiently validate the effectiveness of the control technique. There is also scope for further discussion and investigation in to when the application of wake steering is no longer effective given the inflow conditions, as well tailoring any control strategies in wind farms to the specific conditions that occur at the wind farm site. Some of the limitations of this study and suggestions for future work into the validation of wake steering in realistic flow conditions are presented below in more detail below.

6.0.1 Limitations and Future Work

The flow conditions tested in this research only represent a small slice of the range of wind conditions a wind farm experiences in reality. It was a deliberate choice to focus on the stable boundary layer (SBL), however, aside from the latitude, the stable atmospheric conditions used in each simulation were kept consistent. The surrounding freestream flow influences the wake behaviour in a myriad of ways, including how it recovers, expands and deflects while the shape of the veer profile across the rotor would change the behaviour

of the wake. Testing the effect of wind veer on a wind farm or larger turbine array would also reveal how wind veer influences wake behaviour and wind farm performance as multiple wakes are propagating through downstream turbines. Updating the wake models currently used in wake steering controllers to represent the impact of wind veer on the wake behaviour would improve the capacity of the technique to yield an increase in net power in veered inflow. Finally, further development of wake steering controllers and how they are actually implemented in operating wind farms is needed to ensure wake steering is accurately responding to the wind farm conditions.

Diversity of Veer Profiles

The magnitude of the wind angles across the rotor in this study were quite large and dominated the wake veer and shape of the wake when yawing was implemented. Analysing how wakes respond to wind veers of a lesser magnitude would reveal more on the nuance of the relationship between inflow wind veer and yawed wake behaviour, if the forces due to both are better balanced.

Veer in the SBL varies in magnitude, with recorded values ranging from 0.03°/m in winter to 0.095°/m in summer [114]. This corresponds to 3.78° and 11.97°, respectively, over the 126 m rotor of the NREL 5 MW Turbine. In this study, the change in horizontal wind vector angle ranged from a maximum of approximately 28° across the lower wake region to approximately 4° across the upper wake. Englberger *et al.* [78] showed the erosion of the wake to be enhanced with increasing wind veer and so the larger veer values tested in this study have be having a greater effect on wake flow than would be observed in actual wind farms. Thus, testing smaller magnitude wind vector angles may be more representative of real, veered flow conditions.

Englberger and Lunquist [36] have previously tested different veer profile shapes across a turbine rotor, though the study focused more on its effect on wind speed and did not consider yawed turbines. Yawing the turbine introduces the CRV pair and so isolating the effect of veer over different parts of the rotor would reveal more on how yawed wakes behave in veered flow. Given the variation in wake behaviour observed between yaw angles for the same veered inflow and also the variation between wakes from the same yaw angle in different veered flows, understanding the particular dynamics involved is needed to address wake losses in wind farms.

Lundquist [30] highlights that the current knowledge surrounding wake behaviour and turbine performance in veered flow is primarily from simulations. Similarly, this research utilised numerical methods to analyse deflected wakes when the inflow is veered. Thus, measurements and analysis of wake behaviour from field tests when veer is present are necessary to validate the wake dynamics indicated by the simulation results and

demonstrate the actual flow conditions a wind farm may experience.

Multiple Turbines in Veered Flow

Considering the cumulative impact of wind veer on a larger wind farm or turbine array and the flow dynamics occurring for turbines exposed to multiples wakes produced in veered flow is needed to better understand how wind veer would affect the performance of a more realistic wind farm set up. It would also investigate the interaction between wind veer and the secondary steering phenomenon observed in the wakes produced by turbines exposed to deflected wakes. This phenomenon occurs as the spanwise velocities from the CRV pair generated by a yawed rotor compound as the wake travels downstream through multiple turbines [48]. As veered inflow involves an additional component of spanwise velocity into the flow dynamics, there may be a relationship between secondary steering and the inflow veer profile wherein the downstream turbine deflection could be enhanced or reduced.

As downstream turbines operate in the wakes from those upstream, the wake flow becomes more turbulent as the inflow conditions for the turbine consist of multiple wakes [115]. The power production and maximum velocity deficit in the wake are observed to plateau after approximately three turbines as an equilibrium is reached between the low energy waked inflow conditions for the turbine and the enhanced recovery of the wake due to its increased mixing with the surrounding flow and thus recovery [115]. Wake recovery was found to be enhanced in veered inflow, which would effect the flow conditions within a large wind farm exposed to an inflow wind veer profile. If wake recovery is sufficiently enhanced due to veer and multiple wake scenarios, there may not be a need for additional wind farm optimisation techniques.

Improvement of Wake Models

A key next step in the development of wake steering controllers and validation of the technique for use in realistic wind conditions would be to close the gap between models that can accurately depict the wake shape, deflection and velocity deficit produced from veered inflow and yawed turbines. As highlighted in Section 4.7, the wake models currently used in wake steering controller development do not capture the dynamics of veered wakes well and various suggestions to improve the models are made in Section 5.1.1. The suggested model modifications include changes to the wake shape, velocity deficit distribution and its deflection due to both veer and yaw.

Implementing these modifications would improve how the models represent the flow behaviour observed in this study, though further research into updating the wake models is needed to ensure the models reflect the variation wake behaviour due to the inflow

conditions. Similarly, the deflection due to the veer and yawing was found to not be a simple superimposition relationship and so testing different veer profiles and yaw angles, as suggested above, would reveal more on this complex relationship and assist in its parameterisation for inclusion in the wake models.

The simulations of the wakes in veered flow could also be improved. Including the drag effects of the turbine nacelle and tower would also improve the capacity of numerical simulations to represent realistic turbine wake behaviour. Ensuring the full deflected wake cross-section is captured in the refined region of the simulation domain, would also ensure the analysis more accurately reflects the full picture of the wake behaviour.

Further Wake Steering Controller Development

Given the variation in results obtained for the assorted combinations of veer profiles and yaw angles, the relationship between veer and yawed turbines is complex and goes beyond simply modifying the wake deflection. The suggestions for model modifications outlined above in Section 5.1.1, could well improve the representation of wake behaviour in veered flow, though further research and model development is necessary to ensure the relevant variations in flow features compared with non-veered flow are captured. The complexity and nuance of the relationship between wake flow and wind veer, may indicate that simplified analytical or parametric wake models alone may not be suitable to encapsulate the full picture of wakes in atmospheric flows.

The current format of wake steering controllers involves utilising look-up tables of pre-determined optimal yaw angles for the given wind conditions based on models. The concept of active wake control (AWC) methods have been suggested as a more ideal approach [17][116], using instantaneous measurements of the wind flow at the farm as input conditions and generating a control strategy specific to those conditions. However, AWC is limited by the speed of the wake model calculations and the optimisation algorithm. For a wake model to represent increasingly complex behaviours, the complexity of the model itself will likely increase and so too will the time needed for calculation.

Wind farm control methods must therefore seek a balance between accurately responding to the conditions at the wind farm and having the capacity to implement a suitable strategy in a timely manner, before it is no longer relevant to the inflow. This issue of balance could be addressed by tailoring the wake steering approach to specific wind farms prior to implementation.

This could be achieved by first running a campaign to measure the range of wind conditions experienced by the wind farm. Wharton and Lundquist [69] suggests the stability of the atmospheric flow can be reasonably assessed by measuring wind shear or

the turbulent kinetic energy across the height of the rotor. The authors also found the turbulent kinetic energy to be an effective turbulence stability parameter to characterise the flow [69] . Operating wind farms tend to only measure the wind speed and direction via a wind vane on the nacelle [20][22]. Data regarding the stability of the wind flow or measurements of the inflow wind veer angles are not taken at the farm site.

Wake dynamics can be difficult to measure in the field as they require the use of lidar [33][69], meteorological masts of comparable height to the turbine [31] or supervisory control and data acquisition (SCADA) [117]. Thus, high fidelity simulations of yawed wake behaviour and the farm performance could be performed using the recorded data as inflow conditions. These simulation results could then be used as the actual wake results used in the optimisation algorithm to obtain the optimal yaw set-points per the given wind conditions. Alternatively, and perhaps more effectively, the simulation results could be used to tune a wake model to the observed wake behaviour, allowing for more permutations of the inflow conditions and yaw angles to be modelled than would be possible with the computationally intensive high-fidelity simulations.

Additional issues that this study now highlights in regard to wake steering, that would need to be addressed prior to implementation of the technique in commercial winds farms include whether the controller should track changes in stability of the flow and how much additional sensing of flow parameters is needed for wake steering to be effective. Ultimately, further research is necessary to determine whether additional sensing of wind flow parameters, such as the wind veer angles across the rotor or atmospheric stability, is needed for wake steering to actually succeed in realistic flows. Similarly, it should be determined if wake steering would yield such power improvements that implementing additional sensors is worthwhile or whether an approach such as that outlined above would be effective.

References

[1] R. P. Allan, C. Cassou, D. Chen, *et al.*, "Summary for Policymakers," en, p. 32,

[2] United Nations, *COP26: Together for our planet*, en, Publisher: United Nations. [Online]. Available: https://www.un.org/en/climatechange/cop26 (visited on 01/21/2022).

[3] United Nations, *The Paris Agreement*, en, Publisher: United Nations. [Online]. Available: https://www.un.org/en/climatechange/paris-agreement (visited on 07/30/2022).

[4] IPCC, "Climate Change 2022: Impacts, Adaptation and Vulnerability," 2022, Contribution of Working Group II to the Sixth Assessment Report of the Intergovernmental Panel on Climate Change [H.-O. Pörtner, D.C. Roberts, M. Tignor, E.S. Poloczanska, K. Mintenbeck, A. Alegría, M. Craig, S. Langsdorf, S. Löschke, V. Möller, A. Okem, B. Rama (eds.)] DOI: 10.1017/9781009325844.

[5] IEA, "World Energy Outlook 2021," en, p. 386, 2022.

[6] BP, "BP Energy Outlook 2022," en, p. 57, 2022.

[7] BP, *Electrification in 2022*, en. [Online]. Available: https://www.bp.com/en/global/corporate/news-and-insights/reimagining-energy/electrification-in-2022.html (visited on 05/02/2022).

[8] *Renewable Energy Statistics 2022*, en. [Online]. Available: https://www.irena.org/publications/2022/Jul/Renewable-Energy-Statistics-2022 (visited on 10/19/2022).

[9] IEA, *Wind - Fuels & Technologies*, en-GB. [Online]. Available: https://www.iea.org/fuels-and-technologies/wind (visited on 05/04/2022).

[10] T. Burton, N. Jenkins, D. Sharpe, and E. Bossanyi, *Wind Energy Handbook*, en. John Wiley & Sons, May 2011, ISBN: 978-1-119-99392-6.

[11] P. M. O. Gebraad, F. W. Teeuwisse, J. W. v. Wingerden, *et al.*, "Wind plant power optimization through yaw control using a parametric model for wake effects—a CFD simulation study," en, *Wind Energy*, vol. 19, no. 1, pp. 95–114, 2016, ISSN: 1099-1824. DOI: 10.1002/we.1822.

[12] F. Porté-Agel, M. Bastankhah, and S. Shamsoddin, "Wind-Turbine and Wind-Farm Flows: A Review," *Boundary-Layer Meteorology*, vol. 174, no. 1, 2020. DOI: 10.1007/s10546-019-00473-0.

[13] Á. Jiménez, A. Crespo, and E. Migoya, "Application of a LES technique to characterize the wake deflection of a wind turbine in yaw," en, *Wind Energy*, vol. 13, no. 6, pp. 559–572, 2010, ISSN: 1099-1824. DOI: 10.1002/we.380.

[14] R. J. Barthelmie, K. Hansen, S. T. Frandsen, *et al.*, "Modelling and measuring flow and wind turbine wakes in large wind farms offshore," en, *Wind Energy*, vol. 12, no. 5, pp. 431–444, 2009, ISSN: 1099-1824. DOI: 10.1002/we.348.

[15] R. Baños, F. Manzano-Agugliaro, F. G. Montoya, C. Gil, A. Alcayde, and J. Gómez, "Optimization methods applied to renewable and sustainable energy: A review," *Renewable and Sustainable Energy Reviews*, vol. 15, no. 4, pp. 1753–1766, May 2011. DOI: 10.1016/j.rser.2010.12.008.

[16] S. Kanev, "Dynamic wake steering and its impact on wind farm power production and yaw actuator duty," en, *Renewable Energy*, vol. 146, pp. 9–15, Feb. 2020, ISSN: 0960-1481. DOI: 10.1016/j.renene.2019.06.122.

[17] A. Rott, B. Doekemeijer, J. K. Seifert, J.-W. van Wingerden, and M. Kühn, "Robust active wake control in consideration of wind direction variability and uncertainty," English, *Wind Energy Science*, vol. 3, no. 2, pp. 869–882, Nov. 2018, ISSN: 2366-7443. DOI: 10.5194/wes-3-869-2018.

[18] J. W. v. Wingerden, P. A. Fleming, T. Göçmen, *et al.*, "Expert elicitation on wind farm control," en, *Journal of Physics: Conference Series*, vol. 1618, no. 2, p. 022 025, Sep. 2020, ISSN: 1742-6596. DOI: 10.1088/1742-6596/1618/2/022025.

[19] P. A. Fleming, P. M. O. Gebraad, S. Lee, *et al.*, "Evaluating techniques for redirecting turbine wakes using SOWFA," en, *Renewable Energy*, Special issue on aerodynamics of offshore wind energy systems and wakes, vol. 70, pp. 211–218, Oct. 2014, ISSN: 0960-1481. DOI: 10.1016/j.renene.2014.02.015.

[20] P. Fleming, J. King, K. Dykes, *et al.*, "Initial results from a field campaign of wake steering applied at a commercial wind farm – Part 1," English, *Wind Energy Science*, vol. 4, no. 2, pp. 273–285, May 2019, Publisher: Copernicus GmbH, ISSN: 2366-7443. DOI: https://doi.org/10.5194/wes-4-273-2019.

[21] P. Fleming, J. King, E. Simley, *et al.*, "Continued results from a field campaign of wake steering applied at a commercial wind farm – Part 2," English, *Wind Energy Science*, vol. 5, no. 3, pp. 945–958, Jul. 2020, ISSN: 2366-7443. DOI: https://doi.org/10.5194/wes-5-945-2020.

[22] M. F. Howland, A. S. Ghate, S. K. Lele, and J. O. Dabiri, "Optimal closed-loop wake steering – Part 1: Conventionally neutral atmospheric boundary layer conditions," English, *Wind Energy Science*, vol. 5, no. 4, pp. 1315–1338, Oct. 2020, ISSN: 2366-7443. DOI: 10.5194/wes-5-1315-2020.

[23] J. Annoni, P. Fleming, A. Scholbrock, *et al.*, "Analysis of control-oriented wake modeling tools using lidar field results," *Wind Energy Science*, vol. 3, no. 2, pp. 819–831, Nov. 2018, ISSN: 2366-7443. DOI: https://doi.org/10.5194/wes-3-819-2018.

[24] E. Simley, P. Fleming, and J. King, "Design and analysis of a wake steering controller with wind direction variability," English, *Wind Energy Science*, vol. 5, no. 2, pp. 451–468, Apr. 2020, ISSN: 2366-7443. DOI: https://doi.org/10.5194/wes-5-451-2020.

[25] R. B. Stull, *An Introduction to Boundary Layer Meteorology*, en. Springer Science & Business Media, Dec. 2012, ISBN: 978-94-009-3027-8.

[26] M. J. Churchfield, S. Lee, J. Michalakes, and P. J. Moriarty, "A numerical study of the effects of atmospheric and wake turbulence on wind turbine dynamics," en, *Journal of Turbulence*, vol. 13, N14, Jan. 2012, ISSN: 1468-5248. DOI: 10.1080/14685248.2012.668191.

[27] M. Abkar and F. Porté-Agel, "Influence of atmospheric stability on wind-turbine wakes: A large-eddy simulation study," *Physics of Fluids*, vol. 27, no. 3, p. 035 104, Mar. 2015, Publisher: American Institute of Physics, ISSN: 1070-6631. DOI: 10.1063/1.4913695.

[28] L. Vollmer, G. Steinfeld, D. Heinemann, and M. Kühn, "Estimating the wake deflection downstream of a wind turbine in different atmospheric stabilities: An LES study," English, *Wind Energy Science*, vol. 1, no. 2, pp. 129–141, Sep. 2016, ISSN: 2366-7443. DOI: 10.5194/wes-1-129-2016.

[29] B. M. Doekemeijer, D. van der Hoek, and J.-W. van Wingerden, "Closed-loop model-based wind farm control using FLORIS under time-varying inflow conditions," en, *Renewable Energy*, vol. 156, pp. 719–730, Aug. 2020, ISSN: 0960-1481. DOI: 10.1016/j.renene.2020.04.007.

[30] J. K. Lundquist, "Wind Shear and Wind Veer Effects on Wind Turbines," en, in *Handbook of Wind Energy Aerodynamics*, B. Stoevesandt, G. Schepers, P. Fuglsang, and S. Yuping, Eds., Cham: Springer International Publishing, 2021, pp. 1–22, ISBN: 978-3-030-05455-7. DOI: 10.1007/978-3-030-05455-7_44-1.

[31] M. Bromm, A. Rott, H. Beck, L. Vollmer, G. Steinfeld, and M. Kühn, "Field investigation on the influence of yaw misalignment on the propagation of wind turbine wakes," en, *Wind Energy*, vol. 21, no. 11, pp. 1011–1028, 2018, ISSN: 1099-1824. DOI: 10.1002/we.2210.

[32] R. Nouri, A. Vasel-Be-Hagh, and C. L. Archer, "The Coriolis force and the direction of rotation of the blades significantly affect the wake of wind turbines," en, *Applied Energy*, vol. 277, p. 115 511, Nov. 2020, ISSN: 0306-2619. DOI: 10.1016/j.apenergy.2020.115511.

[33] N. Bodini, D. Zardi, and J. K. Lundquist, "Three-dimensional structure of wind turbine wakes as measured by scanning lidar," English, *Atmospheric Measurement Techniques*, vol. 10, no. 8, pp. 2881–2896, Aug. 2017, ISSN: 1867-1381. DOI: 10.5194/amt-10-2881-2017.

[34] M. J. Churchfield and S. Sirnivas, "On the effects of wind turbine wake skew caused by wind veer," in *2018 Wind Energy Symposium*, American Institute of Aeronautics and Astronautics, 2018.

[35] M. Bromm, L. Vollmer, and M. Kühn, "Numerical investigation of wind turbine wake development in directionally sheared inflow," en, *Wind Energy*, vol. 20, no. 3, pp. 381–395, 2017, ISSN: 1099-1824. DOI: https://doi.org/10.1002/we.2010.

[36] A. Englberger and J. K. Lundquist, "How does inflow veer affect the veer of a wind-turbine wake?" en, *Journal of Physics: Conference Series*, vol. 1452, p. 012 068, Jan. 2020, ISSN: 1742-6596. DOI: 10.1088/1742-6596/1452/1/012068.

[37] M. Abkar and F. Porté-Agel, "Influence of the Coriolis force on the structure and evolution of wind turbine wakes," *Physical Review Fluids*, vol. 1, no. 6, p. 063 701, Oct. 2016, Publisher: American Physical Society. DOI: 10.1103/PhysRevFluids.1.063701.

[38] N. O. Jensen, *A note on wind generator interaction*, English. Risø National Laboratory, 1983, ISBN: 978-87-550-0971-4.

[39] M. Bastankhah and F. Porté-Agel, "Experimental and theoretical study of wind turbine wakes in yawed conditions," English, *Journal of Fluid Mechanics*, vol. 806, pp. 506–541, Nov. 2016, ISSN: 00221120. DOI: http://dx.doi.org.ezproxy.library.sydney.edu.au/10.1017/jfm.2016.595.

[40] J. King, P. Fleming, R. King, *et al.*, "Control-oriented model for secondary effects of wake steering," en, *Wind Energy Science*, vol. 6, no. 3, pp. 701–714, May 2021, ISSN: 2366-7451. DOI: 10.5194/wes-6-701-2021.

[41] L. J. Vermeer, J. N. Sørensen, and A. Crespo, "Wind turbine wake aerodynamics," *Progress in Aerospace Sciences*, vol. 39, no. 6, pp. 467–510, Aug. 2003. DOI: 10.1016/S0376-0421(03)00078-2.

[42] E. Hau, *Wind Turbines*. Berlin, Heidelberg: Springer Berlin Heidelberg, 2013, ISBN: 978-3-642-27150-2 978-3-642-27151-9. DOI: 10.1007/978-3-642-27151-9.

[43] W. Zhang, C. D. Markfort, and F. Porté-Agel, "Near-wake flow structure downwind of a wind turbine in a turbulent boundary layer," en, *Experiments in Fluids*, vol. 52, no. 5, pp. 1219–1235, May 2012, ISSN: 1432-1114. DOI: 10.1007/s00348-011-1250-8.

[44] L. P. Chamorro and F. Porté-Agel, "A wind-tunnel investigation of wind-turbine wakes: Boundary-layer turbulence effects," *Boundary-Layer Meteorology*, vol. 132, no. 1, pp. 129–149, Jul. 2009, ISSN: 1573-1472. DOI: 10.1007/s10546-009-9380-8.

[45] M. F. Howland, S. K. Lele, and J. O. Dabiri, "Wind farm power optimization through wake steering," *Proceedings of the National Academy of Sciences*, vol. 116, no. 29, pp. 14 495–14 500, Jul. 2019, Publisher: Proceedings of the National Academy of Sciences. DOI: 10.1073/pnas.1903680116.

[46] M. F. Howland, J. Bossuyt, L. A. Martínez-Tossas, J. Meyers, and C. Meneveau, "Wake structure in actuator disk models of wind turbines in yaw under uniform inflow conditions," *Journal of Renewable and Sustainable Energy*, vol. 8, no. 4, p. 043 301, Jul. 2016, Publisher: American Institute of Physics. DOI: 10.1063/1.4955091.

[47] P. Fleming, J. Annoni, A. Scholbrock, *et al.*, "Full-scale field test of wake steering," en, *Journal of Physics: Conference Series*, vol. 854, p. 012 013, May 2017, ISSN: 1742-6588, 1742-6596. DOI: 10.1088/1742-6596/854/1/012013.

[48] P. Fleming, J. Annoni, M. Churchfield, *et al.*, "A simulation study demonstrating the importance of large-scale trailing vortices in wake steering," English, *Wind Energy Science*, vol. 3, no. 1, pp. 243–255, May 2018, ISSN: 2366-7443. DOI: https://doi.org/10.5194/wes-3-243-2018.

[49] G. C. Larsen, H. A. Madsen, K. Thomsen, and T. J. Larsen, "Wake meandering: A pragmatic approach," en, *Wind Energy*, vol. 11, no. 4, pp. 377–395, 2008, ISSN: 1099-1824. DOI: 10.1002/we.267.

[50] N. S. Ghaisas, C. L. Archer, S. Xie, S. Wu, and E. Maguire, "Evaluation of layout and atmospheric stability effects in wind farms using large-eddy simulation," en, *Wind Energy*, vol. 20, no. 7, pp. 1227–1240, 2017, ISSN: 1099-1824. DOI: 10.1002/we.2091.

[51] C. L. Archer, S. Mirzaeisefat, and S. Lee, "Quantifying the sensitivity of wind farm performance to array layout options using large-eddy simulation," *Geophysical Research Letters*, vol. 40, no. 18, pp. 4963–4970, 2013, ISSN: 1944-8007. DOI: 10.1002/grl.50911.

[52] J. Schottler, A. Hölling, J. Peinke, and M. Hölling, "Wind tunnel tests on controllable model wind turbines in yaw," in *34th Wind Energy Symposium*, American Institute of Aeronautics and Astronautics, Jan. 2016.

[53] J. Bartl, F. Mühle, J. Schottler, *et al.*, "Wind tunnel experiments on wind turbine wakes in yaw: Effects of inflow turbulence and shear," English, *Wind Energy Science*, vol. 3, no. 1, pp. 329–343, Jun. 2018, Publisher: Copernicus GmbH, ISSN: 2366-7443. DOI: 10.5194/wes-3-329-2018.

[54] B. M. Doekemeijer, S. Kern, S. Maturu, *et al.*, "Field experiment for open-loop yaw-based wake steering at a commercial onshore wind farm in Italy," English, *Wind Energy Science*, vol. 6, no. 1, pp. 159–176, Jan. 2021, ISSN: 2366-7443. DOI: https://doi.org/10.5194/wes-6-159-2021.

[55] C. L. Archer and A. Vasel-Be-Hagh, "Wake steering via yaw control in multi-turbine wind farms: Recommendations based on large-eddy simulation," en, *Sustainable Energy Technologies and Assessments*, vol. 33, pp. 34–43, Jun. 2019, ISSN: 2213-1388. DOI: 10.1016/j.seta.2019.03.002.

[56] D. Wei, D. Wan, and C. Hu, "Numerical simulations of asymmetrical wake flows of a yawed wind turbine," en, OnePetro, Jun. 2021.

[57] F. Campagnolo, V. Petrović, C. L. Bottasso, and A. Croce, "Wind tunnel testing of wake control strategies," in *2016 American Control Conference (ACC)*, ISSN: 2378-5861, Jul. 2016, pp. 513–518. DOI: 10.1109/ACC.2016.7524965.

[58] J. H. Ferziger, M. Perić, and R. L. Street, "Finite Difference Methods," en, in *Computational Methods for Fluid Dynamics*, J. H. Ferziger, M. Perić, and R. L. Street, Eds., Cham: Springer International Publishing, 2020, pp. 41–79, ISBN: 978-3-319-99693-6.

[59] A. Schaffarczyk, *Understanding Wind Power Technology: Theory, Deployment and Optimisation*. Somerset, United Kingdom: John Wiley & Sons, Incorporated, 2014, ISBN: 978-1-118-70154-6.

[60] J. H. Ferziger, M. Perić, and R. L. Street, "Turbulent Flows," in *Computational Methods for Fluid Dynamics*, J. H. Ferziger, M. Perić, and R. L. Street, Eds., Cham: Springer International Publishing, 2020, pp. 347–419. DOI: 10.1007/978-3-319-99693-6_10.

[61] D. Mehta, A. H. van Zuijlen, B. Koren, J. G. Holierhoek, and H. Bijl, "Large eddy simulation of wind farm aerodynamics: A review," en, *Journal of Wind Engineering and Industrial Aerodynamics*, vol. 133, pp. 1–17, Oct. 2014, ISSN: 0167-6105. DOI: 10.1016/j.jweia.2014.07.002.

[62] I. Katic, "A Simple Model for Cluster Efficiency," *Ewec'86. Proceedings. Vol. 1*, pp. 407–410, 1987.

[63] G.-W. Qian and T. Ishihara, "A New Analytical Wake Model for Yawed Wind Turbines," en, *Energies*, vol. 11, no. 3, p. 665, Mar. 2018, ISSN: 1996-1073. DOI: 10.3390/en11030665.

[64] F. Blondel, M. Cathelain, P.-A. Joulin, and P. Bozonnet, "An adaptation of the super-Gaussian wake model for yawed wind turbines," en, *Journal of Physics: Conference Series*, vol. 1618, no. 6, p. 062 031, Sep. 2020, ISSN: 1742-6588, 1742-6596. DOI: 10.1088/1742-6596/1618/6/062031.

[65] L. A. Martínez-Tossas, J. Annoni, P. A. Fleming, and M. J. Churchfield, "The aerodynamics of the curled wake: A simplified model in view of flow control," English, *Wind Energy Science*, vol. 4, no. 1, pp. 127–138, Mar. 2019, ISSN: 2366-7443. DOI: 10.5194/wes-4-127-2019.

[66] S. Wharton and J. K. Lundquist, "Atmospheric stability affects wind turbine power collection," en, *Environmental Research Letters*, vol. 7, no. 1, p. 014 005, Jan. 2012, ISSN: 1748-9326. DOI: 10.1088/1748-9326/7/1/014005.

[67] J. C. Kaimal and J. J. Finnigan, *Atmospheric boundary layer flows: their structure and measurement*. New York: Oxford University Press, 1994, ISBN: 978-0-19-506239-7.

[68] P. Bechtle, M. Schelbergen, R. Schmehl, U. Zillmann, and S. Watson, "Airborne wind energy resource analysis," *arXiv:1808.07718 [physics]*, Mar. 2019, arXiv: 1808.07718.

[69] S. Wharton and J. K. Lundquist, "Assessing atmospheric stability and its impacts on rotor-disk wind characteristics at an onshore wind farm," en, *Wind Energy*, vol. 15, no. 4, pp. 525–546, 2012, ISSN: 1099-1824. DOI: https://doi.org/10.1002/we.483.

[70] M. L. Aitken, B. Kosović, J. D. Mirocha, and J. K. Lundquist, "Large eddy simulation of wind turbine wake dynamics in the stable boundary layer using the Weather Research and Forecasting Model," *Journal of Renewable and Sustainable Energy*, vol. 6, no. 3, p. 033 137, May 2014, Publisher: American Institute of Physics. DOI: 10.1063/1.4885111. [Online]. Available: http://aip.scitation.org/doi/10.1063/1.4885111.

[71] M. Dörenkämper, B. Witha, G. Steinfeld, D. Heinemann, and M. Kühn, "The impact of stable atmospheric boundary layers on wind-turbine wakes within offshore wind farms," en, *Journal of Wind Engineering and Industrial Aerodynamics*, Selected papers from the 6th International Symposium on Computational Wind Engineering CWE 2014, vol. 144, pp. 146–153, Sep. 2015, ISSN: 0167-6105. DOI: 10.1016/j.jweia.2014.12.011.

[72] General Electric, *World's Most Powerful Offshore Wind Platform: Haliade-X | GE Renewable Energy*. [Online]. Available: https://www.ge.com/renewableenergy/wind-energy/offshore-wind/haliade-x-offshore-turbine (visited on 10/18/2022).

[73] R. J. Barthelmie and L. E. Jensen, "Evaluation of wind farm efficiency and wind turbine wakes at the Nysted offshore wind farm," en, *Wind Energy*, vol. 13, no. 6, pp. 573–586, 2010, ISSN: 1099-1824. DOI: 10.1002/we.408.

[74] M. F. Howland, A. S. Ghate, and S. K. Lele, "Influence of the geostrophic wind direction on the atmospheric boundary layer flow," en, *Journal of Fluid Mechanics*, vol. 883, Jan. 2020, Publisher: Cambridge University Press, ISSN: 0022-1120, 1469-7645. DOI: 10.1017/jfm.2019.889.

[75] K. S. Hansen, R. J. Barthelmie, L. E. Jensen, and A. Sommer, "The impact of turbulence intensity and atmospheric stability on power deficits due to wind turbine wakes at Horns Rev wind farm," en, *Wind Energy*, vol. 15, no. 1, pp. 183–196, 2012, ISSN: 1099-1824. DOI: 10.1002/we.512.

[76] K. Bhaganagar and M. Debnath, "The effects of mean atmospheric forcings of the stable atmospheric boundary layer on wind turbine wake," *Journal of Renewable and Sustainable Energy*, vol. 7, no. 1, p. 013 124, Jan. 2015. DOI: 10.1063/1.4907687.

[77] G. Svensson and A. A. M. Holtslag, "Analysis of model results for the turning of the wind and related momentum fluxes in the stable boundary layer," en, *Boundary-Layer Meteorology*, vol. 132, no. 2, pp. 261–277, Aug. 2009, ISSN: 1573-1472. DOI: 10.1007/s10546-009-9395-1.

[78] A. Englberger, J. K. Lundquist, and A. Dörnbrack, "Changing the rotational direction of a wind turbine under veering inflow: A parameter study," English, *Wind Energy Science*, vol. 5, no. 4, pp. 1623–1644, Nov. 2020, ISSN: 2366-7443. DOI: 10.5194/wes-5-1623-2020.

[79] A. Englberger, A. Dörnbrack, and J. K. Lundquist, "Does the rotational direction of a wind turbine impact the wake in a stably stratified atmospheric boundary layer?" English, *Wind Energy Science*, vol. 5, no. 4, pp. 1359–1374, Oct. 2020, ISSN: 2366-7443. DOI: 10.5194/wes-5-1359-2020.

[80] M. Abkar, J. Sørensen, and F. Porté-Agel, "An analytical model for the effect of verticalwind veer on wind turbine wakes," *Energies*, vol. 11, no. 7, 2018. DOI: 10.3390/en11071838.

[81] J. W. Deardorff, "Numerical investigation of neutral and unstable planetary boundary layers," EN, *Journal of the Atmospheric Sciences*, vol. 29, no. 1, pp. 91–115, Jan. 1972, ISSN: 0022-4928, 1520-0469. DOI: 10.1175/1520-0469(1972)029<0091:NIONAU>2.0.CO;2.

[82] U. Schumann, "Subgrid scale model for finite difference simulations of turbulent flows in plane channels and annuli," en, *Journal of Computational Physics*, vol. 18, no. 4, pp. 376–404, Aug. 1975, ISSN: 0021-9991. DOI: 10.1016/0021-9991(75)90093-5.

[83] C.-H. Moeng, "A Large-Eddy-Simulation Model for the Study of Planetary Boundary-Layer Turbulence," EN, *Journal of the Atmospheric Sciences*, vol. 41, no. 13, pp. 2052–2062, Jul. 1984, ISSN: 0022-4928, 1520-0469. DOI: 10.1175/1520-0469(1984)041<2052:ALESMF>2.0.CO;2.

[84] R. J. Beare, M. K. Macvean, A. A. M. Holtslag, *et al.*, "An Intercomparison of Large-Eddy Simulations of the Stable Boundary Layer," en, *Boundary-Layer Meteorology*, vol. 118, no. 2, pp. 247–272, Feb. 2006, ISSN: 0006-8314, 1573-1472. DOI: 10.1007/s10546-004-2820-6.

[85] B. Kosović and J. A. Curry, "A large eddy simulation study of a quasi-steady, stably stratified atmospheric boundary layer," EN, *Journal of the Atmospheric Sciences*, vol. 57, no. 8, pp. 1052–1068, Apr. 2000, ISSN: 0022-4928, 1520-0469. DOI: 10.1175/1520-0469(2000)057<1052:ALESSO>2.0.CO;2.

[86] F. T. M. Nieuwstadt, "The turbulent structure of the stable, nocturnal boundary layer," EN, *Journal of the Atmospheric Sciences*, vol. 41, no. 14, pp. 2202–2216, Jul. 1984, ISSN: 0022-4928, 1520-0469. DOI: 10.1175/1520-0469(1984)041<2202:TTSOTS>2.0.CO;2.

[87] M. J. Churchfield, *Adding Complex Terrain and Stable Atmospheric Condition Capability to the Simulator for On/Offshore Wind Farm Applications (SOWFA)*, 2013.

[88] A. S. Monin and A. M. Obukhov, "Basic laws of turbulent mixing in the ground layer of the atmosphere," en, American Meteorological Society Boston, Tech. Rep., Jan. 1959.

[89] M. Churchfield, S. Lee, P. Moriarty, *et al.*, "A large-eddy simulation of wind-plant aerodynamics," en, in *50th AIAA Aerospace Sciences Meeting including the New Horizons Forum and Aerospace Exposition*, Nashville, Tennessee: American Institute of Aeronautics and Astronautics, Jan. 2012, ISBN: 978-1-60086-936-5. DOI: 10.2514/6.2012-537.

[90] R. I. Issa, "Solution of the implicitly discretised fluid flow equations by operator-splitting," *Journal of Computational Physics*, vol. 62, no. 1, pp. 40–65, 1986, Type: Journal Article, ISSN: 0021-9991. DOI: 10.1016/0021-9991(86)90099-9.

[91] C. M. Rhie and W. L. Chow, "Numerical study of the turbulent flow past an airfoil with trailing edge separation," *AIAA Journal*, vol. 21, no. 11, pp. 1525–1532, 1983, ISSN: 0001-1452. DOI: 10.2514/3.8284.

[92] X. Ning, M. Krutova, and M. Bakhoday-Paskyabi, "Analysis of offshore wind spectra and coherence under neutral stability condition using the two LES models PALM and SOWFA," en, *Journal of Physics: Conference Series*, vol. 2018, no. 1, p. 012 027, Sep. 2021, ISSN: 1742-6588, 1742-6596. DOI: 10.1088/1742-6596/2018/1/012027.

[93] H. Lu and F. Porté-Agel, "Large-eddy simulation of a very large wind farm in a stable atmospheric boundary layer," *Physics of Fluids*, vol. 23, no. 6, p. 065 101, Jun. 2011, ISSN: 1070-6631. DOI: 10.1063/1.3589857.

[94] K. Bhaganagar and M. Debnath, "Implications of stably stratified atmospheric boundary layer turbulence on the near-wake structure of wind turbines," en, *Energies*, vol. 7, no. 9, pp. 5740–5763, Sep. 2014, ISSN: 1996-1073. DOI: 10.3390/en7095740.

[95] S. Basu, A. A. M. Holtslag, B. J. H. Van De Wiel, A. F. Moene, and G.-J. Steeneveld, "An inconvenient "truth" about using sensible heat flux as a surface boundary condition in models under stably stratified regimes," en, *Acta Geophysica*, vol. 56, no. 1, pp. 88–99, Mar. 2008, ISSN: 1895-7455. DOI: 10.2478/s11600-007-0038-y.

[96] N. Troldborg, J. N. Sorensen, and R. Mikkelsen, "Numerical simulations of wake characteristics of a wind turbine in uniform inflow," en, *Wind Energy*, vol. 13, no. 1, pp. 86–99, 2010, ISSN: 1099-1824. DOI: 10.1002/we.345.

[97] R. Damiani, S. Dana, J. Annoni, *et al.*, "Assessment of wind turbine component loads under yaw-offset conditions," English, *Wind Energy Science*, vol. 3, no. 1, pp. 173–189, Apr. 2018, ISSN: 2366-7443. DOI: 10.5194/wes-3-173-2018.

[98] J. Jonkman, S. Butterfield, W. Musial, and G. Scott, "Definition of a 5-MW Reference Wind Turbine for Offshore System Development," English, National Renewable Energy Lab. (NREL), Golden, CO (United States), Tech. Rep. NREL/TP-500-38060, Feb. 2009.

[99] J. N. Sørensen and W. Z. Shen, "Numerical modeling of wind turbine wakes," *Journal of Fluids Engineering*, vol. 124, no. 2, pp. 393–399, May 2002, ISSN: 0098-2202. DOI: 10.1115/1.1471361.

[100] N. Troldborg, "Actuator Line Modeling of Wind Turbine Wakes," en, p. 143, 2008.

[101] M. J. Churchfield, S. J. Schreck, L. A. Martinez, C. Meneveau, and P. R. Spalart, "An advanced actuator line method for wind energy applications and beyond," in *35th Wind Energy Symposium*, American Institute of Aeronautics and Astronautics, 2017.

[102] A. Jimenez, A. Crespo, E. Migoya, and J. Garcia, "Advances in large-eddy simulation of a wind turbine wake," en, *Journal of Physics: Conference Series*, vol. 75, p. 012 041, Jul. 2007, ISSN: 1742-6596. DOI: 10.1088/1742-6596/75/1/012041.

[103] J. Bossuyt, R. Scott, N. Ali, and R. B. Cal, "Quantification of wake shape modulation and deflection for tilt and yaw misaligned wind turbines," en, *Journal of Fluid Mechanics*, vol. 917, A3, Jun. 2021, ISSN: 0022-1120, 1469-7645. DOI: 10.1017/jfm.2021.237.

[104] J.-J. Trujillo, F. Bingöl, G. C. Larsen, J. Mann, and M. Kühn, "Light detection and ranging measurements of wake dynamics. Part II: Two-dimensional scanning," en, *Wind Energy*, vol. 14, no. 1, pp. 61–75, 2011, ISSN: 1099-1824. DOI: 10.1002/we.402.

[105] M. J. Churchfield, S. Lee, S. Schmitz, and Z. Wang, "Modeling wind turbine tower and nacelle effects within an actuator line model," in *33rd Wind Energy Symposium*, American Institute of Aeronautics and Astronautics, 2015.

[106] L. Gao, B. Li, and J. Hong, "Effect of wind veer on wind turbine power generation," *Physics of Fluids*, vol. 33, no. 1, p. 015 101, Jan. 2021, ISSN: 1070-6631. DOI: 10.1063/5.0033826.

[107] H. Zong and F. Porté-Agel, "A point vortex transportation model for yawed wind turbine wakes," en, *Journal of Fluid Mechanics*, vol. 890, May 2020, ISSN: 0022-1120, 1469-7645. DOI: 10.1017/jfm.2020.123.

[108] Z. Gao, Y. Li, T. Wang, *et al.*, "Modelling the nacelle wake of a horizontal-axis wind turbine under different yaw conditions," en, *Renewable Energy*, vol. 172, pp. 263–275, Jul. 2021, ISSN: 0960-1481. DOI: 10.1016/j.renene.2021.02.140.

[109] F. Pierella and L. Sætran, "Wind tunnel investigation on the effect of the turbine tower on wind turbines wake symmetry," en, *Wind Energy*, vol. 20, no. 10, pp. 1753–1769, 2017, ISSN: 1099-1824. DOI: https://doi.org/10.1002/we.2120.

[110] H. Guo, "A simple algorithm for fitting a gaussian function (DSP Tips and Tricks)," *IEEE Signal Processing Magazine*, vol. 28, no. 5, pp. 134–137, Sep. 2011, Conference Name: IEEE Signal Processing Magazine, ISSN: 1558-0792. DOI: 10.1109/MSP.2011.941846.

[111] K. Sun, L. Zhu, K. Cady-Pereira, *et al.*, "A physics-based approach to oversample multi-satellite, multi-species observations to a common grid," *Atmospheric Measurement Techniques Discussions*, pp. 1–30, Aug. 2018. DOI: 10.5194/amt-2018-253.

[112] A. Niayifar and F. Porté-Agel, "A new analytical model for wind farm power prediction," *Journal of Physics: Conference Series*, vol. 625, no. 1, p. 012 039, Jun. 2015, ISSN: 1742-6596. DOI: 10.1088/1742-6596/625/1/012039.

[113] P. Fleming, P. M. O. Gebraad, S. Lee, *et al.*, "Simulation comparison of wake mitigation control strategies for a two-turbine case," *Wind Energy*, vol. 18, no. 12, pp. 2135–2143, 2015, ISSN: 1095-4244. DOI: 10.1002/we.1810.

[114] N. Bodini, J. K. Lundquist, and A. Kirincich, "Offshore wind turbines will encounter very low atmospheric turbulence," en, *Journal of Physics: Conference Series*, vol. 1452, p. 012 023, Jan. 2020, Publisher: IOP Publishing, ISSN: 1742-6596. DOI: 10.1088/1742-6596/1452/1/012023.

[115] B. Witha, G. Steinfeld, M. Dörenkämper, and D. Heinemann, "Large-eddy simulation of multiple wakes in offshore wind farms," en, *Journal of Physics: Conference Series*, vol. 555, no. 1, p. 012 108, Dec. 2014, ISSN: 1742-6596. DOI: 10.1088/1742-6596/555/1/012108.

[116] S. Kanev, "On the robustness of active wake control to wind turbine downtime," en, *Energies*, vol. 12, no. 16, p. 3152, Jan. 2019. DOI: 10.3390/en12163152.

[117] P. Brugger, t. l. w. o. i. a. n. w. Link to external site, M. Debnath, *et al.*, "Lidar measurements of yawed-wind-turbine wakes: Characterization and validation of analytical models," English, *Wind Energy Science*, vol. 5, no. 4, pp. 1253–1272, 2020, ISSN: 23667443. DOI: http://dx.doi.org.ezproxy.library.sydney.edu.au/10.5194/wes-5-1253-2020.

[118] S. Ghosal, "An analysis of numerical errors in large-eddy simulations of turbulence," en, *Journal of Computational Physics*, vol. 125, no. 1, pp. 187–206, Apr. 1996, ISSN: 0021-9991. DOI: 10.1006/jcph.1996.0088.

[119] A. G. Kravchenko and P. Moin, "On the effect of numerical errors in large eddy simulations of turbulent flows," en, *Journal of Computational Physics*, vol. 131, no. 2, pp. 310–322, Mar. 1997, ISSN: 0021-9991. DOI: 10.1006/jcph.1996.5597.

[120] J. P. Boris, F. F. Grinstein, E. S. Oran, and R. L. Kolbe, "New insights into large eddy simulation," en, *Fluid Dynamics Research*, vol. 10, no. 4-6, pp. 199–228, Dec. 1992, ISSN: 0169-5983, 1873-7005. DOI: 10.1016/0169-5983(92)90023-P.

[121] A. Bechmann, "Large-Eddy Simulation of Atmospheric Flow over Complex Terrain," en, Ph.D. dissertation, 2006.

[122] A. Leonard, "Energy Cascade in Large-Eddy Simulations of Turbulent Fluid Flows," en, in *Advances in Geophysics*, ser. Turbulent Diffusion in Environmental Pollution, F. N. Frenkiel and R. E. Munn, Eds., vol. 18, Elsevier, Jan. 1975, pp. 237–248.

[123] J. Smagorinsky, "General Circulation Experiments with the Primitive Equations: I. The Basic Experiment," EN, *Monthly Weather Review*, vol. 91, no. 3, pp. 99–164, Mar. 1963, ISSN: 1520-0493, 0027-0644. DOI: 10.1175/1520-0493(1963)091<0099:GCEWTP>2.3.CO;2.

[124] X. Gao, H. Yang, and L. Lu, "Optimization of wind turbine layout position in a wind farm using a newly-developed two-dimensional wake model," *Applied Energy*, vol. 174, pp. 192–200, Jul. 2016, ISSN: 0306-2619. DOI: 10.1016/j.apenergy.2016.04.098.

[125] M. Bastankhah and F. Porté-Agel, "A new analytical model for wind-turbine wakes," en, *Renewable Energy*, Special issue on aerodynamics of offshore wind energy systems and wakes, vol. 70, pp. 116–123, Oct. 2014, ISSN: 0960-1481. DOI: 10.1016/j.renene.2014.01.002.

[126] C. J. Bay, J. King, P. Fleming, R. Mudafort, and L. A. Martínez-Tossas, "Unlocking the full potential of wake steering: Implementation and assessment of a controls-oriented model," en, Control and system identification, preprint, May 2019.

[127] S. B. Pope and S. B. Pope, *Turbulent Flows*, en. Cambridge University Press, Aug. 2000, ISBN: 978-0-521-59886-6.

[128] R. B. Stull, *Practical Meteorology : An Algebra-based Survey of Atmospheric Science*, eng. University of British Columbia, 2015, Accepted: 2018-02-26T20:59:07Z.

A. Methodology

A.1 Grid Resolution

A.1.1 Atmospheric Flow

Figure A.1 presents the spanwise velocity profile with height for the three grids tested for implementation. The spanwise velocity profile was considered as varying the wind veer profile affects the spanwise velocities present across the rotor. As shown in the Figure, the 6.25m and Graded grids produced profiles that are very similar in the region across the turbine rotor, whereas the 12.5m grid was unable to resolve the same profile. Thus, the 12.5m grid was deemed insufficient for representing the SBL flow. As outlined in Section 3.2.4, the 6.25m grid was selected as graded grids have not been applied to SOWFA before and the skew of the grid introduces difficulties when defining the distribution function involved in the actuator line method.

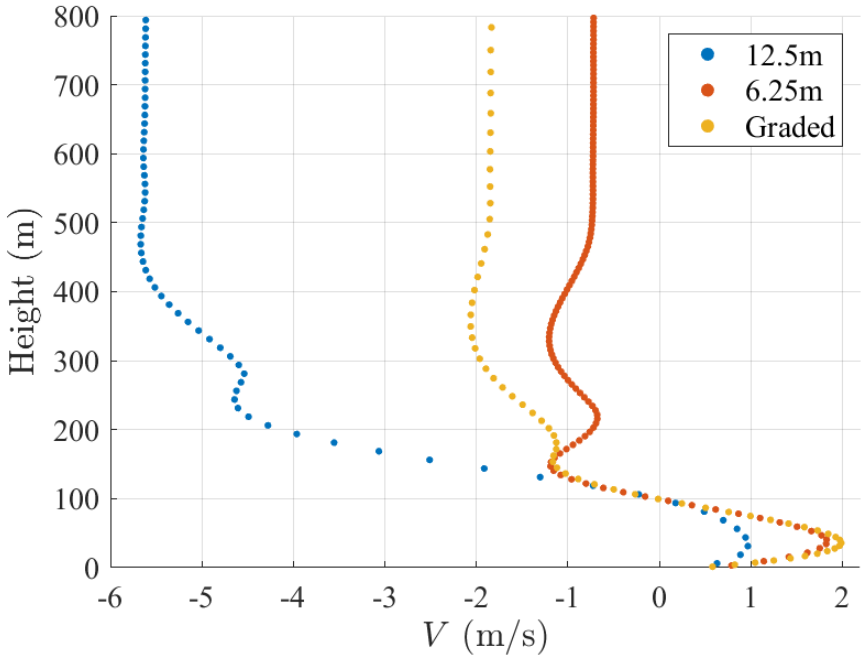

Figure A.1: Horizontally averaged spanwise velocity with height for the 12.5m, 6.25m and Graded grids

A.1.2 Turbine Grid Refinement

The grid around the turbine and wake region needs to be sufficiently refined to resolve the detailed flow structures. When only 1 area of refinement was applied, discontinuities were observed in the flow, as shown in Figure A.2.

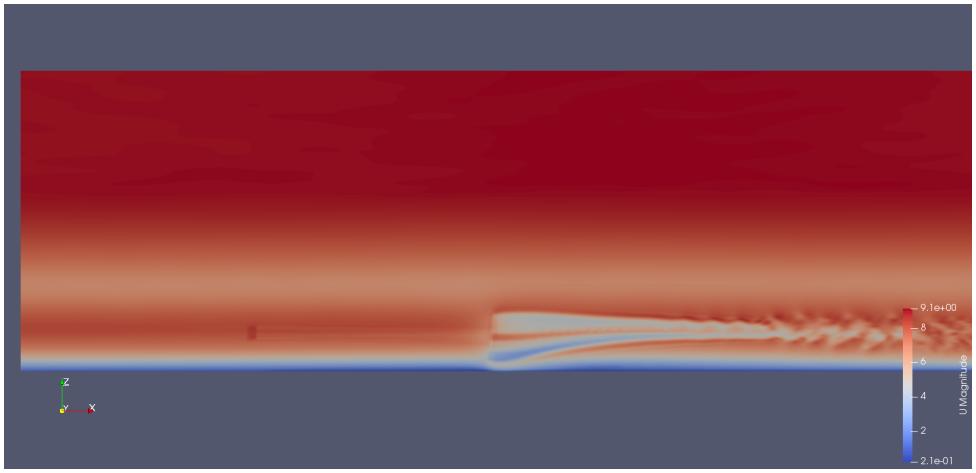

(a) Streamwise velocity, U

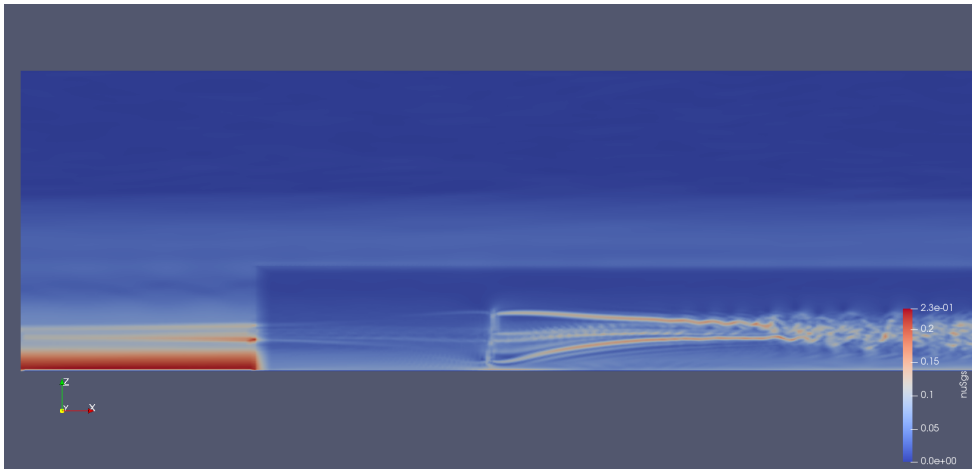

(b) SGS viscosity, ν_{SGS}

(c) SGS turbulent kinetic energy, k_{SGS}

Figure A.2: Observed flow discontinuities for one level of grid refinement

Regions of relatively higher SGS viscosity and turbulent kinetic energy (TKE) appear to propagate upstream from the blade tips and hub. This occurs due to dispersion errors associated with the advection scheme, meaning the numerical calculation is producing higher dispersion in the flow than what would occur physically [118][119]. This indicates insufficient resolution of the vortex structures that are shed from the rotor and hub. One level of refinement around the turbine area thus suggests that grid spacing of 6.25 m (horizontally) and 3.125 m (vertically) is not feasible for accurately resolving the wake behaviour. The grid in LES should resolve the larger, energy containing turbulent structures, which contain "most of the information of interest" according to Boris *et al.* [120]. If these structures are not resolved by the grid, more reliance is placed on the SGS turbulence model to accurately capture a greater range of turbulent scales. The diffusion provided by the SGS turbulence model may also then be insufficient to dissipate the oscillation in the flow that arises due to numerical dispersion [118][119]. Numerical dispersion tends to occur with low-order finite difference schemes, such as the second-order central difference equivalent finite volume approach used in SOWFA [26], and can dominate the SGS model contribution to the turbulence [118][119]. It can be addressed by changing the advection scheme, implementing a more diffuse SGS turbulence model or increasing the grid resolution, the latter of which was done for these simulations [60][121].

The SGS and larger turbulent structures are also not independent, with energy cascading from the larger eddies to those SGS eddies [122]. Similarly, the Smagorinsky model implemented in these simulations depends on values obtained on the resolved grid and the length-scale of the grid itself [83][123]. Therefore, appropriate resolution of the larger scale turbulent structures is required for the SGS turbulence model to be effective and this is not achievable when only one level of grid refinement is applied to the turbine and wake region.

A.2 Run Time

For each latitude case, the run time was determined to be the time after which the vertical momentum and buoyancy fluxes had settled and converged to a constant value. Figure A.3 presents both the momentum and buoyant flux results for each latitude case. The results were obtained and reviewed at heights across the rotor of 28 m and 60 m from the ground and at hub height, 90 m.

The fluxes were deemed to have converged when the magnitude of the flux was between $\pm 1 \times 10^{-4}$ for at least 3600s (1 hour).

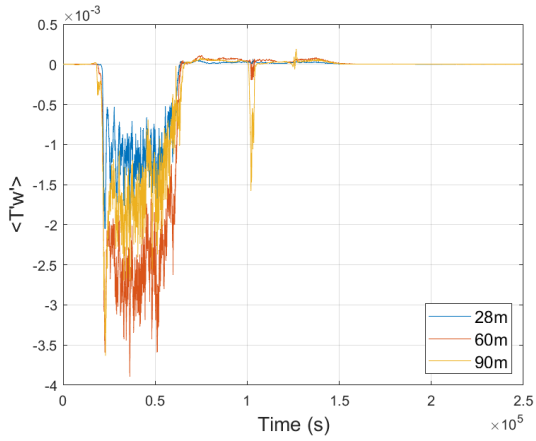

(a) Lat0, $< T'w' >$

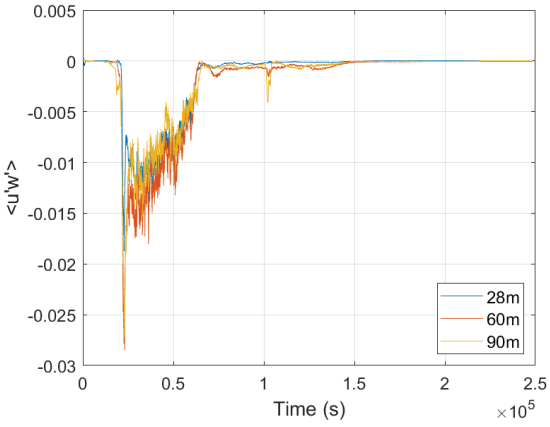

(b) Lat0, $< u'w' >$

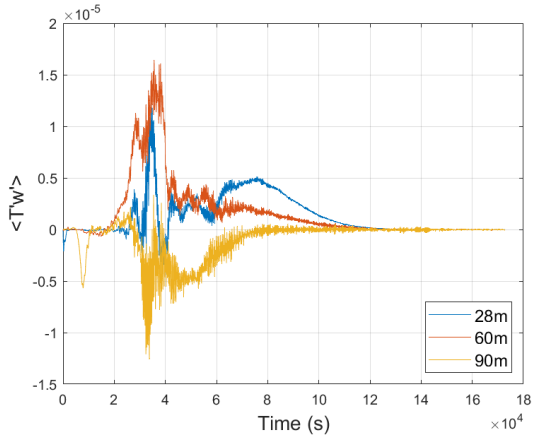

(c) Lat10, $< T'w' >$

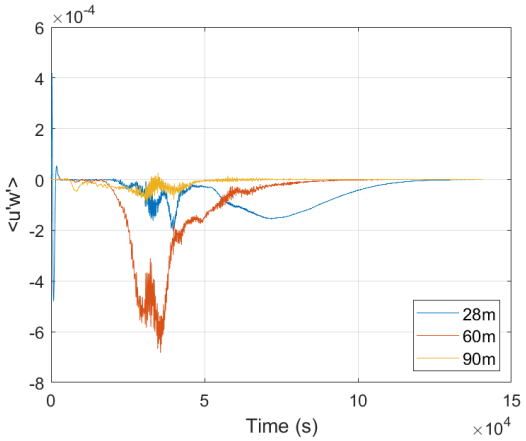

(d) Lat10, $< u'w' >$

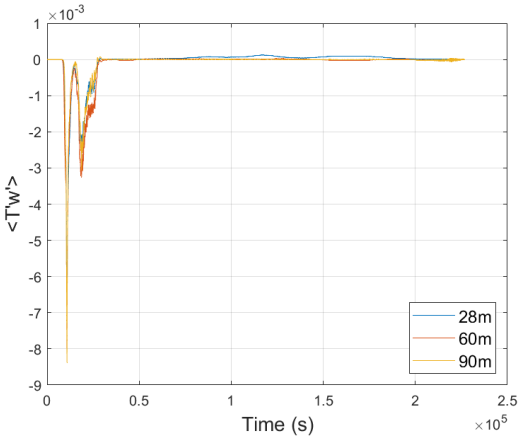

(e) Lat40, $< T'w' >$

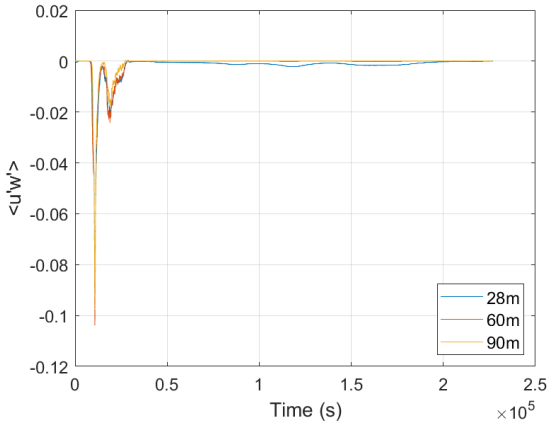

(f) Lat40, $< u'w' >$

Figure A.3: Horizontally averaged buoyancy (left) and momentum (right) fluxes for each latitude case (cont.)

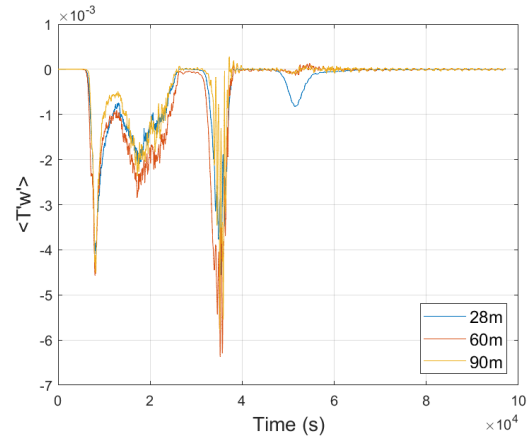

(g) Lat70, $< T'w' >$

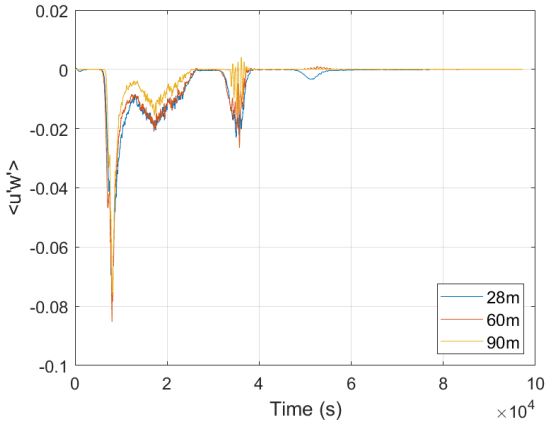

(h) Lat70, $< u'w' >$

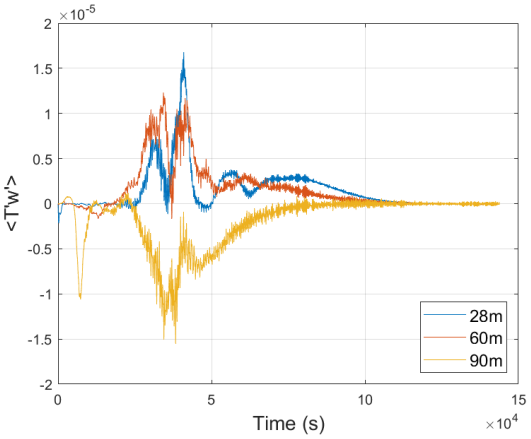

(i) Latneg10, $< T'w' >$

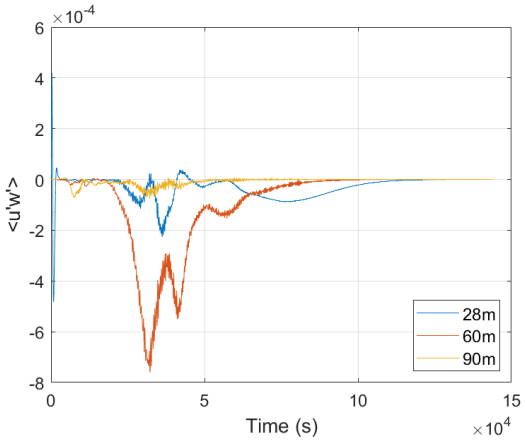

(j) Latneg10, $< u'w' >$

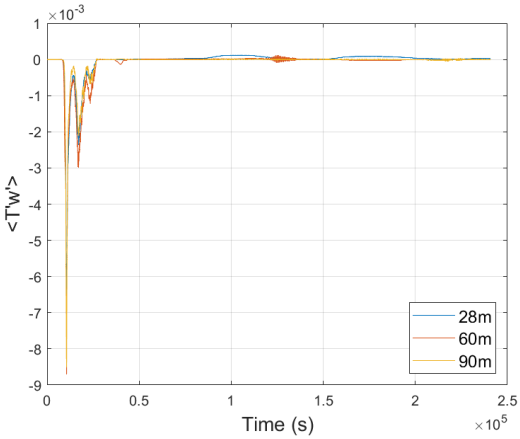

(k) Latneg40, $< T'w' >$

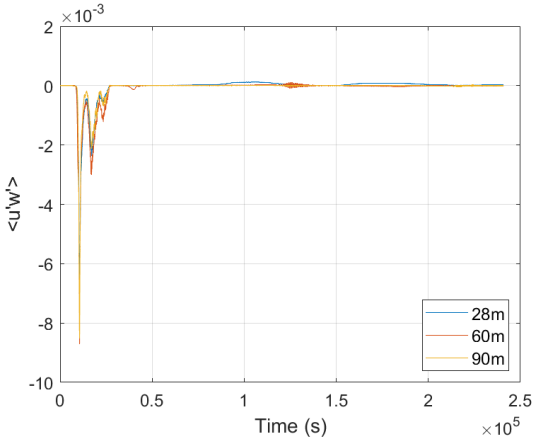

(l) Latneg40, $< u'w' >$

Figure A.3: Horizontally averaged buoyancy (left) and momentum (right) fluxes for each latitude case (cont.)

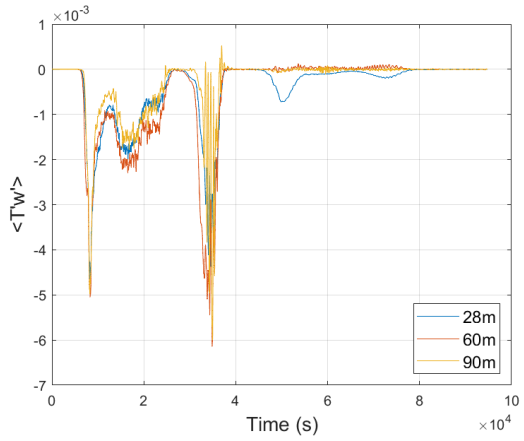

(m) Latneg70, $< T'w' >$

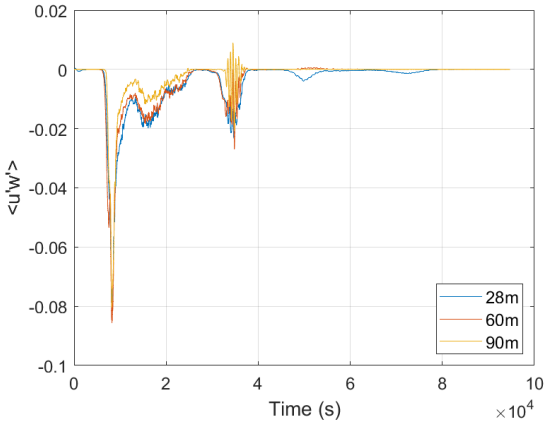

(n) Latneg70, $< u'w' >$

Figure A.3: Horizontally averaged buoyancy (left) and momentum (right) fluxes for each latitude case.

A.3 Wake Models

The details of the wake models, separated into 'Deflection' and 'Velocity Deficit' models are presented below.

A.3.1 Deflection Models

A.3.1.1 Jiménez Model

The Jiménez model was derived from the assumption of a top hat velocity deficit profile, as used by Katic and Jensen. Appling the conservation of momentum to get the wake skew angle, θ, is then given by,

$$\theta = \frac{C_T \cos^2\gamma \sin\gamma}{2\left(1 + 2k_d{}^{x}/_{D}\right)} \tag{A.1}$$

where γ is the yaw angle of the turbine and k_d is the wake deflection factor. The yaw angle is positive in the counter-clockwise direction, while the skew angle is positive in the clockwise direction from the rotor axis. Integrating the skew angle with respect to the distance downstream from the turbine, x, gives the wake deflection. It is assumed that there is no wake deflection at the turbine, so $y_{def(x=0)} = 0$. The relationship for wake deflection is thus given by,

$$\frac{y_{def}}{D} = \cos^2\gamma \sin\gamma \frac{C_T}{4k_d}\left(1 - \frac{1}{1 + 2k_d{}^{x}/_{D}}\right). \tag{A.2}$$

An additional assumption made above is that the wake expands linearly with downstream distance, which is only considered to be true in the far wake [13]. Therefore, the Jiménez

model should not be considered accurate in its representation of the near wake, which demonstrates more complex behaviour than that of the far wake [13][41]. A thrust coefficient of $C_T = 0.7$ and a wake deflection factor of $k_d = 0.17$ were used, per Annoni *et al.* [23].

A.3.1.2 FLORIS Model

The basis of the FLORIS model is the representation of different wake zones depending on the radial distance from the wake centre tp depict the variation in recovery across the wake cross-section [11]. The model incorporates aspects of the Jiménez model and Jensen model and includes an inherent wake deflection due to the rotation of the turbine blades. FLORIS uses the same relationship for the skew angle as shown in Equation A.1, with the initial skew angle given at $x = 0$, as

$$\theta_0 = \frac{1}{2} C_T \cos^2 \gamma \sin \gamma. \tag{A.3}$$

Similar to the Jiménez model, the yaw angle is positive in the counter-clockwise direction from the rotor. The tangent of this skew angle is then integrated, using a second order Taylor series approximation, over the downstream distance from the turbine rotor, x, to give the lateral deflection due to yaw as,

$$y_{def,yaw} = \frac{\theta_0 \left[15 \left[\frac{2k_d x}{D} + 1 \right]^4 + {\theta_0}^2 \right]}{\frac{30k_d}{D} \left[\frac{2k_d x}{D} + 1 \right]^5} - \frac{\theta_0 D \left(15 + {\theta_0}^2 \right)}{30k_d}. \tag{A.4}$$

As suggested by Fleming *et al.*, turbines in not in yaw display a small lateral wake deflection due to the rotation of the wake and stratification of the ABL [19]. Gebraad *et al.* used data from SOWFA simulations to parameterise the following function for rotation induced deflection [11],

$$y_{def,rotation} = a_d + b_d x \tag{A.5}$$

where the constants a_d and b_d are obtained from the results of SOWFA simulations by Gebraad *et al.*[11]. The wake deflection is therefore given by the sum of the deflection due to yaw and deflection due to wake rotation,

$$y_{def} = y_{def,yaw} + y_{def,rotation}. \tag{A.6}$$

The constant values implemented in this model are $a_d = -4.5$, $b_d = -0.01$ and $k_d = 0.15$ per Gebraad *et al.*[11].

A.3.1.3 Gaussian Model

The Gaussian model, as developed by Bastankhah and Porté-Agel, is derived from wind tunnel measurements of a yawed turbine and the observation of self-similarity within the wind turbine wake. Self-similarity in the wake occurs when the velocity deficit normalised with the maximum velocity deficit collapses onto a single curve, regardless of the downstream distance [39]. Compared with previous models assuming top-hat distribution assumptions, the Gaussian distribution more accurately reflects the wake velocity profile as measured experimentally [124][39].

The Gaussian model separates the wake into 'near' and 'far' wake regions, with the latter being where the model is most applicable. The model for the near wake region is primarily used to provide a basis for the calculation of far wake features.Henceforth, variables with the subscript '0' refer to values calculated in the near wake. The skew angle in the near wake is given by,

$$\theta_0 = \frac{0.3\gamma}{\cos\gamma}\left(1 - \sqrt{1 - C_T\cos\gamma}\,\right). \tag{A.7}$$

It should be noted here, that the yaw angle is considered as positive in the clockwise direction from the rotor, which differs from the previous two models.

The above skew angle is assumed as constant within the near wake up to a distance of x_0 downstream from the rotor. This is referred to as the 'potential core' length and is given by,

$$\frac{x_0}{D} = \frac{\cos\gamma\left(1 + \sqrt{1 - C_T}\right)}{\sqrt{2}\left[4\alpha I + 2\beta\left(1 - \sqrt{1 - C_T}\right)\right]} \tag{A.8}$$

where α and β are parameters tuned from experimental measurements and I is the turbulence intensity of the flow.

This turbulence intensity variable aims to incorporate both the ambient turbulence and any additional turbulence present in upstream turbine wakes. As just one turbine is modelled in this study, only the ambient turbulence intensity was considered for this variable. For more information on a method to model the turbulence intensity due to multiple upstream wakes, refer to [112].

Given the skew angle remains constant in the near wake, the deflection in this region is proportional to the length of the potential core,

$$\frac{y_{def_0}}{D} = \frac{x_0}{D}\tan\theta_0 \approx \frac{x_0}{D}\theta_0. \tag{A.9}$$

To maintain mass conservation, the potential core width at the turbine must be greater

than the diameter of the rotor. Bastankhah and Porté-Agel describe the rotor area as elliptical with the width as a lateral minor axis of $D\cos\gamma\sqrt{U_R/U_0}$, where U_R is the velocity at the rotor. This compares to the minor axis of the ellipse frontal area of a yawed turbine of $D\cos\gamma$ [39].

The wind tunnel measurements demonstrate the streamwise velocity deficit within the potential core region to be approximately constant. The width of the wake at x_0 in the lateral and vertical directions is thus found by equating the streamwise momentum deficit at the rotor with that at x_0 to give,

$$\frac{\sigma_{z_0}}{D} = \sqrt{\frac{1+\sqrt{1-C_T\cos\gamma}}{8(1+\sqrt{1-C_T})}} \tag{A.10}$$

$$\frac{\sigma_{y_0}}{D} = \frac{\sigma_{z_0}}{D}\cos\gamma. \tag{A.11}$$

Similar to the Jiménez and FLORIS models, the wake in the far region is assumed to expand linearly with distance from the rotor and so the variation in wake width can be approximated as,

$$\frac{\sigma_y}{D} = k_y\frac{(x-x_0)}{D} + \sigma_{y_0} \tag{A.12}$$

$$\frac{\sigma_z}{D} = k_z\frac{(x-x_0)}{D} + \sigma_{z_0}. \tag{A.13}$$

where k_y and k_z are the wake growth rates in the lateral and vertical directions, respectively, and are assumed to be equal in this study. These are calculated based on the inflow turbulence intensity,

$$k_y = k_z = 0.38371I + 0.003678 \tag{A.14}$$

where I is the ambient turbulence intensity.

The wake skew angle beyond x_0 was derived from the conservation of the spanwise momentum and the application of a Gaussian distribution to the skew angle. Integrating this gives the wake deflection in the far wake as,

$$\begin{aligned}\frac{y_{def}}{D} = \frac{y_{def_0}}{D} + \frac{\theta_0}{14.7}\sqrt{\frac{\cos\gamma}{k_y k_z C_T}}\left(2.9 + 1.3\sqrt{1-C_T} - C_T\right) \\ \times \ln\left[\frac{\left(1.6+\sqrt{C_T}\right)\left(1.6\sqrt{\frac{8\sigma_y\sigma_z}{D^2\cos\gamma}} - \sqrt{C_T}\right)}{\left(1.6-\sqrt{C_T}\right)\left(1.6\sqrt{\frac{8\sigma_y\sigma_z}{D^2\cos\gamma}} + \sqrt{C_T}\right)}\right].\end{aligned} \tag{A.15}$$

The constant values used with this model are $I = 8\%$, $C_T = 0.7$, $\alpha = 0.58$ and $\beta = 0.077$.

For a more detailed derivation of this model refer to [39].

A.3.2 Velocity Deficit Models

A.3.2.1 Abkar Model

The velocity deficit in the Abkar Model is assumed to take a skewed Gaussian shape to account for the effect of inflow wind veer on the wake. This is achieved by incorporating the angle of the horizontal wind vector, α_{in}, and how it varies with height. The lateral displacement of the wake, Δy_{wake} at each downstream distance is thus given by,

$$\Delta y_{wake} = x \tan(\alpha_{in}), \tag{A.16}$$

where x is the distance downstream from the turbine. This is then incorporated in the velocity deficit model proposed by Bastankhah and Porté-Agel [125] and expanded on in Abkar *et al.* [27],

$$\frac{\Delta U}{U_{hub}} = \frac{\Delta U_{max}}{U_{hub}} \exp\left(-\frac{1}{2}\left[\left(\frac{y + x\tan\alpha_{in}}{\sigma_y}\right)^2 + \left(\frac{z - z_{hub}}{\sigma_z}\right)^2\right]\right), \tag{A.17}$$

where σ_y and σ_z are the lateral and vertical standard deviation in the velocity profiles in terms of the Gaussian shape, respectively, when wind veer is not present. The maximum velocity deficit is computed as,

$$\frac{\Delta U_{max}}{U_{hub}} = \left(1 - \sqrt{1 - \frac{C_T}{8\left(\frac{\sigma_y \sigma_z}{D^2}\right)}}\right), \tag{A.18}$$

where C_T is the thrust coefficient. The above solution may diverge in the near wake region where the wake is not necessarily self-similar Gaussian. According to the one-dimensional momentum theory [80][10], the normalised maximum velocity deficit should not exceed $2a$, where a is the axial induction factor. The axial induction factor is related to the thrust coefficient via,

$$a = \frac{1 - \sqrt{1 - C_T}}{2}. \tag{A.19}$$

The normalised velocity deficit in the region near the wake is thus taken as the maximum value out of $2a$ or the output of Equation A.18. As done with previous studies into analytical wake models [125][39], the standard deviations in the Gaussian profile are assumed to expand linearly with downstream distance as,

$$\sigma_y = k_y x + \epsilon D, \;\; \sigma_z = k_z x + \epsilon D. \tag{A.20}$$

Here the terms k_y and k_z represent the wake growth rate in the lateral and vertical directions, respectively, and ϵ is a non-dimensional parameter that relates to the standard deviation of the wake as x approaches zero. This is modelled as,

$$\epsilon = 0.2\sqrt{\beta}, \text{ where } \beta = \frac{1}{2}\frac{1+\sqrt{1-C_T}}{\sqrt{1-C_T}}. \tag{A.21}$$

The wake growth in the lateral and vertical directions is assumed to be the same, so $k_y = k_z = k$, with $k = 0.024$ adopted in this study as it best fit the data obtained in [80]. A thrust coefficient of $C_T = 0.7$ was also used.

A.3.2.2 GCH Model

The Gaussian Curl Hybrid (GCH) Model combines the velocity deficit model from Bastankhah and Porté-Agel [39] with the curled wake model proposed by Martinez-Tossas *et al.* [65]. The velocity deficit in the streamwise component is given by,

$$\frac{u_G}{U_\infty} = 1 - C\exp\left(\frac{-(y-y_0-\delta)^2}{2\sigma_y^2} - \frac{(z-z_h)^2}{2\sigma_z^2}\right), \tag{A.22}$$

where,

$$C = 1 - \sqrt{1 - \frac{\sigma_{y0}\sigma_{z0}C_T}{\sigma_y\sigma_z}}. \tag{A.23}$$

Here U_∞ is the freestream velocity, C_T is the thrust coefficient, δ is the wake deflection as calculated in Equation A.15, y_0 is the spanwise turbulent position, z_h is the hub height, σ_y is the wake width in the lateral direction and σ_z is the wake width in the vertical direction. The subscript "0" refers to value obtained at the start of the far wake, the location of which is determined as done in Equation A.8. For more details on the near wake calculations see Section A.3.1.3 and [39].

The wake widths are defined as,

$$\frac{\sigma_z}{D} = k_z\frac{(x-x_0)}{D} + \frac{\sigma_{z0}}{D} \text{ where } \frac{\sigma_{z0}}{D} = \frac{1}{2}\sqrt{\frac{u_R}{U_\infty + u_0}}, \tag{A.24}$$

$$\frac{\sigma_y}{D} = k_y\frac{(x-x_0)}{D} + \frac{\sigma_{y0}}{D} \text{ where } \frac{\sigma_{y0}}{D} = \frac{\sigma_{z0}}{D}\cos\gamma. \tag{A.25}$$

Here D is the rotor diameter, γ is the yaw angle, u_R is the velocity at the rotor, u_0 is the velocity at the end of near near wake, k_y and k_z are the wake growth rates in the lateral and vertical directions, respectively. The wake growth rates in this model implementation are assumed to be equal in the lateral and vertical directions. The velocity at the rotor is

given by,

$$\frac{u_R}{U_\infty} = \frac{C_T \cos\gamma}{1 - \sqrt{1 - C_T \cos\gamma}}, \tag{A.26}$$

while the velocity at the end of the near wake is,

$$\frac{u_0}{U_\infty} = \sqrt{1 - C_T}. \tag{A.27}$$

The original Gaussian velocity deficit model did not include calculation of the spanwise and vertical velocity components [39]. Martinez-Tossas *et al.* [65] proposed including a Lamb-Oseen vortex to model the wake rotation, the circulation strength of which is given by,

$$\Gamma_{wr} = \frac{\pi(a - a^2)U_\infty D}{\lambda} \tag{A.28}$$

where λ is the tip-speed ratio calculated as $\lambda = \dfrac{\omega D}{2U_\infty}$ with ω as the rotation speed of the turbine blades. The axial induction factor is linked to the yaw angle and thrust coefficient as below,

$$a = \frac{1}{2\cos\gamma}\left(1 - \sqrt{1 - C_T \cos\gamma}\right). \tag{A.29}$$

The vertical and spanwise velocities can then be calculated using the strength of the vortex due to rotation,

$$V_{wr} = \frac{\Gamma_{wr}(z - z_h)}{2\pi\left((y - y_0)^2 + (z - z_h)^2\right)}\left(1 - \exp\frac{-(y - y_0)^2 - (z - z_h)^2}{\epsilon^2}\right) \tag{A.30}$$

$$W_{wr} = \frac{-\Gamma_{wr}(y - y_0)}{2\pi\left((y - y_0)^2 + (z - z_h)^2\right)}\left(1 - \exp\frac{-(y - y_0)^2 - (z - z_h)^2}{\epsilon^2}\right). \tag{A.31}$$

From Martinez-Tossas *et al.* [65], ϵ represents the size of the vortex core and is taken as $\epsilon = 0.3D$. Vortices in the wake also form due to yaw misalignment, including a counter-rotating vortex pair at the top and bottom of the rotor. The strength of the vortices due to yawing is given by,

$$\Gamma(\gamma) = \frac{\pi}{8}\rho D U_\infty C_T \sin\gamma(\cos\gamma)^2, \tag{A.32}$$

where ρ is the density of the air. The spanwise velocity components of the vortex pair is then calculated using this vortex strength,

$$V_{top} = \frac{\Gamma_{top}(z - z_h + {}^D\!/_2)}{2\pi\left((y - y_0)^2 + (z - z_h - {}^D\!/_2)^2\right)}\left(1 - \exp\frac{-(y - y_0)^2 - (z - z_h - {}^D\!/_2)^2}{\epsilon^2}\right) \tag{A.33}$$

$$V_{bot} = \frac{\Gamma_{bot}(z - z_h - {}^D\!/_2)}{2\pi\left((y - y_0)^2 + (z - z_h + {}^D\!/_2)^2\right)}\left(1 - \exp\frac{-(y - y_0)^2 - (z - z_h + {}^D\!/_2)^2}{\epsilon^2}\right). \tag{A.34}$$

Γ_{top} and Γ_{bot} are computed using the velocities at the top and bottom of the rotor, respectively. Due to the sheared velocity profile, Γ_{top} is larger than Γ_{bot}. The total spanwise velocity in the wake is then found by linear combination of the spanwise components as below,

$$V_{wake} = V_{top} + V_{bot} + V_{wr}. \tag{A.35}$$

A similar approach is taken for the vertical velocity in the wake, as outlined below,

$$W_{top} = \frac{-\Gamma_{top}(y - y_0)}{2\pi\left((y - y_0)^2 + (z - z_h - {}^{D}/_{2})^2\right)}\left(1 - \exp\frac{-(y - y_0)^2 - (z - z_h - {}^{D}/_{2})^2}{\epsilon^2}\right) \tag{A.36}$$

$$W_{bot} = \frac{-\Gamma_{bot}(y - y_0)}{2\pi\left((y - y_0)^2 + (z - z_h + {}^{D}/_{2})^2\right)}\left(1 - \exp\frac{-(y - y_0)^2 - (z - z_h + {}^{D}/_{2})^2}{\epsilon^2}\right) \tag{A.37}$$

$$W_{wake} = W_{top} + W_{bot} + W_{wr}. \tag{A.38}$$

Finally, the vortices in the wake decay as it moves downstream, with this dissipation described by Bay *et al.* [126] and is computed as,

$$V = V_{wake}\left(\frac{\epsilon^2}{4\nu_T\frac{(x - x_0)}{U_\infty} + \epsilon^2}\right) \tag{A.39}$$

$$W = W_{wake}\left(\frac{\epsilon^2}{4\nu_T\frac{(x - x_0)}{U_\infty} + \epsilon^2}\right). \tag{A.40}$$

Here ν_T is the turbulent viscosity, defined using a mixing length model,

$$\nu_T = l_m^2\left|\frac{\partial U}{\partial z}\right|, \tag{A.41}$$

where $l_m = \frac{\kappa z}{1 + {}^{\kappa z}/_{\lambda_T}}$ with $\kappa = 0.41$ and the mixing length used is $\lambda = {}^{D}/_{8}$ for the free atmosphere [127]. Wakes are known to recover faster in yawed flow conditions and so some added wake recovery is included in the streamwise velocity calculation based on momentum conservation and enhanced entrainment into the wake via the vertical velocity component, W. This gives the streamwise velocity as,

$$U = u_G + \frac{W(x - x_0)(y - y_0)}{\pi(\alpha_r(x - x_0) + \frac{D}{2})^2}, \tag{A.42}$$

where u_G is the velocity computed in Equation A.22 and α_r is a tuning parameter for how much entrainment influences wake recovery. Using the same value as King *et al.* [40],

$\alpha_r = 0.03$, where larger values mean a smaller effect of entrainment on the recovery of the streamwise velocity.

B. Results and Analysis

B.1 Variation in Wind Veer Profiles

The ±40° and ±70° latitude wind veer profiles, as shown in Figure 4.1, demonstrate a change in direction across the upper region of the rotor, which is contrasted with the near linear profile demonstrated by the ±10° latitudes. In the upper region of the domain, the wind velocity oscillates about a constant value and the frequency of this oscillation is proportional to the Coriolis forcing and thus latitude. This is depicted in Figure B.1, which depicts the difference in how the streamwise velocity changes at half the height of the domain between the different positive latitudes. This is known as inertial oscillation and occurs as the Coriolis forcing turns the wind away from its steady-state value [128]. The

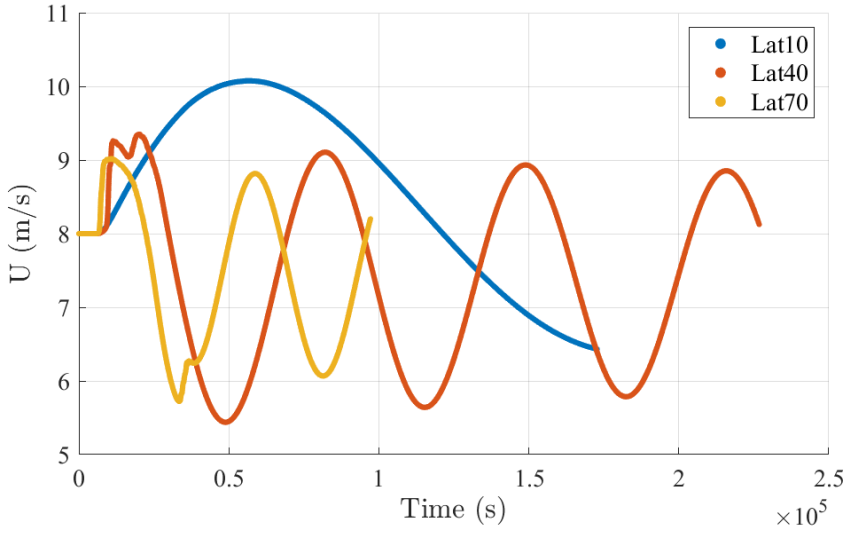

Figure B.1: Horizontally averaged streamwise velocity at 400 m with time.

result of this is that the wind veer profile above 100 m, varies with time as the streamwise and spanwise velocity components fluctuate, as shown in Figure B.2. The 'turning' of the wind veer profile is also observed to be more substantial for the higher latitude and thus higher Coriolis forcing conditions with Figure B.3 depicting the different veer profiles recorded at various run times.

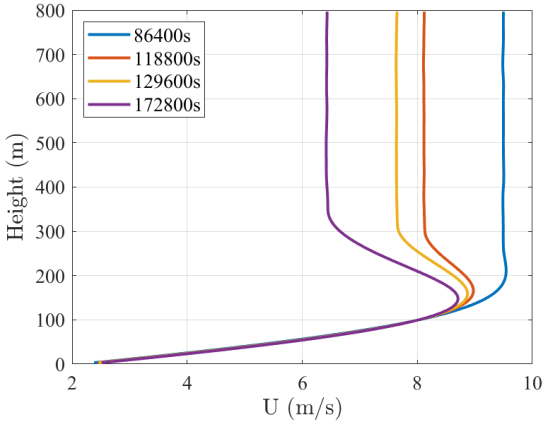

(a) Lat10 Streamwise velocity, U

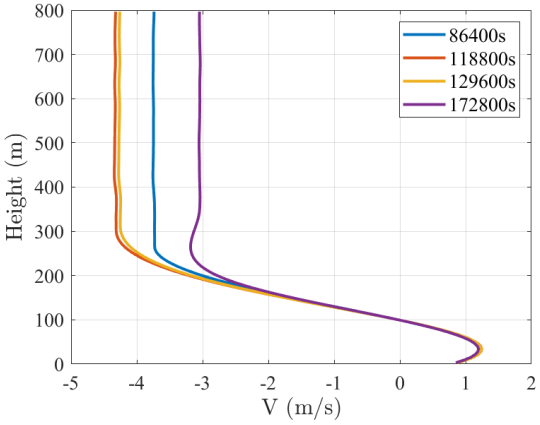

(b) Lat10 Spanwise velocity, V

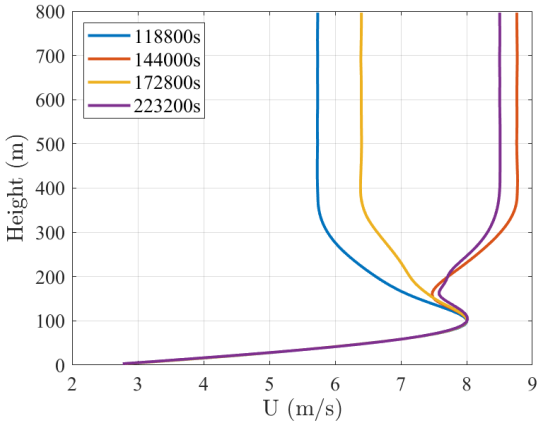

(c) Lat40 Streamwise velocity, U

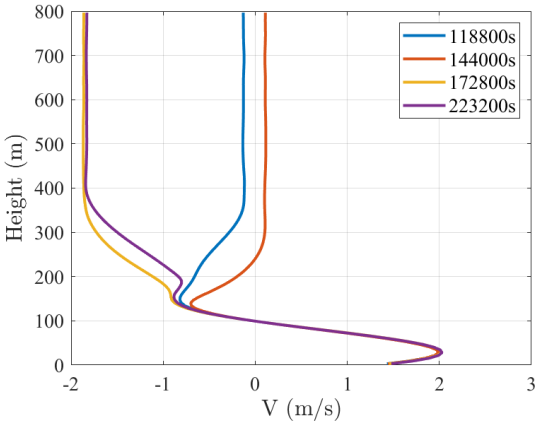

(d) Lat40 Spanwise velocity, V

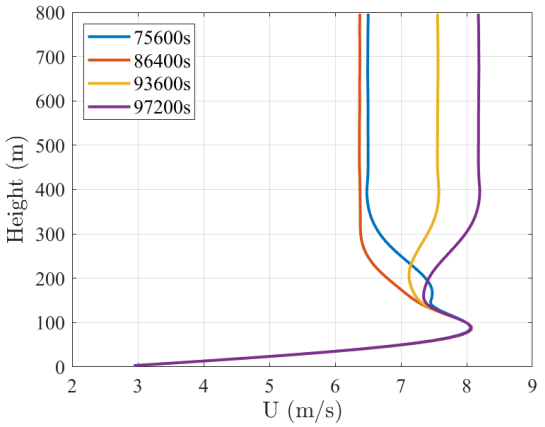

(e) Lat70 Streamwise velocity, U

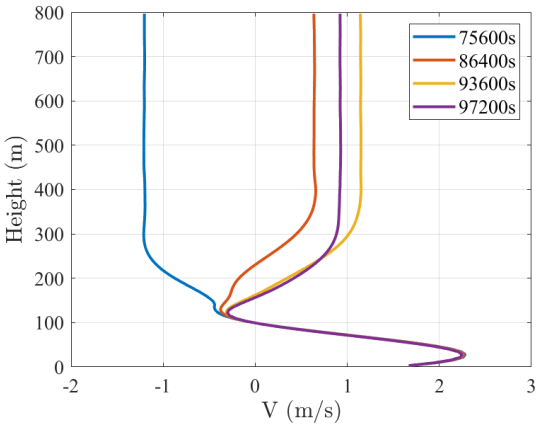

(f) Lat70 Spanwise velocity, V

Figure B.2: Streamwise (left) and spanwise (right) velocity components for the positive latitudes at various run times.

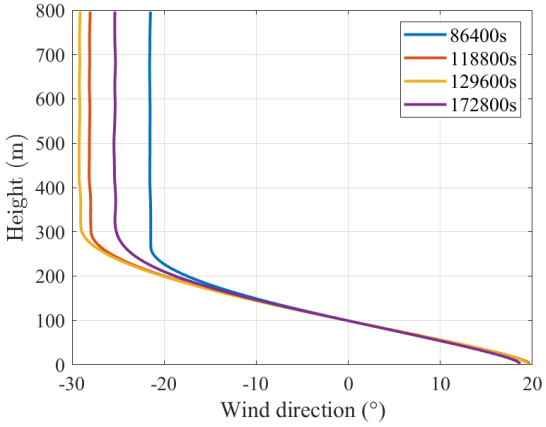

(a) Lat10

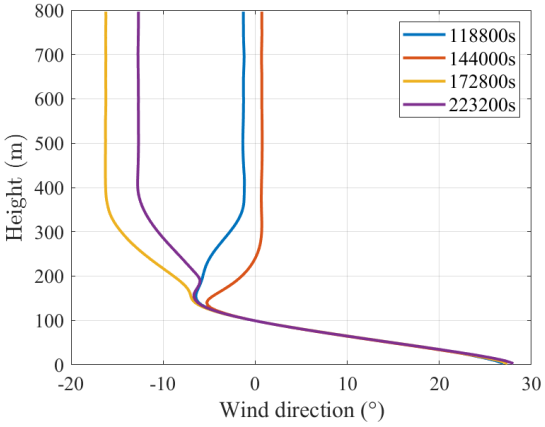

(b) Lat40

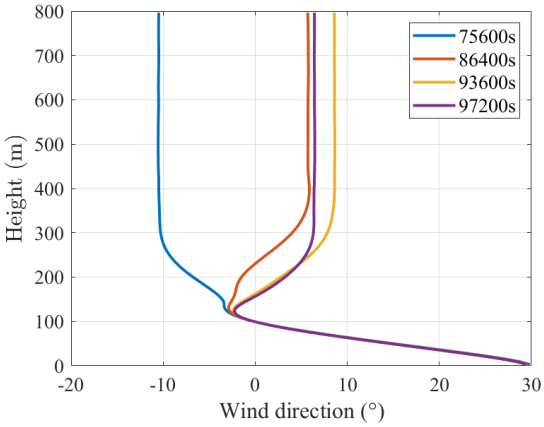

(c) Lat70

Figure B.3: Horizontal wind vector angle profiles for the positive latitudes at various run times.